Science and History Explored by Nuclear Magnetic Resonance

vorgelegt von

M. Sc. Maria Antoaneta Baias

aus Dej, Romania

„Laziness may appear attractive, but work gives satisfaction."

Anne Frank

Berichte aus der Physik

Maria Antoaneta Baias

Science and History Explored by Nuclear Magnetic Resonance

Contents

1 Introduction

Mummies, bones, chemical reactions, keratin, proton exchange membranes… it sounds like some random words put together with no meaning. Yet, there is something that unites all of them, and that is NMR (Nuclear Magnetic Resonance). NMR is the method chosen to describe all the above-mentioned materials ranging from biological materials to synthetic polymers. Why? Because NMR comprises of a large variety of methods, which, when judiciously applied to such samples are able to provide detailed insight into the molecular structures and arrangements [Cal91, Blü00].

Conventional high-field solid-state NMR offers many techniques for characterizing heterogeneous materials at microscopic and macroscopic levels. Solid-state NMR can provide relevant information about polymer materials, ranging from features of molecular structure to describing the various kinds of interactions in such systems and can also provide useful information about the molecular dynamics of these systems. Studying and understanding of proteins is another field where solid-state NMR proved to be a very useful tool. Its main focus is the characterization of solid proteins, especially the ones linked to human diseases such as Alzheimer's, CJD and Type II diabetes with solid protein deposits in vital organs of the body [Due01]. It can be used as a method for investigating the domain sizes and morphology of synthetic polymers and biopolymers [Buda03a, Buda03b, Buda04] such as keratin, or the proton dynamics inside the polymer chains of the proton exchange membranes for fuel cells [Bai08].

In the recent years hyperpolarized noble gases are being used in NMR and MRI from very large magnetic fields to the Earth magnetic field. Their main advantage is the large nuclear spin polarization, created through spin exchange optical pumping which can be transferred to other nuclei thus enhancing the signal to noise ratio [App04]. For this reason it was applied for the online-monitoring of chemical reactions where single-shot spectra acquired at different times during the polymerization offer good insight of the reaction.

Modern mobile NMR uses low filed magnets with single-sided sensors like the MOUSE (MObile Universal Surface Explorer) [Per05, Blü08]. Mobile NMR holds great promise in a variety of fields [Fer01], in particular in medicine, materials science [Hak00, Blü00], chemical engineering [Gla03], and space science [Pow59]. It has the advantage of using an open magnet geometry, where the sensor much smaller than the object is placed

near the object to acquire signals from the object volume near the sensor, which thus provides a non-invasive method of material characterization [Blü08]. It allows non-destructive investigations of samples, which is desired when objects are large and need to be investigated as in the case for the preservation of cultural and historical heritage such as ancient mummies and bones [Rüh07].

The aim of this work is to prove my statement that it is NMR that unites the large variety of materials that I am investigating and describing in this thesis. Therefore, I will show that NMR is able to provide the morphology and molecular structures and conformations to understand the functional properties of materials such as proton exchange membranes for fuel cells or fibrous proteins like the α-keratin of wool and hair. NMR in combination with hyperpolarization by spin-exchange optical pumping offers good insight into the fundamental processes that occur during chemical reactions such as polymerization reactions. It is also NMR that provides the unique method of characterizing precious objects of cultural heritage from historical mummies and bones to the great masterpiece of famous artists in a non-destructive manner with the help of the NMR-MOUSE.

2 Thermal Denaturation of Keratin Fibers by Solid-State NMR

2.1 Introduction

Proteins exhibit their active properties within certain ranges of temperature and unfold beyond the limits. These ranges are near room temperature, although for many industrial applications of enzymes it would be of interest to have them active at higher temperatures. A few proteins withstand temperatures above 100° C and among them there are some of the fibrous proteins.

Fibrous proteins are distinguished from globular proteins by their filamentous, elongated form. Most of them play structural roles in animal cells and tissues. Among the most prominent representatives of this class are the α-keratins in human hair, wool and finger nails, fibroin in silk, actin and myosin in muscles, and collagen, the most abundant protein in vertebrate bodies.

The keratin fibre structure is modelled by a crystalline rod-like α-helix (intermediate filaments, IFs) embedded in an amorphous matrix (Fig. 2.1) (intermediate filament associated proteins, IFAP) having a relatively high amount of cystine [Feu02, and references therein]. The structure of hard a-keratin is characterized by three structural hierarchy levels [Raf04]. At high resolution, the intermediate filament (IF) protein is made of a central rod domain of sequences (1A, 1B, 2A, 2B) containing an aminoacid heptade repeat unit that favours the formation of α-helical structure and separated by loop links (L1, L12, and L2) [Par85, Ste89]. At the extremity of the rod domain the globular C- and N-terminal domains are located and arranged mostly in β-sheet and formed of rich of sulphur compounds [Pow97, Par05]. Two α-helices form a parallel, superhelical dimer. At medium resolution, i.e. the intermediate level arrangement of the heterodimers inside Ifs, the molecules are assembled both longitudinally and laterally in an ensemble called microfibril [Bir57]. The dimers are associated as straight tetramers with random orientations [Raf04] and this organization forms a long cylinder-shaped intermediate filament with uniform density. At lower structural resolution, the bundles of parallel Ifs are organized in amorphous and disordered crystalline lateral network. These are embedded in

a sulphur-rich protein matrix of intermediate filaments associated proteins (IFAP) and form a macrofibril, the main morphological components of hard α-keratin fibres [Raf04].
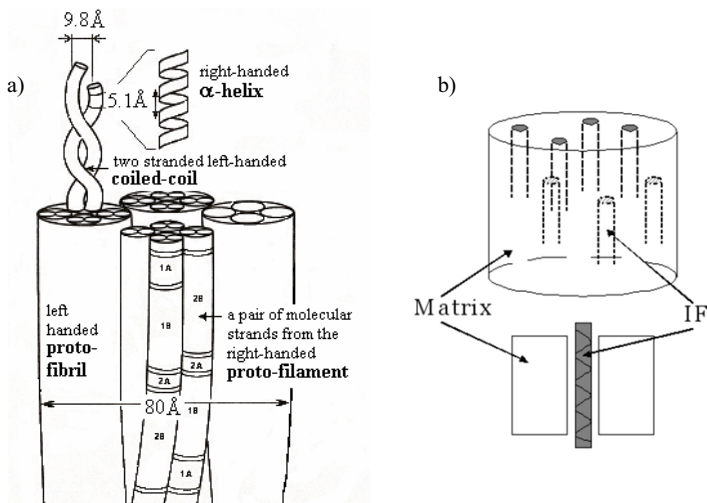
Fig. 2.1 (a) The intermediate filament structure [Bai09]. (b) Schematic representation of the two-phase model of keratin fibres. The intermediate filaments (IF) are imbedded in an amorphous keratin matrix.

Although the above model was proposed to explain the mechanical behaviour of keratins, it appeared to also comply with the high denaturation temperature found at keratins [Wor07, Wor08]. In soluble proteins the helix denaturates (unfolds) at temperatures up to 80° C. There are no data on the denaturation temperature of free IFs which are not surrounded by a matrix but one may expect that the α-helix of keratins would also unfold at temperatures of about 80° C. The fact that keratin proteins denaturate at about 200° C is assumed to be due to the rigidity of the matrix, whose viscosity impedes the unfolding of the helix. The viscosity and crosslinked structure of the matrix governs, therefore, the segmental mobility of the α-helix and the unfolding reaction (denaturation).

A similar model was proposed for collagen based materials [Mil99]. The model suggests that the addition of solvents able to decrease the viscosity of the matrix depresses the temperature of unfolding. This has indeed been noticed in DSC experiments with keratin fibres [Hal67, Ler05] and with collagen based materials (parchments, leathers) in watery environments [Bud03, Bud04, Pop08]. Detailed insights into how keratins protect the intermediate filaments against thermal denaturation up to high temperatures is of fundamental interest for understanding protein denaturation. The role of matrix in this

process may suggest ways for designing high-temperature stable proteins as new biomaterials.

Multinuclear and multidimensional liquid- and solid-state NMR are important techniques in structural biology [Wüt86, Ern90, Due01]. They are well suited to the investigation of non-crystalline molecules, such as proteins, that often cannot be studied with other experimental techniques. Recently, a ^{13}C and ^2H solid-state NMR investigation of an α-keratin from equine hoof has revealed a strong dependence of molecular conformation and molecular dynamics on the degree of hydration of the material [Due03]. In particular, dehydration results in a much more rigid and ordered structure, with a loss of α-helical components in the structure and breaking of cysteine disulfide linkages. Moreover, the molecular dynamics and structural organization of mouse epidermal keratin intermediate filaments (IF) have been studied by ^{13}C and ^2H spectroscopy and relaxometry on IF labelled with isotopically enriched amino acids [Mac88]. Solid-state ^{31}P NMR spectroscopy was also applied to the analysis of phosphorylated wool keratin to investigate the modification located on the surface of wool keratin [Yos90].

The clarification of the fine structure of fibrous proteins that include keratin in the solid state is very important for understanding their nature. The key to access the structure is the fact that the ^{13}C and ^{15}N chemical shifts of polypeptides substantially depend on their main-chain conformations such as α-helix and β-sheet forms. NMR measurements could therefore confirm that both right-handed α-helix and β-sheet forms exist in native wool fiber [Nis98, Nis99].

Spin-diffusion NMR has been shown to be a useful method for characterizating semicrystalline polymer morphology [Sch94, Dem95, Van96, Buda03a, Buda04]. The sizes of the rigid, interfacial, and amorphous fractions can be estimated from such experiments and the results compared well to those from TEM and X-ray diffraction.

The aim of this part is to investigate the effect of thermal denaturation of hydrated wool and hair keratin by ^1H NMR wide-line spectroscopy and ^1H spin diffusion and to monitor the damage induced by various chemical treatments on the hair keratin. Moreover, cross-polarization magic angle spinning (CPMAS) ^{13}C NMR was used for this purpose. The phase (fraction) composition was determined from ^1H wide-line spectra *ex situ* for different denaturation temperatures. Three fractions were detected, a rigid, an interfacial, and an amorphous one. The domain sizes were determined for different stages of denaturation by ^1H spin-diffusion NMR for two different wool keratin morphologies. The rigid domain sizes for the hair samples were measured by ^1H spin-diffusion using initial-

rate approximation. The molecular dynamics of the interfacial region can also be investigated by ^{1}H spin-diffusion NMR. The changes in the degree of α-keratin organization, the amounts of different phases and molecular dynamics are discussed with regard to the temperatures of the thermal denaturation process.

2.2 Theory

2.2.1 Spin-diffusion observables

The transport of z-magnetization oriented along the static magnetic field in a NMR experiment can be described by the diffusion equation in the continuum approximation. The concentration $m(\vec{r},t)$ of nuclear z-magnetization at position $\vec{r}$ in the sample from the centre of symmetry of different morphologies (Fig. 2.2a and b) at the moment of time t is defined by

$$m(\vec{r},t) = \frac{M_z(\vec{r},t)}{\rho(\vec{r})\Delta V(\vec{r})}, \tag{2.1}$$

where $M_z(\vec{r},t)$ is the total z-magnetization and $\Delta V(\vec{r})$ is the infinitesimal volume around the point defined by the vector $\vec{r}$. The number density of spins is denoted by $\rho(\vec{r})$.
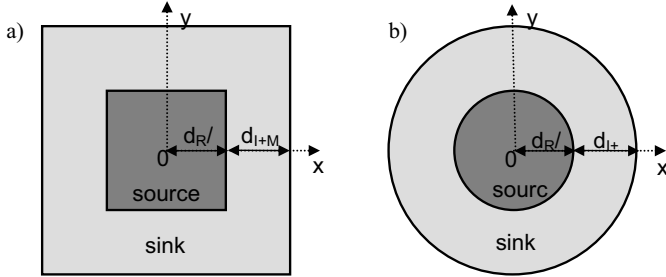
Fig. 2.2 Schematic representation of the square **(a)** and cylindrical **(b)** morphologies used to approximate the keratin tertiary structure. The combined size of interface and mobile (amorphous) fractions is doted by d_{I+M} and d_R is the size of the rigid domain.

In the limit of isotropic spin-diffusion and spatially constant spin diffusivity the spin diffusion equation has the form

$$\frac{\partial m(\vec{r},t)}{\partial t} = D\nabla^2 m(\vec{r},t). \tag{2.2}$$

The instantaneous NMR observables in a spin-diffusion experiment are represented by the normalized integral intensity $I_i(t)/I_0$ of the ith component of the NMR spectrum

with the total integral intensity I_0. More specific the NMR spin-diffusion observables are defined by

$$\frac{I_i(t)}{I_0} = \frac{\oiiint\limits_{V_i} \rho_i m_i(\vec{r},t) d\vec{r}}{I_0},$$

(2.3)

where V_i is the volume of the ith domain.

2.2.2 Spin-diffusion for a square morphology

The real morphology of keratin in wool can be approximated by a square transverse morphology (Fig. 2.2a). We assume that the spin-diffusion takes place in a heterogeneous matrix from a source R with low segmental mobility into a finite sink M with larger segmental mobility. The interfacial region is taken together with the amorphous fraction in the following considerations. The relationships describing the time evolution of the integral intensities of the NMR signals $I_R(t)$ and $I_M(t)$ for a spin-diffusion process of dimensionality $n=2$ can be obtained from Refs. [Wan96] and [Buda03b]. The magnetization in the source region (R) for a two-dimensional spin-diffusion process is given by

$$I_R(t) \approx \rho_R \left[2 \int\limits_0^{d_R/2} m_R(x,t) dx \right]^2,$$

(2.4)

where ρ_R is the number density of spins of the source R of size d_R and $m_R(x,t)$ is the space and time dependent concentration of the z magnetization. For a dipolar filter that selects only the magnetization of the R region, the magnetization in the sink region can be written as

$$I_M(t) = I_R(0) - I_R(t).$$

(2.5)

The quantity $m_R(x,t)$ is given by [Wan96, Buda03b]

$$\begin{aligned}
m_R(x,t) = {} & \frac{\rho_R d_R m_{0R}}{\rho_R d_R + \rho_M d_M} - \sum_{m=1}^{\infty} 2m_{0R} \sin[kd_M \beta_m] \cos[x\beta_m] \exp[-D_R \beta_m^2 t] \beta_m^{-1} \\
& \cdot \Big\{ [\sigma d_R + kd_M] \cos[d_R \beta_m] \cos[kd_M \beta_m] - \\
& \quad - [\sigma kd_M + d_R] \sin[d_R \beta_m] \sin[kd_M \beta_m] \Big\}^{-1}
\end{aligned}$$

(2.6)

where d_M is the size of the sink ($d_M \approx d_{I+M}$), ρ_M is the number density of spins in the region M, $k = (D_R / D_M)^{1/2}$, and $\sigma = k\rho_R / \rho_M$. The spin-diffusion coefficients in the regions R and M are denoted by D_R and D_M, respectively. The quantities β_m, (m=1,2,3,…) are the roots of a trigonometric equation [Wan96, Buda03b]

$$\rho_R k \sin(d_R \beta)\cos(kd_M \beta) + \rho_M \cos(d_R \beta)\sin(kd_M \beta) = 0 . \qquad (2.7)$$

We note that the ratio d_M / d_R can be evaluated from the thermal equilibrium values of the R and M spectral components, i.e.,

$$E = \frac{I_{M,eq}}{I_{R,eq}} = \frac{\rho_M V_M}{\rho_R V_R} , \qquad (2.8)$$

where V_M and V_R are the volumes of the domains. For a square morphology (Fig. 2.2a) we can finally write

$$\frac{d_M}{d_R} = \left(E \frac{\rho_R}{\rho_M} \right)^{1/2} - 1 . \qquad (2.9)$$

The above Equation can be used for reducing the number of independent parameters that describe the decay and buildup curves in spin diffusion NMR.

2.2.3 Spin-diffusion for a cylindrical morphology

In the following we consider a more realistic cyllindrical morphology to describe spin-diffusion in wool keratin (cf. Fig. 2.2b). The rigid domains selected by a double-quantum dipolar filter are represented by the intermediate filaments (Fig. 2.1) that are surrounded by the amorphous keratin region. For simplicity we consider mobile (amorphous) and interface regions as the sink for the ^{1}H magnetization.

For a cylindrical morphology the equation that governs the diffusion of for the instantaneous concentration of z-magnetization $m(r,t)$ at distance r from the centre of cylinder is given by [Cra75]

$$\frac{\partial m(r,t)}{\partial t} = \frac{1}{r} \frac{\partial}{\partial r}\left[rD\frac{\partial m(r,t)}{\partial r} \right] . \qquad (2.10)$$

For a constant spin diffusivity D it can be written as

$$\frac{\partial m(r,t)}{\partial t} = \frac{D}{r} \frac{\partial m(r,t)}{\partial r} + D\frac{\partial^2 m(r,t)}{\partial r^2} . \qquad (2.11)$$

The equations of spin diffusion in a two-phase composite medium R and M (Fig. 2.2b) have the following forms:

$$\frac{\partial m_R(r,t)}{\partial t} = \frac{D_R}{r}\frac{\partial m_R(r,t)}{\partial r} + D_R\frac{\partial^2 m_R(r,t)}{\partial r^2}; \ (0 \leq r \leq d_R/2), \qquad (2.12)$$

and

$$\frac{\partial m_M(r,t)}{\partial t} = \frac{D_M}{r}\frac{\partial m_M(r,t)}{\partial r} + D_M\frac{\partial^2 m_M(r,t)}{\partial r^2}; \ (d_R/2 \leq r \leq (d_M+d_R)/2). \qquad (2.13)$$

The solutions of the above equations are obtained with the initial and boundary conditions. Considering an ideal magnetization filter we can write,

$$m_R(r,t)\big|_{t=0} = m_{0R}, \qquad (2.14)$$

$$m_M(r,t)\big|_{t=0} = 0, \qquad (2.15)$$

where the magnetization concentration is denoted by m_{0R} at the time when the action of dipolar filter was ended. Two boundary conditions need to be also specified. The first boundary condition is related to the continuity of the z-magnetization concentration at the domain boundary, i.e., for $r = d_R/2$, we have

$$m_R(r,t)\big|_{r=d_R/2} = m_M(r,t)\big|_{r=d_R/2}. \qquad (2.16)$$

The second boundary condition corresponds to the fact that magnetization fluxes, defined by the relation $\vec{j}(\vec{r},t) = -D\rho \cdot \nabla m(\vec{r},t)$, have to be equal at the domain interface. The following relation can be written

$$\rho_R D_R \frac{\partial}{\partial r} m_R(r,t)\big|_{r=d_R/2} = \rho_M D_M \frac{\partial}{\partial r} m_M(r,t)\big|_{r=d_R/2}. \qquad (2.17)$$

The NMR spin-diffusion observables for the cylindrical morphology are defined by the relationships

$$\frac{I_R(t)}{I_0} = \frac{\int_0^{d_R/2} r m_R(r,t)dr}{I_0}, \qquad (2.18)$$

and

$$\frac{I_M(t)}{I_0} = \frac{\int_{d_R/2}^{(d_M+d_R)/2} r m_M(r,t)dr}{I_0}. \qquad (2.19)$$

In the time regime in which the spin diffusion is not affected by the spin-lattice relaxation, the theorem of total magnetization conservation leads to

$$\frac{I_R(t)}{I_0} + \frac{I_M(t)}{I_0} = 1, \qquad (2.20)$$

which shows that in this case the two NMR observables are not independent.

For a spin system in thermodynamic equilibrium with a thermal bath we can define the ratio E between the total z-magnetization in the M and R domains given by Eqs. (2.18) and (2.19). The volume of the cylindrical domains can easily be evaluated, and from Eq. (2.20) we can finally write

$$\frac{d_M}{d_R} = \left(E \frac{\rho_R}{\rho_M} + 1 \right)^{1/2} - 1 .$$
(2.21)

Equation (2.21) establishes a relationship between the domain sizes independent of the spin-diffusion data.

Analytical solutions for the spin-diffusion equations can be established only for a composite medium with a uniform value of spin diffusivities [Dem95]. Realistic values for the domain sizes for a heterogeneous medium with spin-diffusivities $D_R \neq D_M$ can be obtained by the numerical solutions of Eqs. (2.12) and (2.13) with supplementary conditions Eqs. (2.14)-(2.17), and (2.21).

2.2.4 Spin-diffusion for a finite source and semi-infinite sink

The real morphology of keratin in wool can be approximated by a square transverse morphology (Fig. 2.3). We assume that the spin-diffusion takes place in a heterogeneous matrix from a source R with low segmental mobility represented by the intermediate filaments into a **semi-infinite sink** M with larger segmental mobility corresponding to the amorphous phase of the keratin.

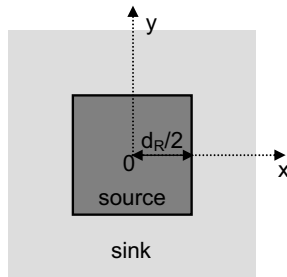**Fig. 2.3** Representation of the square morphology used for the case of finite source and infinite sink

The above morphology is valid only for short spin-diffusion time t i.e., $t < d_R^2 / D_R$, where d_R is the size of the rigid domain R (source of magnetization) and D_R is the spin diffusivity for the R domain. The interfacial region is taken together with the amorphous fraction in the following considerations.

The solution of the spin diffusion equation for the composite medium of finite source and semi-infinite sink can be obtained using the solution for a one-dimensional (1D) composite medium [Cra75, Dem95, Wan96, Buda03b]. For a ε-dimensional diffusion process with $\varepsilon > 1$, the solution of the spin diffusion equation can be written simply as a product of the solutions for the 1D diffusion process [Dem95]. For this the essential condition is that the initial conditions must be expressible as a product of those for the one-variable problems taken separately. The space and time evolution of the concentration of magnetization in the R domain is given by [Dem95]

$$m_R(\vec{r},t) = \frac{\rho_R \sqrt{D_R} m_{R0} + \rho_M \sqrt{D_M} m_{M0}}{\rho_R \sqrt{D_R} + \rho_M \sqrt{D_M}} - \frac{\rho_M \sqrt{D_M}(m_{M0}-m_{R0})}{\rho_R \sqrt{D_R} + \rho_M \sqrt{D_M}} \prod_{i=1}^{\varepsilon} erf\left\{ \frac{d_R/2 - x_i}{\sqrt{4D_R t}} \right\}, \quad (2.22)$$

where x_i are the coordinates of the vector $\vec{r}(x_1,x_2,x_3)$ and $x_i < d_R/2$. The error function is defined as

$$erf(z) = \frac{2}{\sqrt{\pi}} \int_0^z e^{-x^2} dx. \tag{2.23}$$

A high efficient dipolar filter is characterized by the initial concentration of magnetization: $m_{R0} \neq 0$, and $m_{M0} = 0$. For such condition the Eq. (2.22) has the form

$$m_R(\vec{r},t) = \frac{\rho_R \sqrt{D_R} m_{R0}}{\rho_R \sqrt{D_R} + \rho_M \sqrt{D_M}} + \frac{\rho_M \sqrt{D_M} m_{R0}}{\rho_R \sqrt{D_R} + \rho_M \sqrt{D_M}} \prod_{i=1}^{\varepsilon} erf\left\{ \frac{d_R/2 - x_i}{\sqrt{4D_R t}} \right\}. \tag{2.24}$$

Using the results presented in [Dem95] (Eq. 30) and the above Eqs. (2.3), (2.23) and (2.24) we get for the time evolution of the integral intensity of the NMR signal from domain R the relationship

$$\frac{I_R(t)}{I_0} = \frac{\rho_R \sqrt{D_R}}{\rho_R \sqrt{D_R} + \rho_M \sqrt{D_M}} + \frac{\rho_M \sqrt{D_M}}{\rho_R \sqrt{D_R} + \rho_M \sqrt{D_M}} \left\{ 1 - \frac{4\sqrt{D_R t}}{d_R} \left[\frac{1}{\sqrt{\pi}} - ierfc\left(\frac{d_R}{4\sqrt{D_R t}} \right) \right] \right\}^{\varepsilon} \tag{2.25}$$

where the integral error complement function is

$$ierfc(z) = \int_z^{\infty} (1 - erf(x)) dx. \tag{2.26}$$

At the beginning of the spin-diffusion process for short spin-diffusion times t the quantity $\frac{d_R}{\sqrt{D_R t}} \gg 1$ and $ierfc(\infty) = 0$. It is evident from Eq. (2.25) that in the initial regime of the spin-diffusion, i.e., for $t \ll d_R^2/D_R$ the time dependence of the NMR observable $I_R(t)/I_0$ is linear in $\sqrt{t}$ and is given by

$$\frac{I_R(t)}{I_0} \approx \frac{\rho_R \sqrt{D_R}}{\rho_R \sqrt{D_R} + \rho_M \sqrt{D_M}} + \frac{\rho_M \sqrt{D_M}}{\rho_R \sqrt{D_R} + \rho_M \sqrt{D_M}} \left\{ 1 - \frac{4\varepsilon \sqrt{D_R t}}{\sqrt{\pi}\, d_R} \right\}. \qquad (2.27)$$

The tangent to the initial part of the spin-diffusion decay curve described by Eq. (2.27) intersects the $\sqrt{t}$ axis at $\sqrt{t_0}$. The domain thickness d_R for a rectangular 1D, 2D, or 3D morphology is given from Eq. (2.27) by

$$d_R \approx \frac{4\varepsilon}{\sqrt{\pi}} \frac{\rho_M \sqrt{D_R D_M}}{\rho_R \sqrt{D_R} + \rho_M \sqrt{D_M}} \sqrt{t_0}. \qquad (2.28)$$

In the time regime in which the spin diffusion is not affected by the spin-lattice relaxation, the theorem of total magnetization conservation leads to Eq. (2.20). Hence from Eqs. (2.27), and (2.20) the time evolution of the spin-diffusion buildup curve for the sink domain (M) has the same slope as that of the source domain. The intercept of the tangent starting from $t = 0$ with the horizontal line at $I(0)/I_0 = 1$ for the spin-diffusion build-up curve will lead to the same t_0 value as that of the decay curve Eq. (2.28). This is a direct consequence of a finite and semi-infinite morphology. This morphology is a good approximation for the morphology with both finite domains in the initial-rate regime. The thickness of the mobile domain d_M can be obtained by the same procedure discussed above using a Goldman-Shen dipolar filter [Gol66].

We can also note that the derivation of the relationship for d_R (Eq. (2.28)) employs only the solution of the spin-diffusion equation with corresponding initial and boundary conditions. Moreover, the time evolution is considered for the normalized magnetization. This is not the case for the intercept spin-diffusion time reported in [Sch93] and [Van96] where the phase structure considerations and magnetization at equilibrium were taken into account.

2.3 Experimental

2.3.1 Samples

Keratin fibres from 23 μm diameter wool were used for investigating the thermal denaturation of wool keratin. The samples were cut into fine snippets (~2 mm), for ease of handling. The reference sample was soaked in ^2H_2O for one week. The swollen wool fibers were introduced in stainless steel capsules and treated at different temperatures in a DSC instrument (see below). The denaturation process was followed at different temperatures

up to +160° C. The NMR samples were gathered from deuterium oxide-DSC experiments at various times linked to thermal events as disclosed by DSC. Five samples were prepared at the temperatures of 25° C, 134° C, 142° C, 149° C, and 160° C at which NMR measurements were made.

For the investigation of hair keratin denaturation hard α-keratin fibres from Caucasian dark-brown hair, supplied by Kerling International Haarfabrik GmbH, Germany were used. The fibres were cleaned with 1% lauryl ether sulphate (LES) and dried at room temperature prior to work with them. The pH of their aqueous extract was found to be 6.5 to 7.

The damage of the keratin fibres was induced by oxidative and reductive-oxidative chemical treatments, respectively. The oxidative treatment was performed on 1 g keratin fibres with 0.2 g potassium persulphate mixed with 1.2 mL 6% hydrogen peroxide solution to form a paste adjusted at pH 8.5-9 with ammonia. The fibres were covered with the paste, massaged gently between the fingers and left 30 minutes to react at room temperature. The fibres were then rinsed thoroughly until the pH of the aqueous extract was checked to be 7. The treatment was resumed two more times.

The reductive-oxidative treatment was performed with thioglycolic acid (TGA) and hydrogen peroxide. 1 g keratin fibres, pre-wetted with water, were immersed 30 seconds in the reducing solution of 8% w/w TGA at pH 8.5-9 adjusted with ammonia, the solution excess being removed by gently pressing the fibres between the fingers, then covered with plastic folia and let to react for 30 minutes at room temperature. The fibres were then rinsed with tap water (3 minutes) and immersed in the oxidative (hydrogen peroxide 3%) solution adjusted at pH 4.5 with phosphoric acid, for 30 seconds. After squeezing between fingers, fibres were allowed to react with the oxidative solution for 10 minutes, at room temperature. Finally, the fibres were washed thoroughly under tap water for 3 minutes, shampooed for 1 minute (70% Natrium Laurethsulfat, pH 7), washed in warm water for 1 minute, rinsed for 3 minutes in tap water and dried under a steam of hot air. The process has been repeated twice.

The denaturation process was followed at different temperatures up to +180° C. The NMR samples were gathered from deuterium oxide-DSC experiments at various times linked to thermal events as disclosed by DSC. For each chemical treatment four samples were prepared at different temperatures at which NMR measurements were made. Thus, for the Caucasian hair, samples were collected at 145° C, 154.2° C, 160° C, and 180° C, bleached Caucasian hair samples were collected at 122° C, 132.7° C, 140° C, and 180° C,

and permanent treated hair samples were investigated at 140° C, 146° C, 155° C, and 180° C.

2.3.2 Proton and ^{13}C NMR measurements

Proton solid-state NMR spectra, ^{1}H double-quantum (DQ) build-up curves, ^{1}H spin-diffusion, and ^{13}C CPMAS spectra were measured on a Bruker DSX-500 spectrometer operating at 500.45 MHz for ^{1}H, and at 125.84 MHz for ^{13}C. The ^{1}H NMR data were collected at room temperature for non-spinning samples. The dead time of the spectrometer is 5.5 μs. The length of a π/2 pulse was about 5.5 μs, the dwell time was 2 μs, and the recycle delay was 3 s for all measurements.

Proton spin-diffusion measurements were performed following the general scheme consisting of a double-quantum (DQ) dipolar filter, a spin-diffusion period, and an acquisition period as presented in Fig. 2.4. A magnetization gradient was created by the dipolar filter that excites DQ coherences (Fig. 2.4) and selects mainly the magnetization of the rigid phase (fraction) [Buda03a, Buda04]. The DQ excitation sequence is based on two pulses that act during the excitation and reconversion periods. The value of the excitation/reconversion times used in the spin-diffusion experiments was τ = 7 μs. It corresponds to the rising region of the DQ build-up curve for each sample (see below).
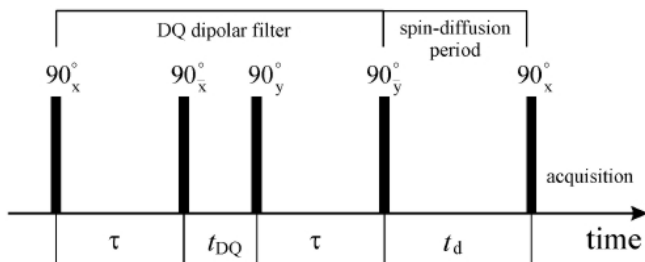
Fig. 2.4 Scheme for the spin-diffusion experiment with a DQ filter. The first two pulses excite DQ coherences that evolve for a short time t_{DQ}. These coherences are converted by the following two pulses into z-magnetization. The spin diffusion takes place during the time interval of duration t_d. The last pulse reads out the distribution of magnetization between different keratin phases.

The experimental wide-line spectra were decomposed into three components using the DMFIT program. The broad component describing the rigid fraction of the spectra was approximated by a Gaussian function. A Lorentzian line shape was employed to describe the narrow component of the spectra corresponding to the mobile phase. A combination of

Gaussian and Lorenzian functions was used to describe the intermediate line corresponding to the interface.

Proton NMR DQ build-up curves were recorded for setting the optimum parameters of the DQ dipolar filter. The DQ evolution time and the z-filter delay were fixed to $t_{DQ} = t_d = 5$ µs (Fig. 2.4).

^{13}C NMR spectra were measured by cross-polarization (CP) magic-angle sample spinning (MAS) with power decoupling by the two-pulse phase modulation (TPPM) method. The contact pulse for CP had a duration of 3 ms.

2.3.3 Differential Scanning Calorimetry (DSC)

The DSC investigations were performed with a DSC 7 from Perkin Elemer, using large volumic, pressure resistant (25 bar), stainless steel capsules (Perkin Elemer). The temperature ranged from 50 to 180° C with a heating rate of 10 K/min, while flushing the chamber with a nitrogen flow of 10 mL/min. The DSC measurement was calibrated with indium and palmitic acid, both of high purity.

Differential scanning calorimetry experiments were carried out, using deuterated water as environment for keratin during heating. For deuterium oxide-DSC experiments, 5-6 mg of snippets were weighted and then transferred into 1 mL deuterium oxide (99.9%) and kept over night to replace of the H_2O moisture. The sample was then placed inside a stainless steel crucible which was sealed with a silicon rubber O-ring, and the peak and enthalpy of the endothermal process were recorded. A minimum of 3 samples was measured to ensure the reproducibility of the DSC data.

2.4 Results and discussion

2.4.1 α-Keratin from wool

2.4.1.1 Thermal denaturation by DSC

A typical DSC plot of a wool keratin fibre in deuterated water is shown in Fig. 2.5. The endothermal process recorded near 140° C is attributed to the thermal denaturation of keratin by melting of the crystalline α-helix structure [Pop07, and references tehrein]. The peak is quite different from keratin in a water environment, where the endothermal process

appears as a doublet (peaks around 138 and 144° C), attributed to the denaturation of α-helices in ortho and para cells which form wool cortex [Deu98]. This difference between the experiments in water and deuterated water suggests that hydrogen bonds play a significant role in the thermal denaturation process of wool, and supports the model of interface scaffolding in the crystalline part which was recently proposed for keratin fibres [Ist08]. The scenario for the thermal denaturation of hydrated keratin as reflected in the DSC and NMR data is discussed below.
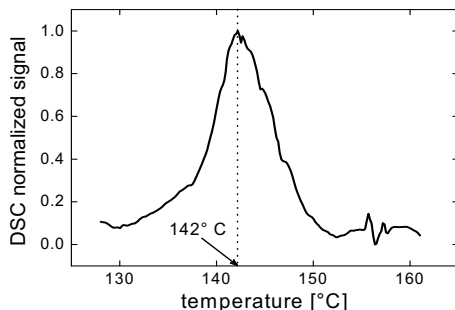
Fig. 2.5 Normalized DSC signal of a wool sample in D_2O for the temperature range of denaturation.

2.4.1.2 Proton NMR spectra and phase composition

Proton NMR spectra of hydrated wool keratin samples denaturated at different temperatures, recorded under static conditions, are presented in Fig. 2.6. The best fit parameters have been found by decomposing the spectra into three lines, i.e. a Gaussian, a Lorenzian, and a combination of a Gaussian and a Lorenzian function. The broad component, associated with the Gaussian line, corresponds to the rigid phase. The Lorenzian line associated with the narrow component of the spectra describes the mobile phase. The intermediate line, described by the combination of Gaussian and Lorenzian functions is associated with the interface.
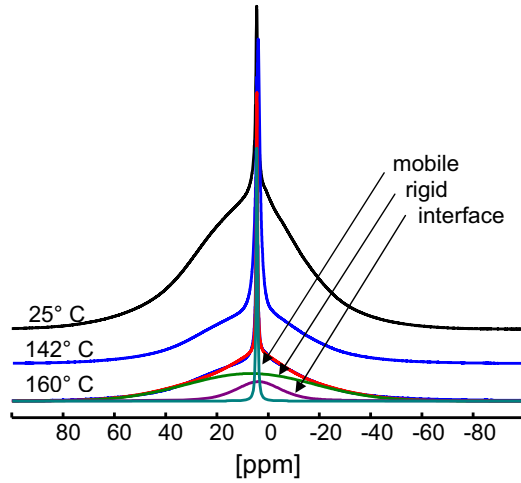
Fig. 2.6 Proton NMR spectra of native (25° C) and denaturated wool keratin fibres at temperatures 142° C and 160° C. All spectra were decomposed into three components corresponding to the rigid, semi-rigid (interface) and mobile fractions.

The phase composition of the investigated hydrated wool keratin samples is shown in Fig. 2.7 as a function of the denaturation temperature. The measurements reveal a decrease of the rigid phase at the expense of the mobile phase in the temperature region where the denaturation process occurs. The phase (fraction) composition at temperatures higher than 142° C is similar to (but not identical) with the one measured at ambient temperature.
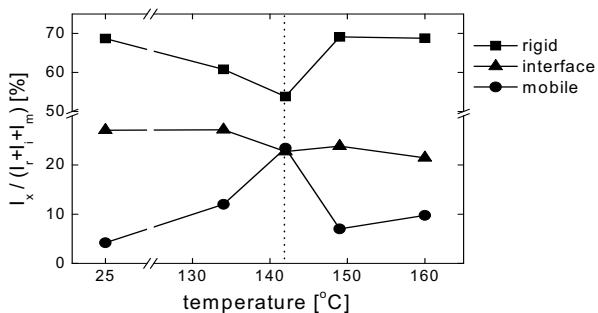
Fig. 2.7 The phase (fraction) composition of hydrated keratin wool fibers at different denaturation temperatures.

2.4.1.3 Double-quantum dipolar filter for ^{1}H spin-diffusion

Spin-diffusion experiments observe the equilibration of a spatially heterogeneous magnetization distribution across the sample. A gradient in the magnetization can be created, for example, with a dipolar filter which excites double-quantum (DQ) coherences [Buda03b]. This type of filter is more advantageous than a dipolar filter for mobile domains because it allows a more accurate detection in terms of the narrow signals on top of a broad component than in terms of a broad component under a narrow signal. This is valid especially at short diffusion times when the magnetization of one of the components is very small.

The DQ filter can be set such to select the magnetization only from the most rigid part of a heterogeneous sample. By choosing appropriate excitation/reconversion periods τ (Fig. 2.4) of the double-quantum coherences originating from the magnetization of the stronger dipolar couplings will pass through the filter while the signal of the weaker dipolar couplings is filtered out. The optimum value of τ is chosen from DQ build-up curves as shown in Fig. 2.8 for non-denatured (25° C) and denatured (160° C) wool samples. The DQ build-up curves were recorded with the five-pulse sequence and a spin-diffusion time of $t_d = 5$ μs (Fig. 2.4). The maxima in the curves appear at very short excitation/reconversion times τ of about 10-12 μs for all investigated wool samples. In this range of τ values, the mobile component is completely filtered out as shown below. This shows that ^{1}H dipolar couplings are larger for the native sample than for the sample denatured at 160° C. The slope of the DQ build-up curves in the initial regime of the excitation/reconversion times is related to the residual second van Vleck moment of the rigid fraction [Ern90]. Figure 2.8 shows that the residual dipolar interactions change to some extent during the denaturation process. The maximum of the DQ build-up curve of the native sample is slightly shifted to smaller τ values compared to the denatured samples. This indicates that ^{1}H dipolar couplings are larger for the native sample than for the sample denatured at 142° C. The average proton-proton distances inside the collapsed intermediate filaments become larger than those in the native sample.
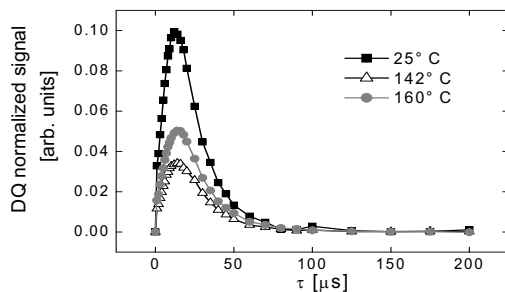
Fig. 2.8 Normalized ^1H DQ signals for native and denatured wool keratin samples at different denaturation temperatures.

DQ filtered NMR spectra recorded for different values of the excitation/reconversion times τ are shown in Fig. 2.9 for the non-denaturated sample. For short τ values, the DQ filtered ^1H spectrum edits mainly the spin-pairs with the strongest dipolar couplings (Fig. 2.9a). In the region of the maximum of the DQ build-up curves, the pulse sequence edits a dipolar network of many spins corresponding to the crystalline and partially the interface fraction (Fig. 2.9b). The ^1H spectrum in Fig. 2.9c filtered only the keratin from the amorphous fraction. The value of $\tau = 5$ µs has been chosen for the dipolar filter of the rigid domain, which still keeps the filter efficiency close to unity with a reasonable value of the signal–to–noise ratio.
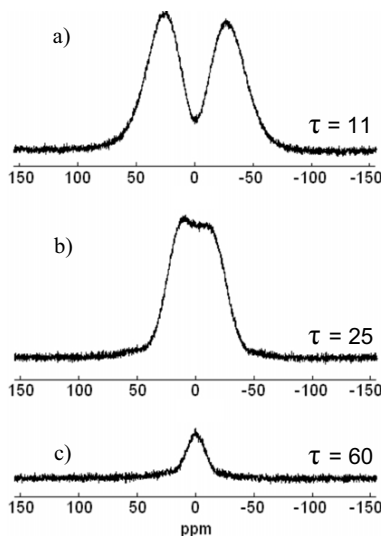
Fig. 2.9 Proton DQ filtered NMR spectra recorded for different values of the excitation/reconversion time **(a)** $\tau=11$ µs, **(b)** $\tau= 25$ µs, and **(c)** $\tau= 60$ µs (Fig. 2.4).

2.4.1.4 Proton residual second van Vleck moments

The determination of the residual second van Vleck moment by DQ build-up curves (Fig. 2.8) was reported in [Buda03a], and the resultant values are summarized in Tab. 2.1. Similar to the spin diffusivities, the second van Vleck moment $<M_2>$ has the lowest value for the the keratin fibers which were heated to the denaturation temperature. A decrease in strength of the dipole-dipole interaction is observed in connection with the loss of rigidity in the temperature range of the denaturation process.

Table 2.1 Proton second van Vleck moments for native and thermally denatured hydrated keratin fibers.

T [° C]	$<M_2>$ [10^9 Hz^2]
25	5.96
142	2.14
160	2.7

2.4.1.5 Proton spin diffusivities

An accurate analysis of the thickness of domains by NMR spin-diffusion experiments requires three steps. These are: (i) an optimization of a dipolar filter to obtain the highest selectivity to the different phases, (ii) knowledge of the spin-diffusion coefficients for modelling the experimental data, and (iii) proper choice of a model that describes the morphology of the studied material. The spin-diffusion coefficients can be expressed in terms of the local dipolar field, so that the spin diffusivities are related to the second van Vleck moments.

The values of the spin-diffusion coefficients D_R and D_M for the rigid and soft fractions, respectively, can be determined by approximating the corresponding NMR line shapes by Gaussian and Lorentzian functions, respectively. The spin-diffusion coefficients can be related to the second van Vleck moment of the NMR absorption lines, which, in turn, are related to the full line width $\Delta\nu_{1/2}$ at half height.

The equations describing the spin-diffusion coefficients for rigid (Gaussian line) and mobile (Lorentzian line) regions are given by [Dem95],

$$D_R = \frac{1}{12}\sqrt{\frac{\pi}{2\ln 2}}\left\langle r^2 \right\rangle \Delta\nu_{1/2}, \tag{2.28}$$

and

$$D_{\mathrm{M}} = \frac{1}{6}\left\langle r^2 \right\rangle \left[\alpha\Delta\nu_{1/2}\right]^{1/2}, \tag{2.29}$$

where α is the cut-off parameter of the Lorentzian line, $\Delta\nu_{1/2}$ is the full line width at half height, and $<r^2>$ is the mean square distance between the nearest spins. An estimation of $\left\langle r^2 \right\rangle^{1/2} \approx 0.22$ nm was given for wool keratin, taking into account the amino acid composition [Per95].

The spin-diffusion coefficients calculated from Eq. (2.28) and (2.29) are shown in Fig. 2.10. The values of the spin-diffusion coefficient for the region composed of the mobile and interface fractions decrease in the temperature range where the denaturation process occurs. This region can be interpreted as disordered keratin fibrils with larger interproton distances. A reorganization that increases the degree of packing will lead to higher denaturation temperatures and larger values of spin diffusivitiy.
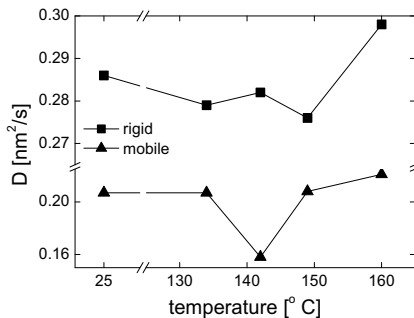
Fig. 2.10 Effective ^{1}H spin-diffusivities evaluated from Eq. (2.28) and Eq. (2.29) for the phases of wool keratin as a function of the denaturation temperature.

2.4.1.6 Morphology and domain sizes

The spin-diffusion experiments were performed on keratin fibers after they were heated to the following temperatures: 25° C, 134° C, 142° C, 149° C, and 160° C. Proton wide-line NMR spectra recorded at three different diffusion times t_{d} are shown in Fig. 2.11. In all cases the flow of magnetization from the rigid domain into the mobile domain is observed with increasing diffusion times. At short diffusion times mainly the rigid fraction of keratin composed of the α-helical conformation of the intermediate filament is observed, and can be seen in Fig. 2.11 for $t_{\mathrm{d}} = 25$ μs. Upon increasing the spin-diffusion time, the relative intensity of the rigid fraction in the spectra decreases, and the intensity of the narrow line

that originates from the soft amorphous fraction represented by the keratin matrix surrounding the intermediate filament increases.
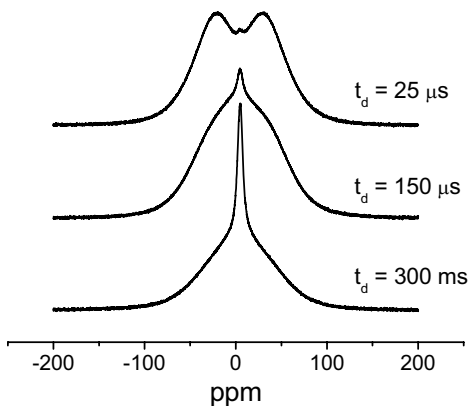
Fig. 2.11 Proton wide-line NMR spectra recorded at three different spin-diffusion times t_d after the action of the DQ dipolar filter (Fig. 2.4).

The presence of the mobile amorphous regions complicates the interpretation of the spin diffusion data. Due to the fact that it is less than 10% for all samples and that the flow of magnetization reaches it only after longer spin-diffusion times, our approach will mainly focus on the transfer of magnetization between the crystalline and the less-mobile amorphous regions. Therefore, a renormalization of the integral intensities corresponding to these two phases was made by adding the signal of the amorphous phase to the signal of the interface. The time evolution of the nuclear magnetization for native and denaturated samples with increasing spin-diffusion time is shown in Fig. 2.12 for the rigid and less rigid fraction of the keratin fibres. The quasi-equilibrium is reached after about 4 ms.
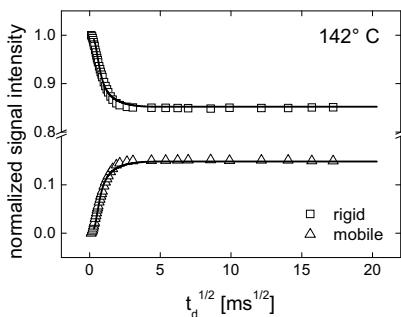
Fig. 2.12 The normalized signal intensities obtained by a ^1H spin-diffusion experiment (Fig. 2.4) for a wool fiber denaturated at 142° C.

22

To estimate the domain sizes for the rigid and less-mobile amorphous domains from the spin-diffusion data, two different morphology models were analysed, the two-dimensional (2D) square morphology and the 2D cylindrical morphology. The domain sizes of hydrated keratin derived with the ^{1}H spin diffusivity shown in Fig. 2.10 are presented in Fig. 2.13 for different denaturation temperatures. Both morphologies lead to similar results within the limit of experimental error. The rigid domain size increases at the denaturation temperature of 142° C and the thickness of the mobile domains including the interfaces decreases. These findings are in agreement with the thermal denaturation scenario discussed below.
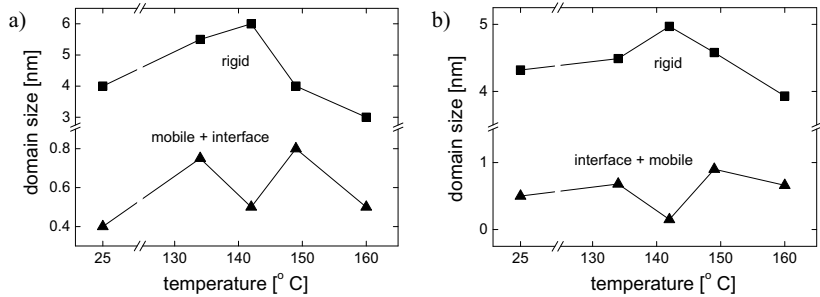
Fig. 2.13 Domain sizes for the rigid and mobile + interface fractions of wool keratin as a function of the denaturation temperature. The solutions for the spin-diffusion equations for square **(a)** and cylindrical **(b)** morphologies were used for the evaluation of domain sizes.

2.4.1.7 Dynamic heterogeneity of hydrated keratin fibre interface

The ^{1}H spin-diffusion experiment with a DQ filter was made on the wool fibres denaturated at different temperatures. The evolution of the z-magnetization front was analyzed by decomposing the NMR spectrum into components. At the beginning of the spin-diffusion experiment the magnetization is stored only in the rigid domain. For short spin-diffusion times the magnetization moves only into the interface and at the longer diffusion times, it reaches the mobile region. The average distance $\left\langle z^2 \right\rangle^{1/2}$ travelled by the [1]H z-magnetization can be estimated with Einstein relationship in one dimension, i.e.,

$$\left\langle z^2 \right\rangle^{1/2} = 2\left(\frac{D_R + D_M}{2} \right) t_d, \tag{2.30}$$

where $\dfrac{D_R + D_M}{2}$ is the average spin diffusivity, and t_d is the spin-diffusion time.

The interfacial region has a gradient in molecular mobility, and a monotonic change in the line-width at the half-intensity can be detected. At small spin-diffusion times, the experiment edits the part of the interface close to the rigid region, and at longer diffusion times the more mobile part of the interface connected to the mobile region. The line-width $\Delta v_{1/2}$ of the interface component at half-intensity changes gradually (Fig. 2.14). It is evident that the mobility gradient of the interface is almost the same for the native hydrated wool sample and the sample denaturated at 160° C. The largest gradient in the molecular mobility of about 6 kHz/nm is seen for the keratin proteins at the denaturation temperature of 149° C. For all the other temperatures the gradient in mobility of the interfacial region is around 0.6 kHz/nm.
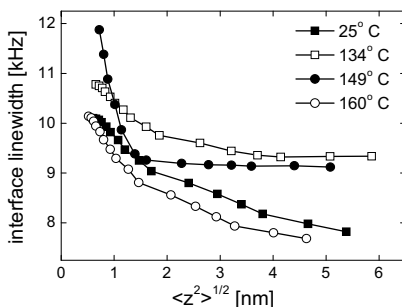
Fig. 2.14 Full line-width at half intensity of the interfacial component of the ^{1}H NMR spectrum for wool fibers as a function of the average spin-diffusion distance $<z^2>^{1/2}$ for different denaturation temperatures.

2.4.1.8 ^{13}C CPMAS spectra of thermally denaturated wool keratin

Cross-polarization (CP) MAS ^{13}C spectra of hydrated wool keratin denaturated at different temperatures are shown in Fig. 2.15. These spectra are similar to those reported for α-keratin of equine hoof under hydrated condition [Per95]. Many spinning-sidebands not reported before are present in these spectra due to the large values of the ^{13}C chemical shielding anisotropy (Fig. 2.15a). The ^{13}C spectra show several distinct regions: (i) the carbonyl region with a maximum at 173 ppm, (ii) a broader signal due to the α-carbons at 54 ppm, (iii) a peak at 40 ppm with a contribution from β-carbon in leucine residues and the β-carbon in crosslinked cysteine residues, and (iv) a complex lineshape in the 10-35 ppm region due to alkyl components of the side-chains (Fig. 2.15b). The assignment was made following the ^{13}C isotropic chemical shifts for the common amino acid residues reported in [Per95].
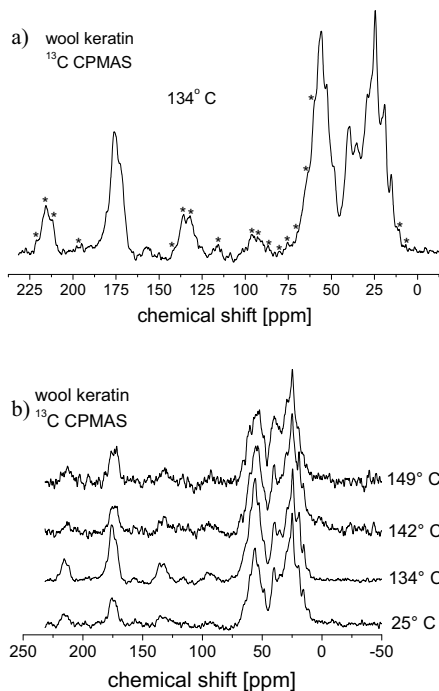
Fig. 2.15 (a) ^{13}C CPMAS spectrum of keratin fiber at 134° C where the spinning sidebands are marked by stars. **(b)** ^{13}C CPMAS spectra of hydrated wool keratin as a function of the denaturation temperature.

The ^{13}C CPMAS spectra from Fig. 2.15b show that the lineshape of the carbonyl signal changes significantly with increasing denaturation temperature. Growing disorder of the intermediate filaments leads to a broadening of the resonances starting at the denaturation temperature of 142° C. This disorder induces ^{13}C chemical shielding tensors with different orientations of principal reference frames relative to the laboratory frame leading to the line broadening. The broadening of the ^{13}C carbonyl resonance suggests a shift in the conformation of α-helix components in the hydrated keratin towards more extended configuration related to coil conformation [Per95]. In the investigated thermal denaturation temperature range, the amino acid residue composition does not change and therefore, the change in the carbonyl lineshape must result from changes in the keratin conformation.

The region of the alkyl and α-carbon regions is enlarged in Fig. 2.16. The peak at 40 ppm is related to the β-carbon in crosslinked cysteine residues. These cysteine residues

25

participate in the -S-S- disulfide links between neighbouring keratin molecules. The intermolecular disulfide links between cysteine residues confer some degree of rigidity to the intermediate filaments in the amorphous component of the α-keratin matrix. The broadening of the ^{13}C resonances at 40 ppm and a temperature of 149° C, which is over the denaturation temperature of 142° C, strongly suggest an increased heterogeneity of hydrated keratin due to the braking of a significant number of such –S-S- crosslinks during the denaturation process. Additional non-fully resolved resonances in the 32-40 ppm region are due to glutamic acid, glutamine and proline residues. Moreover, the spectral region at around 54 ppm is almost entirely associated with a random coil keratin structure whilst the higher frequency region is associated with α-helical conformations.
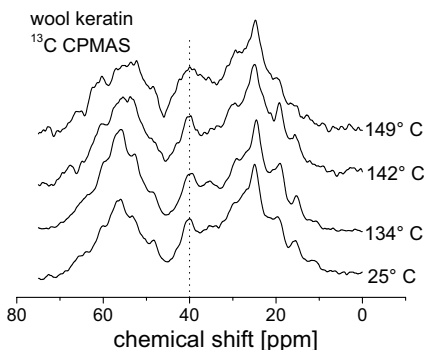
Fig. 2.16 Enlarged version of the alkyl and α-carbon regions of the ^{13}C CPMAS spectra of Fig. 2.15b for different denaturation temperatures. The dashed line at 400 ppm marks the ^{13}C resonance of the cysteine engaged in the disulfide links.

2.4.1.9 Morphological changes induced by thermal denaturation as seen by NMR data

The model in Fig 2.17a gives a simplified scheme of a microfibril with protofibrils showing the α-helical rods and the non-helical terminal domains projecting into the interfilamentous space and linking with the matrix proteins through disulfide bonds. The terminal domains contain, besides cystine, glycine, threonine, valine, alanine and serine, acidic sites as glutamic and aspartic acid. In this way, the electrostatic forces may well play a role for the stability of IFs in the native fibre. This scaffolding structure at the IFs surface made by the side-chain interactions that anchor microfibrils to the matrix (interface phase) assists the thermal stability and the primary control over the denaturation of the helical

structure of keratin materials when heated. It has a protective role and the capacity to participate in the formation of a solid interface.
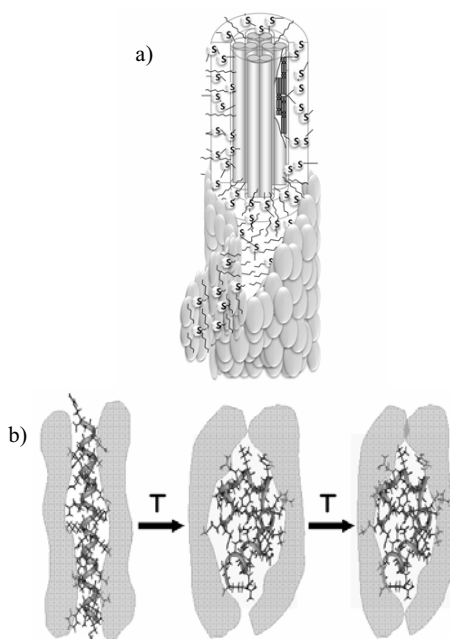
Fig. 2.17 (a) Schematic representation of the intermediate filament imbedded in the amorphous keratin matrix. The wavy lines show the disulfidic bonds. **(b)** Sequence of frame representations of a keratin α-helix imbedded in an amorphous keratin matrix (grey areas) during thermal denaturation. The keratin system at ambient temperature is shown on the left. At the denaturation temperature of 142° C the keratin α-helix folds (middle). The reduction in the transverse average diameter of the rigid domain due to keratin reorganization is shown on the right.

The mechanism of thermal denaturation of keratins should therefore follow several steps (Fig. 2.17b). Beyond a certain temperature (around 130° C) the temperature rise leads to the break-up of the scaffold structure of the IFs. At that temperature the IFs are in a meta-stable state as shown in the left hand frame of Fig. 2.17b. The α-helix denaturates around at 80° C into soluble proteins, and it is only the interface that keeps it still organised. Once set free, the IFs (α-helices) denaturate. This involves a transition from a relatively compact ordered structure to a more flexible, disorganized, opened polypeptide chain (middle frame of Fig. 2.17b). As the process of denaturation proceeds the protein molecules unfold (right hand frame of Fig. 2.17b) and the internal, hydrophobic regions expose to the outside of the molecules. The hydrophobic groups in water tend to cluster, leading to associations of molecules.

2.4.2 α-Keratin from hair

2.4.2.1 Thermal denaturation by DSC

Typical DSC plots in D_2O for the temperature range of denaturation of hard α-keratin in the untreated state, after oxidative, and after reductive & oxidative treatment respectively, are shown in Fig. 2.18. The endothermal process recorded around 140° C for the untreated sample is attributed to the thermal denaturation of keratin by melting of the α-helix crystalline structure [Van96]. The scenario for the thermal denaturation of hard α-keratin in the native form and after chemical treatments as reflected in the DSC and NMR data is discussed below.
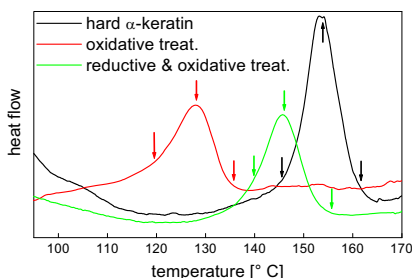
Fig. 2.18 DSC signals of hard α-keratin, in the native state, after oxidative, and reductive & oxidative treatments in D_2O for the denaturation temperature range. The arrows mark the temperatures at which the samples were collected to be used in the NMR measurements.

2.4.2.2 Proton NMR spectra, phase composition and molecular dynamics

The proton NMR spectrum of hard α-keratin, recorded in static conditions at room temperature, is presented in Fig. 2.19. The spectra were decomposed into three components corresponding to the rigid, interface and the mobile phase, as described in Section 2.4.1.2.
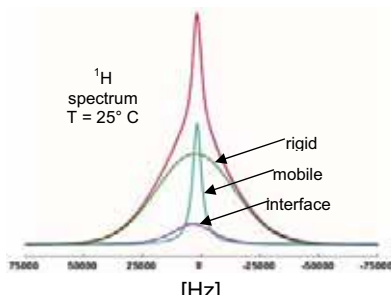
Fig. 2.19 Proton wide-line NMR spectrum of hard α - keratin. All NMR spectra were decomposed into three components corresponding to the rigid, semi-rigid (interface) and mobile fractions.

The phase composition for hard α-keratin, in the native state, after oxidative, and reductive & oxidative treatments in D_2O for the temperature range where the denaturation takes place is shown in Fig. 2.20. The denaturation temperature of hard α-keratin is 155° C, for the hair samples after the oxidative treatment is 144° C and for the sample subjected to reductive & oxidative treatment is 128° C. The measurements reveal a slight increase in the relative amount of rigid phase and a decrease of the interface for hard α-keratin. We can note the opposite behaviour for the sample after the oxidative and reductive & oxidative treatments. The amount of mobile (amorphous) fraction is essentially not affected by the denaturation temperature. The reductive & oxidative treatment increases the relative amount of rigid fraction at the expense of interface compared to the hard α-keratin.
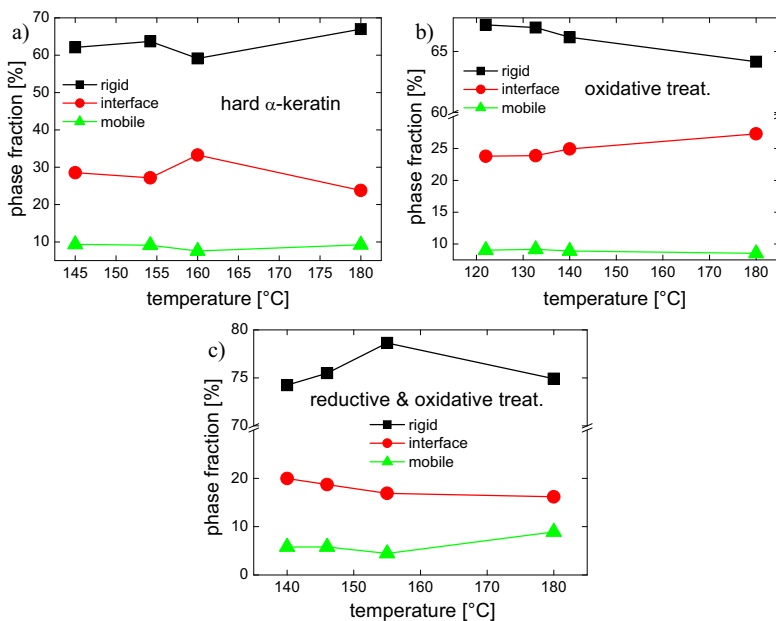
Fig. 2.20 The phase composition of hard α-keratin, in **(a)** the native state, **(b)** after oxidative, and **(c)** reductive & oxidative treatments for different temperature ranges.

The molecular dynamics measured in terms of the linewidth of the ^{1}H spectral components of hard α-keratin, after oxidative, and reductive & oxidative treatments for the temperaturee range where denaturation occurs is shown for the rigid, interface, and mobile fractions in Fig. 2.21. In general, denaturation at 180° C induces a greater disorganization in the nanostructured keratin and hence a large molecular mobility. An exception is the

mobile fraction of the sample after reductive & oxidative treatment. The molecular motion is strongly hindered by the matrix disorganization induced by this chemical treatment. The molecular motions are more hindered for the rigid phase and interface of hard α-keratin.
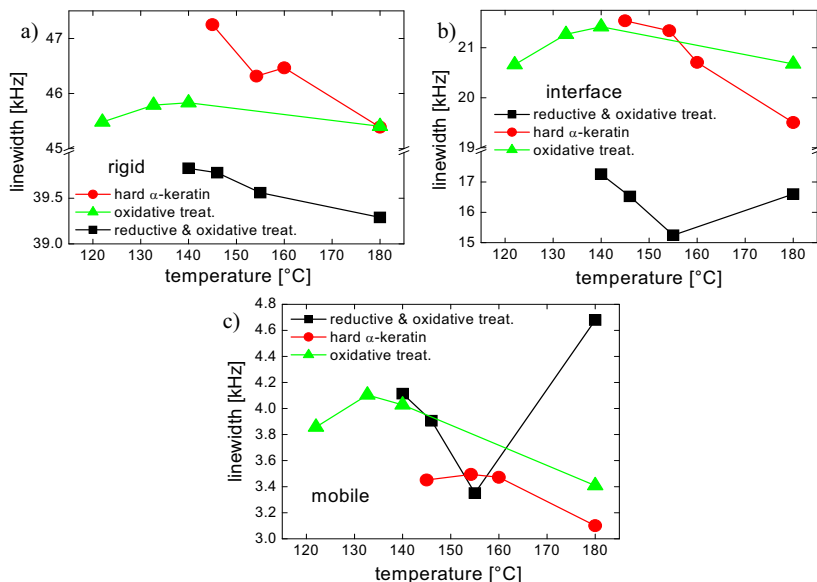
Fig. 2.21 The full line-width at half intensity of the NMR spectral components corresponding to rigid, interface, and amorphous fractions of hard α-keratin, in the native state, after oxidative, and reductive & oxidative treatments for different temperature intervals.

2.4.2.3 Double-quantum dipolar filter for ^{1}H spin-diffusion

The DQ filtered NMR spectra recorded for different values of the excitation/reconversion times τ are shown in Fig. 2.22 for hard the α-keratin sample. For short τ values the DQ filtered ^{1}H spectrum edits mainly the spin-pairs of aminoacids with the strongest dipolar couplings (Fig. 2.22a). In the region of the maximum of the DQ build-up curves the pulse sequence edits a dipolar network of many spins corresponding to the crystalline and partially the interface fraction (Fig. 2.22b). The ^{1}H spectrum in Fig. 2.22c filtered only the mobile keratin from the amorphous fraction. The value of τ=5 μs has been chosen for the dipolar filter of the rigid domain, which still keeps the filter efficiency close to unity with a reasonable value of the signal–to–noise ratio.
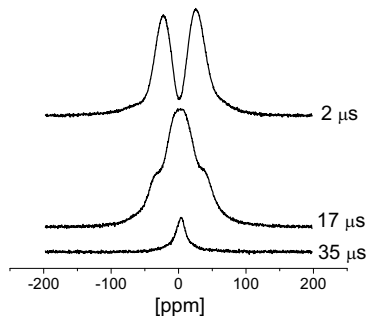
Fig. 2.22 Proton DQ filtered NMR spectra recorded for hard α-keratin at different values of the excitation/reconversion times **(a)** τ=2 μs, **(b)** τ= 17 μs, and **(c)** τ= 35 μs.

2.4.2.4 Proton spin diffusivities

The calculated spin-diffusion coefficients using Eqs. (2.28) and (2.29) are shown in Fig. 2.23. For each denaturation temperature and type of sample the specific values of $D_{R,}$ and D_M are used for domain size evaluation. The largest value for $D_{R,}$ showing the highest organization and packing corresponds to hard α-keratin (Fig. 2.23a). The morphology dezorganization due to reductive & oxidative treatment leads to a reduction of D_R at the denaturation temperature. This trend is also valid for D_M (Fig. 2.23b).
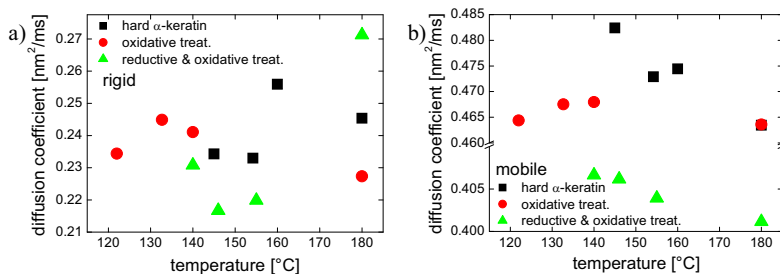
Fig. 2.23 Effective ^{1}H spin-diffusivities D_R **(a)** and D_M **(b)** evaluated from Eq. (2.28) and Eq. (2.29) for different hard α-keratin as a function of the denaturation temperature.

2.4.2.5 Morphology and domain sizes

The spin-diffusion experiments were performed on native hard α-keratin and chemically treated samples after they were heated at the temperatures shown in Fig. 2.18. Proton wide-line NMR spectra recorded at three different diffusion times t_d are shown in Fig. 2.24. In all cases the flow of magnetization from the rigid domain into the mobile domain is observed with increasing diffusion times. At short diffusion times mainly the rigid fraction

of keratin composed of the α-helical conformation of the intermediate filament is observed, and can be seen in Fig. 2.24 for t_d=40 µs. Upon increasing the spin-diffusion time, for example at t_d=250 µs and t_d=600 ms, the relative intensity of the rigid fraction in the spectra decreases, and the intensity of the narrow line that originates from the soft amorphous fraction represented by the keratin matrix surrounding the intermediate filament increases (Fig. 2.24).
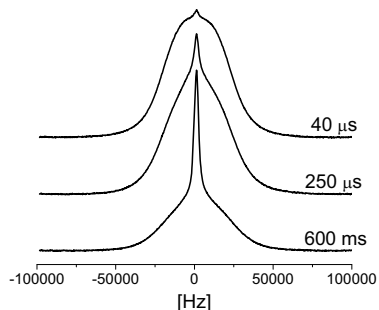
Fig. 2.24 Proton wide-line NMR spectra recorded at three different spin-diffusion times t_d of 40 µs, 250 µs, 600 ms after the action of the DQ dipolar filter (Fig. 2.4).

A renormalization of the integral intensities of the fractions was done as described in Section 2.4.1.6 and thus we shall only focus on the transfer of magnetization between the crystalline and the less-mobile amorphous regions. The time evolution of NMR observables for the reductive & oxidative treated hard α-keratin sample with increasing spin-diffusion time is shown in Fig. 2.25 for the rigid and less rigid fractions. The quasi-equilibrium is reached after about 4 ms that is less than the longitudinal relaxation times.
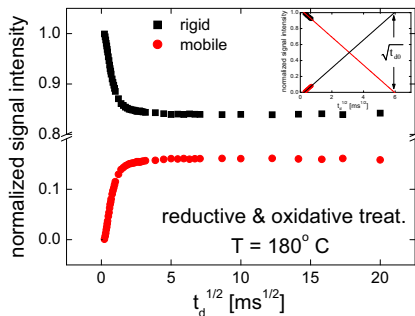
Fig. 2.25 The normalized signal intensities for ^{1}H spin-diffusion experiment (Fig. 2.4) for a hard α-keratin after the reductive & oxidative treatment and denatured at 180° C. The initial slope and the intercept at $\sqrt{t_{d0}}$ is shown in the inset.

To estimate the domain sizes for the rigid and less-mobile amorphous domains based on the analysis of spin-diffusion data using initial rate approximation (Sec. 2.2.4). The symmetric display of $\sqrt{t_{d0}}$ is shown in the insert of Fig. 2.25 and the two-dimensional (2D) morphology ($\varepsilon = 2$) is considered in Eq. (2.28). The values of $\sqrt{t_{d0}}$ for hard α-keratin, in the native state, after oxidative, and reductive & oxidative treatments for range of the denaturation temperature are given in Fig. 2.26.
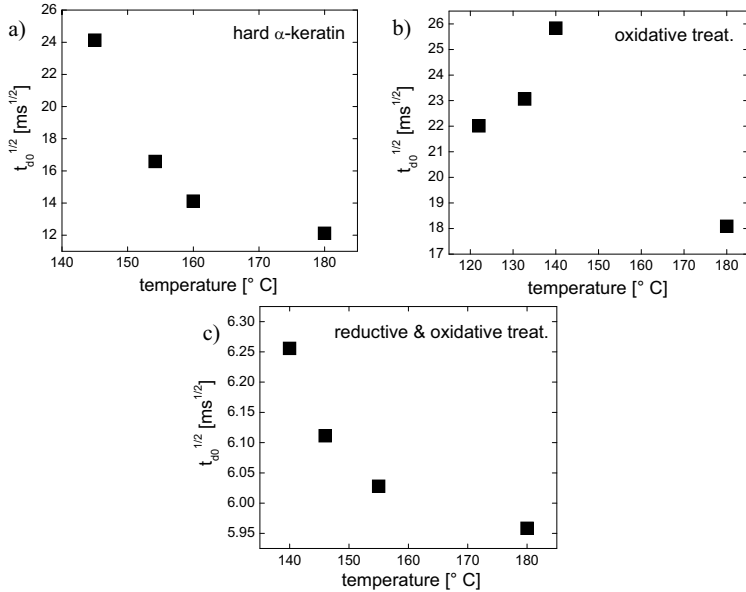
Fig. 2.26 The denaturation temperature dependence of the intercept $\sqrt{t_{d0}}$ for hard α-keratin, in the native state, after oxidative, and reductive & oxidative treatments.

The rigid domain thickness of hard α-keratin samples for different denaturation temperatures are presented in Fig. 2.27. It is evident that in the case of reductive & oxidative treatment of hard α-keratin the rigid domains do not change in the limit of experimental errors with the denaturation temperatures. Moreover, the disorganization in the intermediate filaments will reduce the domain size as compared to hard α-keratin and the sample submitted to the oxidative treatment by about 50%. For the last two samples d_R decreases for the largest denaturation temperature.
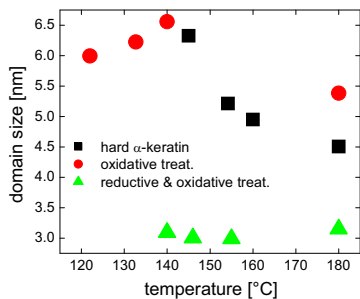
Fig. 2.27 Rigid domain sizes for rigid and mobile+interface fractions of hard α-keratin with different treatments as a function of denaturation temperature.

2.4.2.6 Dynamic heterogeneity of hard α-keratin fiber interface

The changes in the line-width at the half-intensity $\Delta v_{1/2}$ of the interface spectral component is shown in Fig. 2.28 for hard a-keratin at different temperatures before and after the denaturation temperature of 154° C. It is interesting that the dynamic heterogeneity of the interface shows a maximum in the molecular mobility. This is more pronounced for the hard α-keratin denatured at T=154° C. The width of the molecular mobility heterogeneity measured in units of the spin-diffusion time is almost the same for different temperatures around the DSC denaturation peak (Fig. 2.18). Moreover, heterogeneity of the molecular dynamics at the interfacial region in hard α-keratin at the extreme temperatures of 145° C and 180° C before and after the DSC peak is almost the same showing a reorganization of the morphology after denaturation occurs. Nevertheless, this is not complete because the molecular dynamics at T=180° C is slightly faster compared to that at T=145° C as it is evident from the right hand side of Fig. 2.28.
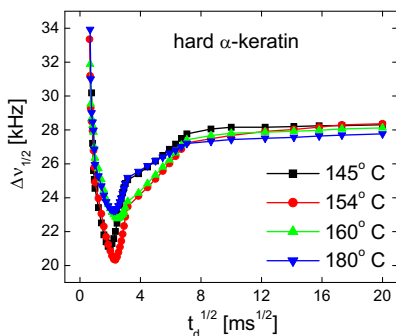
Fig. 2.28 Full line-width at the half intensity of the interfacial component of the ^{1}H NMR spectrum for hard α-keratin measured at different denaturation temperatures.

2.4.2.7 13C CPMAS spectra of chemically treated hard α-keratin

Cross-polarization (CP) MAS ^{13}C spectra of hard α-keratin, in the native state, after oxidative, reductive & oxidative and disulfide bonds scission treatments at room temperature are shown in Fig. 2.29 and 2.30. These spectra are similar with those reported for α-keratin of equine hoof under hydrated condition [Due03] and thermally denaturated wool keratin as described in Section 2.4.1.8 [Bai09]. Many spinning-sidebands are present in these spectra due to the large values of the ^{13}C chemical shielding anisotropy (cf. Fig. 2.29).
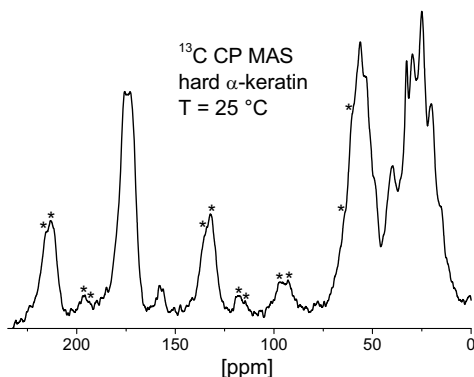
Fig. 2.29 ^{13}C CPMAS spectrum of hard α-keratin at the rotor frequency of 5 kHz where the spinning sidebands are marked by asterix.

In Fig. 2.30a is a zoom of the alkyl and α-carbon regions. The α-carbon shows an increase of intensity, expressed by the shoulder at around 64 ppm, noticeable for the hard α-keratin subjected to oxidative treatment. The peak at 40 ppm is related to the β-carbon in crosslinked cystine residues. They participate in the -S-S- (disulfide) bonds between neighbouring keratin molecules. The intermolecular disulfide links between cysteine residues confer some degree of rigidity to the intermediate filaments in the amorphous matrix component of α-keratin. The intensity and the broadening of the resonance at 40 ppm ^{13}C does not change significantly with the chemical treatment with the exception of the sample where the sulphur of the broken S-S bond was acetylated for arresting its reactivity. This sample has a lower intensity of ^{13}C resonance at 40 ppm compared to the other samples. Moreover, resulting reduced cysteine residues would be expected to have a β-carbon resonance between 25 ppm and 29 ppm that is indeed revealed in Fig. 2.30a.
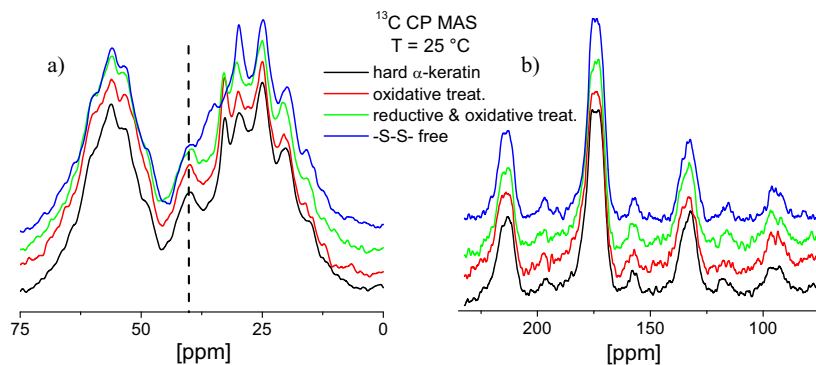
Fig. 2.30 Enlarged version of the alkyl **(a)** and α-carbon **(b)** regions of the ^{13}C CPMAS spectra at the rotor frequency of 5 kHz for hard α-keratin, in the native state, after oxidative, and reductive & oxidative treatments. The dashed line at 40 ppm marks the ^{13}C resonance of the cysteine engaged in the disulfide links. The ^{13}C CPMAS spectrum of the sample free of –S-S- bonds is also shown.

The ^{13}C CPMAS spectra from Fig. 2.30b show that the lineshape of the carbonyl signal has not changed significantly with chemical treatments. This indicates that the amino-acid chains (the keratin molecules) are not significantly damaged (hydrolysed) by our treatments. A larger degree of disorder of the intermediate filaments would lead to a broadening of the resonances. This disorder will induce ^{13}C chemical shielding tensors with different orientations of the principal reference frames relative to the laboratory frame leading finally to the line broadening. The broadening of the ^{13}C carbonyl resonance would suggest a shift in the conformation of the α-helix components. For the investigated chemical treatments the amino acid residue composition does not change and therefore, the lack of the changes in the carbonyl lineshape shows basically the same conformation of the hard α - keratin. This does not stand for the case of hard α-keratin with acetylated sulphur where the linewidth of the carbonyl signal is slightly larger than the others, suggesting that the acetylation of sulphur after breaking the disulphide bond induced a certain degree of disorder in the hard α-keratin. This supports our view of a three-phase model for the hard α-keratins, where the interface, mainly cystine based, scaffolds the intermediate filaments (the rigid phase). The breaking of the cystine and the arresting of the reactive formed thiols by acetylation fragments the scaffold and deprives the intermediate filaments of their mechanical support.

2.4.2.8 Morphological changes induced by chemical and thermal treatments as seen by DSC and NMR data

The chemical modifications we used for the keratin material were focused on attacking the disulphide bonds. The oxidative modification aims at breaking the S-S bonds and oxidise them into cysteic acid (see Fig. 2.31a). Under the reaction conditions not all the bonds will be broken but, overall, it is expected that both the scaffold and the matrix are crumbled. As a result the DSC peak corresponding to the denaturation of protein shifts towards lower temperature (around 130° C, see Fig. 2.18) and the enthalpy decreases compared to the original keratin material. The interface amount for oxidative modification is reduced as compared to the hard α-keratin as shown in Figs. 2.20a and b. Moreover, the molecular dynamics of side chains are intermediate between that of hard α-keratin and the sample subjected to the reductive & oxidative treatment (cf. Fig. 2.21). The rigid domain thickness is not essentially affected by the oxidative treatment (Fig. 2.27).
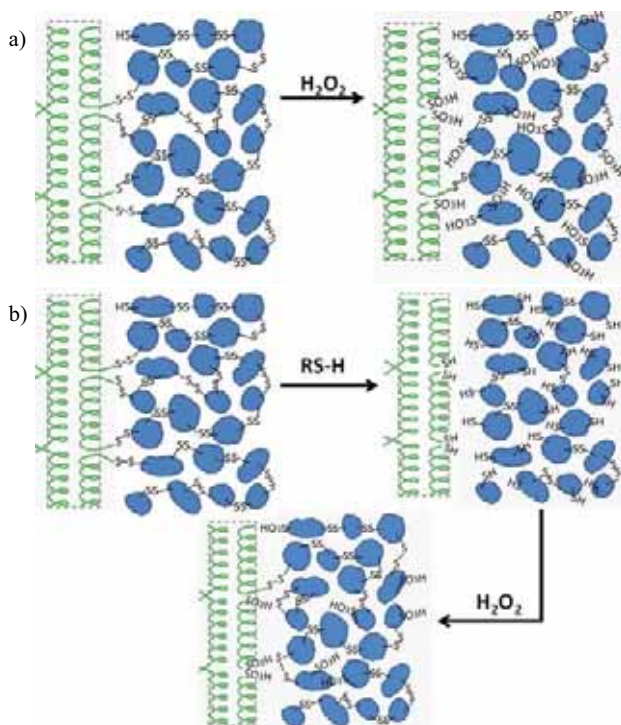
Fig. 2.31 Schematic representation of the intermediate filament (α-helices) imbedded in the keratin amorphous matrix (grey islands). The chemical changes induced by the oxidative **(a)** and reductive & oxidative **(b)** treatments (see text). RSH is the abbreviation for thioglycolic acid.

The reductive-oxidative modification occurs in two steps. Firstly the S-S bonds are broken by the action of the reductive reagent, thioglycolic acid (TGA) and then are reformed by the oxidative reagent (see Fig. 2.31b). During this sequence of reactions not all the bonds are broken and not all the broken bonds reform; besides, not all the reformations occur at the same places. In other words we expect to reform the material but with a more hindered molecular mobility of the interface and matrix as shown in Fig. 2.21 obtained from deconvolution of ^{1}H NMR spectra. The crystalline part increase slightly compared to hard α-keratin (Fig. 2.20a and c) but a reorganization process takes place that reduce the rigid domain sizes (Fig. 2.27). Consequently, the DSC peak is recorded at a temperature between those of un-treated and of oxidatively-treated material and has also an intermediary value of the enthalpy (Fig. 2.18).

2.5 Conclusions

Proton and ^{13}C NMR spectroscopy, double-quantum, and ^{1}H spin-diffusion NMR were used to characterize morphology, phase composition, segmental dynamics and domain thicknesses during thermal denaturation of hydrated wool keratin and for hard α-keratin of hair under various chemical treatments and in a range of temperatures including the temperature of denaturation. For the first time, quantitative information about the heterogeneity of side chain and segmental mobility of the interfacial region are obtained by ^{1}H spin-diffusion NMR. The side chain motions play an important role in defining the material properties of keratin. It may well be their degrees of freedom which can dissipate stress during the mechanical deformation of keratin fibers.

These reported NMR results support the thermal denaturation pathway described above according to which along with the collapse of the scaffolds, the α-helices change from a relatively compact ordered structure to a more flexible, disorganized, open polypeptide chain. This is shown by an increase of the mobile phase at the expense of the rigid- and interfacial phases. At higher temperature, the protein molecules unfold and the internal hydrophobic regions expose to the outside of the molecules. The hydrophobic groups tend to cluster in deuterated water, leading to associations of molecules and a resurgence of the amount of rigid phase. The interphase amount remains, however, unchanged, as no other re-organisation occurs.

3 Properties of Sulfonated Poly(Ether Ether Ketone) Silica Proton Exchange Membranes by ^{1}H NMR

3.1 Introduction

Proton exchange membranes fuel cells (PEMFC) are a promising new energy source with a wide range of applications varying from industrial applications like microelectronics, vehicles and aerospace applications to residential purposes [Car01, Jon85, Yue07]. Research and development of new PEMFCs has developed into a highly recognized topic over the past decade [Kre01, Hic05]. Extensive efforts were spent to develop alternative hydrocarbon-based polymer electrolyte membranes to overcome the currently widely used perfluorosulfonic acid Nafion membrane [Hic04]. An alternative for the Nafion membranes are sulfonated polyether ether ketones (SPEEK) (Fig. 3.1) membranes due to their good conductivity, thermal stability and mechanical properties [Zai00, Kob98, Kre01].
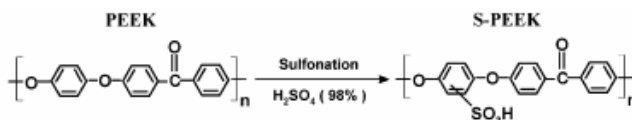
Fig. 3.1 Schematic chemical formula of SPEEK.

Since the state of the water confined in the polymer matrix and the proton exchange between different water states has direct consequences on the transport properties of the protons within the membrane, its characterization is an essential part when designing smart PEMs [Pad03]. Besides bulk (or free) water, molecules mainly involved in the diffusion process, the water which is tightly or loosely bound to the sulfonic acid groups i.e., at the first level of hydration or in the larger salvation shell, take part in the transport process by dissociation and proton exchange. Many NMR techniques including 1D and 2D ^{1}H NMR spectroscopy [Lap99, Gow02, Li08, and references therein], relaxometry [Ye07, Kim03, Per06] and diffusiometry [Zaw91] give evidence of different states of water and provide a way to correlate the role of the different water states with other properties relevant to fuel cells applications such as methanol permeability and electro-osmotic drag.

Proton full linewidths at half-height ($\Delta v_{1/2}$) for SPEEK for different degrees of sulfonation and water uptake as a function of temperature were recently reported [Ye06]. Assuming an Arrhenius temperature dependence for $\Delta v_{1/2}$, the energy of activation for proton exchange was estimated. In the investigated temperature range of 300-360 K the water exchange process was characterized by a unique energy of activation [Ye06]. The same approach was reported for Nafion and Nafion/SiO$_2$ composites [Ye07] using the temperature dependence of the self-diffusion coefficients and spectral linewidth. We should note that based on first principles the proton exchange of the acidic protons in the hydrogen-bonded network is described by the empiric Arrhenius law only in a crude approximation.

High-resolution solid-state ^{1}H NMR under fast magic angle spinning (MAS) was used to study proton exchange and conductivity in ethylene oxide tethered imidazole heterocycles [Gow02]. The effective transverse relaxation time measured from the linewidth of the N-H resonance reflects the proton exchange in the fast limit. It is claimed that the Arrhenius relation describes the proton exchange process in the investigated temperature range.

The aim of this study is to characterize quantitatively the proton exchange process and the changes in the state of water in fully hydrated SPEEK/SiO$_2$ composite PEMs [Col06, Zhu06] by ^{1}H solid-state NMR as a function the polyethoxysiloxane (PEOS) content. The temperature dependence of the full linewidth at half intensity from the ^{1}H NMR spectra under magic angle sample spinning (MAS) was used to measure the enthalpy of activation of exchange processes based on an Eyring function. The normalized enthalpy of activation was measured from the temperature dependence of the isotropic chemical shift. The dependence of these thermodynamic quantities on the PEOS content is also reported. Proton 1D exchange spectroscopy by sideband alteration (ODESSA) [Tek00] was used to measure the effective exchange rate between bound and free water and the average longitudinal relaxation time (T_1). Moreover, the molecular motions of bound and free water and the population of each water state were investigated by ^{1}H transverse relaxation NMR for different contents of silica oxide particles.

3.2 Experimental

3.2.1 Membrane preparation

Polyetherketone was obtained according to [Zhu06]. Polyethoxysiloxane was prepared as described before with an average molecular weight of $\overline{M}_n$ =1100 [Zhu06]. Poly(ether ether ketone) (PEEK) was sulfonated up to 64% degree of sulfonation. The polymer was dried in an oven at 105° C. The hybrid SPEEK-SiO$_2$ membranes were prepared by adding the respective amount of PEOS, previously dissolved in methanol, into a solution (0.18 g/mL) of SPEEK in N,N'-dimethylaacetamide (DMAc), stirring the mixture at room temperature for 2 h, casting it onto a glass plate, heating it in the oven at 55° C for 5 h followed by heating at 120° C overnight. According to the chemical composition and density, 2 wt.% PEOS added to the membrane preparation corresponds to a fraction of 1 wt.% SiO$_2$ in the final membrane. The obtained membranes were immersed in demineralised water at 60° C for one night and they were kept in water at room temperature until they were used for the measurements. The detailed characterization of all samples is summarized in Tab. 3.1.

Table 3.1 List of hybrid SPEEK-silica membranes and their preparation [Col09].

Sample name[a]	PEOS[b]		PEOS diluent[c]		Expected silica content [wt.%][d]
	[g]	[wt.%]	[mL]	type	
SP-PE.10	0.04	10	0.5	MeOH	5.4
SP-PE.20	0.09	20	0.5	MeOH	11.4
SP-PE.30	0.15	30	0.5	MeOH	17.1
SP-PE.40	0.23	40	0.5	MeOH	24.7
SP-PE.50	0.35	50	0.5	MeOH	33.3

[a] The numbers refer to the weight percentage of PEOS. [b] Amount of PEOS: given as grams and as percentage the total weight of the two polymers. [c] Solvent used to dissolve PEOS: amount (mL) and type. [d] The expected silica content is calculated assuming full conversion of PEOS into silica. Knowing the SiO$_2$ content in the PEOS synthesized for this study (48%), the theoretical weight percentage of silica in the final membrane is calculated as:
(grams of PEOS x 0.48)/[(grams of SPEEK) + (grams of PEOS x 0.48)].

3.2.2 Proton NMR measurements

Proton NMR MAS spectra were measured on Bruker DMX-300 and DSX-500 spectrometers. The chemical shifts of the NMR spectra are referenced to TMS. The spectra were collected in the temperature range 295-370 K with a temperature stability of ±0.1° C.

The duration of a 90° radio-frequency pulse was about 3.5 μs (at 300 MHz) and 3.5 μs (at 500 MHz). The dwell time was 1 μs (at 300 MHz) and 2.5 μs (at 500 MHz), and the recycle delay was 500 to 700 ms for all measurements. Transverse ^{1}H relaxation times (T_2) were measured with the multi-echo CPMG method with an inter-echo time of 100 μs. The measurements were made under magic-angle sample spinning (MAS) with the rotor frequency of ν_R = 5 kHz. The ^{1}H ODESSA [Tek00] pulse sequence with rotor-synchronized mixing time (Fig. 3.2) was employed on the DSX-500 spectrometer. For ODESSA measurements a rotor frequency of ν_R = 2 kHz was used.
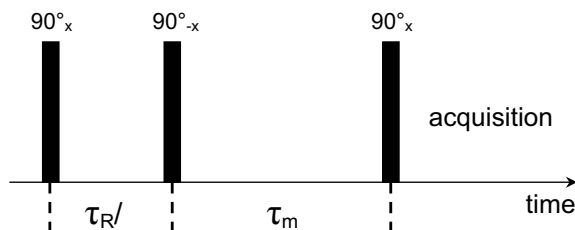
Fig. 3.2 Pulse sequence for ODESSA NMR [Tek00]. The mixing time is rotor synchronized, i.e., $\tau_m = M\tau_R$, where (M = 1,2,3,…).

3.3 Results and discussion

3.3.1 Enthalpy of activation for water chemical exchange by the Eyring function

Proton NMR spectra of fully hydrated SPEEK membranes were recorded under MAS at a rotor frequency ν_R = 5 kHz and a temperature T = 295 K (Fig. 3.3). The intense line corresponds to a coalescence of the NMR peaks from the protons attached to the sulfonic groups (-SO$_3$H) that includes also bound water molecules and highly mobile molecules of free water. Weak spinning sidebands are evident and are related mainly to the residual dipolar interactions and chemical shift anisotropy of bound water. This was proved by an exchange NMR experiment using one-dimensional exchange spectroscopy by sideband alteration [Tek00]. We show here that the intensity of the spinning sidebands changes with the mixing (exchange) time. Hence, should be related to the bound water. Moreover, an NMR experiment using a dipolar filter that leads to a ^{1}H MAS NMR spectrum without the broad component corresponding to the protons in the backbone of SPEEK. Nevertheless, the spinning sidebands are still present showing that they originate from the bound water.
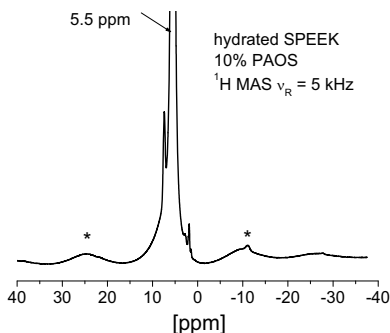
Fig. 3.3 Proton spectrum of fully hydrated SPEEK membrane with 10 wt.% PEOS under MAS at 5 kHz. The spinning sidebands are marked with stars.

The measurements made at different rotor frequencies in the range 0.5-5 kHz show that the chemical shift and the linewidth at the half-height are independent of ν_R (Fig. 3.4). Hence the proton exchange processes are not affected by the sample rotation in the investigated rotor frequency range. The spinning side pattern is positioned on top of a broad NMR spectrum related to the protons of PEEK polymer with restricted molecular motions.
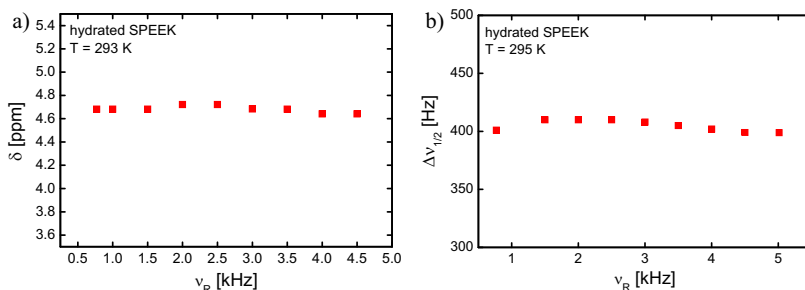
Fig. 3.4 The chemical shift **(a)** and the full line width at half intensity **(b)** of ^{1}H NMR spectra under MAS for the hydrated SPEEK membrane as a function of rotor frequency. The measurements were made at room temperature.

We shall consider in the following that the chemical exchange of protons between different water pools can be described by an effective exchange rate k_{eff}. The dependence of k_{eff} on temperature is described by the Eyring function [Bai03, and references therein]. In the fast exchange limit the relationship $\Delta \nu_{1/2} \propto k_{eff}^{-1}$ is valid where $\Delta \nu_{1/2}$ is the full linewidth at the half height [Bai03]. One of the major differences between the Eyring and

Arrhenius functions is the fact that the prefactor is temperature dependent in the Eyring function.

The temperature dependence of $\Delta\nu_{1/2}$ is given by the Eyring function as

$$\Delta\nu_{1/2} \propto \left[\frac{k_B T}{h} \exp\left(\frac{\Delta S^+}{R} - \frac{\Delta H^+}{RT} \right) \right]^{-1}, \qquad (3.1)$$

where k_B is the Boltzman's constant, T is the temperature, h is Planck's constant, R is the ideal gas constant, and $\Delta G^+ = \Delta H^+ - T\Delta S^+$ is the free energy of activation. The dependence of $\ln(\Delta\nu_{1/2}T)$ as a function of $1/T$ is a straight line with the slope related to the enthalpy of activation ΔH^+. Such a dependence is shown in Fig. 3.5 for fully hydrated SPEEK and was measured for all SPEEK/SiO$_2$ samples. Two different proton exchange processes are detected for all samples. The first process takes place at low temperatures with a small value of ΔH^+ (hereafter ΔH_2^+) and corresponds to the chemical exchange between strongly bound and free water at higher temperatures.
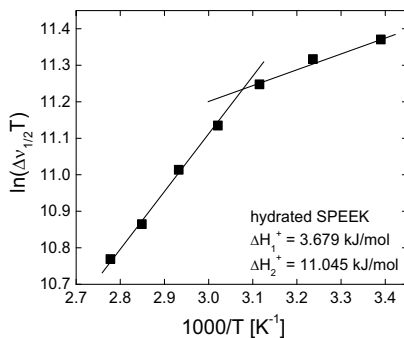
Fig. 3.5 The temperature dependence of $\ln(\Delta\nu_{1/2}T)$ measured by the full linewidth at half intensity from ^{1}H MAS spectrum at $\nu_R = 5$ kHz for hydrated SPEEK using the Eyring functional dependence.

The dependence of the enthalpies of activation for fully hydrated SPEEK/SiO2 as a function of the amount of PEOS is shown in Fig. 3.6. The quantity ΔH_2^+ shows a minimum for the sample with about 20 wt.% PEOS. Therefore, less thermal energy is needed in order to activate the exchange between strongly bound and free or weakly bound water. For larger values of the PEOS concentration, the enthalpy of activation for exchange between weakly bound and free water is not changing essentially with increasing amount of PEOS.
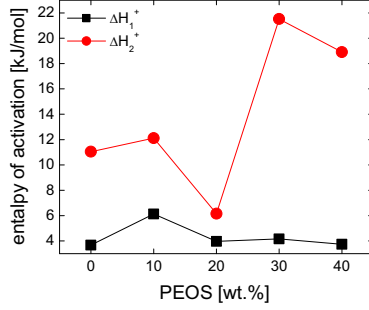
Fig. 3.6 Enthalpies of activation for water exchange in hydrated SPEEK with different PEOS contents. The errors are of the order of 5%.

3.3.2 Normalized enthalpy of activation for proton chemical exchange by isotropic chemical shift

For obtaining information about the free energy of activation the NMR method using the coalescence temperature was applied. The isotropic chemical shift δ of the coalescence peak is given by [Mar80]

$$\delta(T) = p_1(T)\delta_1(T) + p_2(T)\delta_2(T),$$ (3.2)

where δ_1 and δ_2 are the isotropic chemical shifts of the different states of water. The ratio of probabilities of the site occupations p_1 and p_2 is described by the relationship [Sha70]

$$\frac{p_1}{p_2} = \exp\left\{-\frac{\Delta G^+}{RT}\right\},$$ (3.3)

where the quantity ΔG^+ is the free activation energy difference between the two species participating in the chemical exchange. From the normalization condition $p_1+p_2=1$, and Eq. (3.3) one can derive

$$\delta(T) = \frac{\exp\left\{-\Delta G^+ / RT\right\}\delta_1(T) + \delta_2(T)}{1 + \exp\left\{-\Delta G^+ / RT\right\}}.$$ (3.4)

From the above equation in the limit of $\Delta G^+ << RT$ we can write

$$\delta(T) \approx \frac{\delta_1(T) + \delta_2(T)}{2} + \frac{\delta_1(T) - \delta_2(T)}{4}\frac{\Delta G^+}{RT}.$$ (3.5)

If the temperature dependence of the individual chemical shift parameters can be neglected in the investigated temperature range, i.e., $\delta_i(T) \approx \overline{\delta}_i$, $(i=1, 2)$ we can finally write,

$$\delta(T) \approx \frac{\overline{\delta}_1 + \overline{\delta}_2}{2} - \frac{\overline{\delta}_1 - \overline{\delta}_2}{4}\frac{\Delta S^+}{R} + \frac{\overline{\delta}_1 - \overline{\delta}_2}{4}\frac{\Delta H^+}{RT}.$$ (3.6)

The temperature dependence of the isotropic chemical shift of the exchange peak is shown in Fig. 3.7. The experimental data of Fig. 3.7 are in agreement with Eq. (3.6). This clearly shows that the temperature dependence of the water exchange process dominates that of the chemical shifts δ_1 and δ_2. The individual isotropic chemical shifts $\overline{\delta}_1$ and $\overline{\delta}_2$ are difficult to measure in the very slow exchange regime due to the dipolar line broadening effects. The temperature change of the magnetic susceptibility could be responsible for the variation of the measured chemical shift δ. The susceptibility correction for the measured chemical shift follows the relationship $\delta = \delta_0 - \left(\dfrac{4\pi}{3} - \overline{\alpha} \right) \kappa$, where δ_0 is the uncorrected chemical shift, $\overline{\alpha}$ is the mean shape factor of the sample, and κ is the volume magnetic susceptibility [Hof03]. The last quantity for water depends on the number of hydrogen bonds and in the first approximation changes linearly with the temperature [Cin68]. If this effect is comparable to that of the Boltzmann factor the temperature dependence of $\delta(T)$ in Eq. (3.6) will not follow the linear dependence shown in Fig. 3.7.
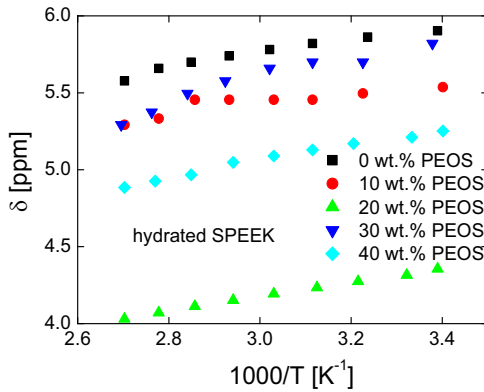
Fig. 3.7 The temperature dependence of the coalesced peak position (δ) for fully hydrated SPEEK for different PEOS concentrations from the ^{1}H MAS spectrum at $\nu_R = 5$ kHz.

The data of Fig. 3.7 reveal that the measurements of the temperature dependence of the isotropic chemical shift of the collapsed resonance do not probe separately the proton exchange between different water pools like the measurements of linewidth (Fig. 3.5). This can be explained by the fact that the former experiment is related to the statistical equilibrium of water populations and the last one describes the kinetics of proton exchange in a cooperative hydrogen bonded network.

From Eq. (2.6) we can evaluate the ratio $\Delta H^+(PEOS)/\Delta H^+(0)$, where $\Delta H^+(0)$ is the enthalpy of activation for SPEEK membrane without silica. The dependence of $\Delta H^+(PEOS)/\Delta H^+(0)$ on the amount of PEOS is shown in Fig. 3.8. The ratio of the enthalpies of activation shows a minimum for the low content of PEOS and increases for larger values of PEOS content similar to that of the enthalpy of activation (Fig. 3.6).
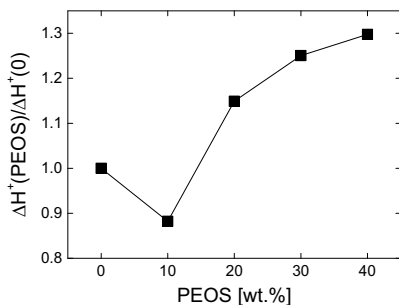
Fig. 3.8 Normalized enthalpy of activation for water exchange in hydrated SPEEK versus content of PEOS. The errors are of the order of 5%.

3.3.3 Water exchange rate and longitudinal relaxation by ODESSA NMR

Proton MAS-NMR spectra of fully hydrated SPEEK PEM were recorded at a rotor frequency $\nu_R = 2$ kHz where all samples show spinning sideband (ssb) (Fig. 3.9). These sideband patterns are observed on top of a broad line from the protons of the PEEK backbone with restricted molecular motions. This broad spectral component is suppressed by the ODESSA pulse sequence. The intense centerband corresponds to a coalescence of the NMR peaks from the protons attached to the sulfonic acid groups (-SO$_3$H) that include also bound water molecules and highly mobile molecules of free water. Weak spinning sidebands are evident and are related mainly to the residual dipolar interactions and partially to the small chemical shift anisotropy of the bound water. The measurements made at different rotor frequencies in the range 0.5 kHz – 5 kHz show that the linewidth at the half height of centerband is independent of ν_R. Hence, the proton exchange process is not affected by the sample rotation in the investigated range of rotor frequencies.
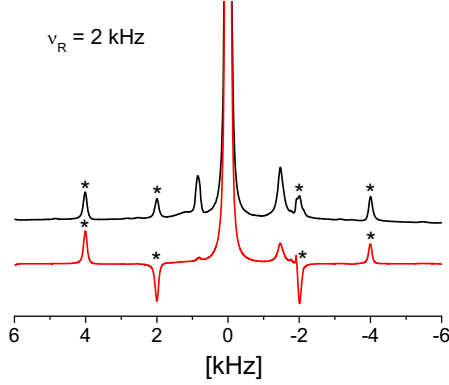
Fig. 3.9 Proton spectrum of a fully hydrated SPEEK membrane without PEOS under MAS at 2 kHz measured at 500 MHz. The spinning-sidebands with positive intensities are shown in the top spectrum. The bottom spectrum with alternating sidebands corresponds to that measured using the ODEESA method.

In the following it is assumed, that the chemical exchange of protons between different water pools can be described by an effective exchange rate k and an average longitudinal relaxation time T_1. In the approximation of the exchangeable protons of congruent sites [Rei00] the intensity of the ssb of order N is given by:

$$I_N(\tau_m) = \left(A_N + B_N e^{-2k\tau_m}\right) e^{-\tau_m/T_1}, \tag{3.7}$$

where

$$A_N = \frac{1}{2}\left\langle\left(I_N^{11} + I_N^{12}\right)\right\rangle$$
$$A_N = \frac{1}{2}\left\langle\left(I_N^{11} - I_N^{12}\right)\right\rangle \tag{3.8}$$

and $I_N^{ij} = I_N^{ji}$. The symbol $\langle\langle...\rangle\rangle$ denotes the powder average over the Euler angles for a particular interproton vector. The quantities I_N^{ij} can be calculated from so-called f functions [Rei00] that are orientation dependent. For the normalized intensity of the ssb of order N one eventually obtains

$$\frac{I_N(\tau_m)}{I_N(0)} = \frac{A_N}{A_N + B_N} e^{-\tau_m/T_1} + \frac{B_N}{A_N + B_N} e^{-(2k+1/T_1)\tau_m}. \tag{3.9}$$

The validity of the above equation is supported by the fact that the magnetization buildup in the saturation recovery T_1 measurements can be fitted by a mono-exponential function for the investigated series of SPEEK/SiO$_2$ samples.

An example of the mixing time evolution of the ssb patterns of hydrated SPEEK without PEOS for the ratio $I_N(\tau_m)/I_N(0)$ ($N = 1, 2$) is shown in Fig. 3.10a together with a fit of the experimental data using Eq. (3.9). The dependence of the ODESSA build-up and decay curves as a function of the PEOS content is shown in Figs. 3.10b and 3.10c.
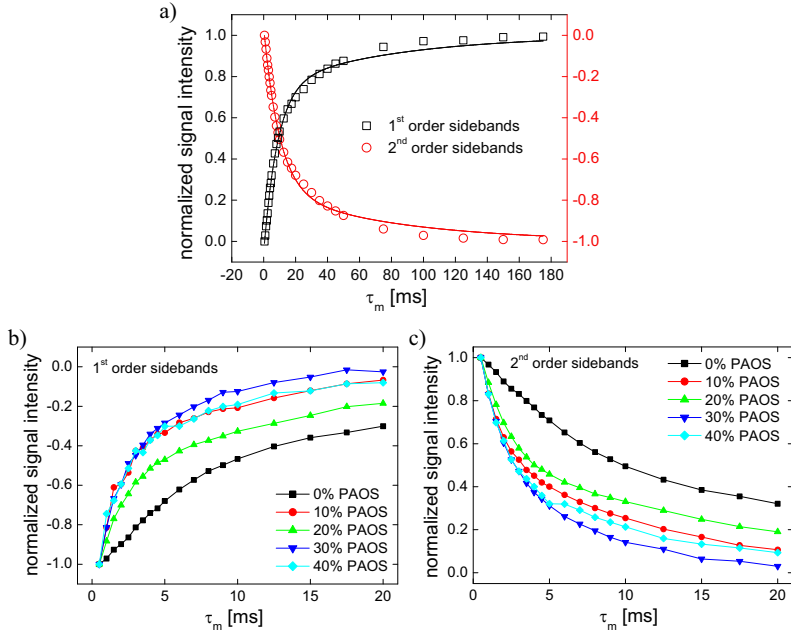
Fig. 3.10 (a) Intensities of the first and second order ssb for fully hydrated SPEEK membrane without PEOS as a function of τ_m. The solid lines are the fits with Eq. (2.9). **(b)** The ODESSA buildup curves for the $N = 1$ spinning sidebands of SPEEK with different PEOS contents. **(c)** ODESSA decay curves for the $N = 2$ spinning sidebands of fully hydrated SPEEK with different PEOS content. The data points are connected by lines to guide the reader. All measurements were made at room temperature.

Figure 3.11 shows the dependence of T_1 and the effective exchange rate k of fully hydrated SPEEK membranes at room temperature as a function of the PEOS content obtained from the data of Fig. 3.10 and Eq. (3.9). The data of Fig. 3.11 reveal that for the investigated range of PEOS content the condition $T_1 > 1/k$ is fulfilled, i.e. the water exchange times are *fast* on the time scale of the longitudinal relaxation times. The presence of PEOS will reduce substantially the T_1 of water due to the increased amount of bound water (*vide infra*).
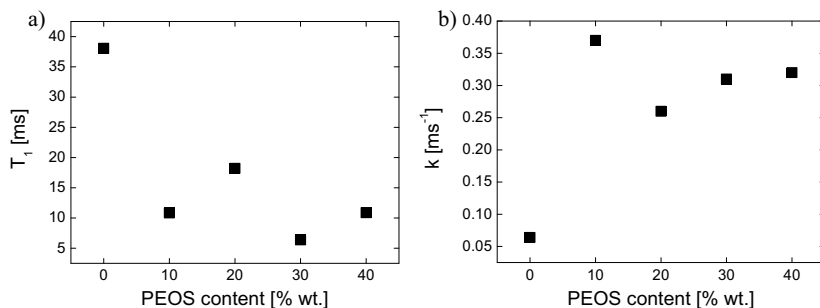
Fig. 3.11 Dependence of T_1 **(a)** and k **(b)** as a function of PEOS content in SPEEK membranes at room temperature.

For the same SPEEK/SiO$_2$ series the enthalpy of activation was reported to have a minimum in the range of 10%-20% wt. PEOS based on an analysis of the temperature dependence of the width of the centerband [Bai08]. Therefore, less thermal energy is needed in order to activate the exchange between strongly bound and free or weakly bound water. This is in agreement with the observation of the maximum value of the effective exchange rate k at 10% wt. PEOS (Fig. 3.11b).

3.3.4 State of water by ^{1}H transverse relaxation NMR

Decays of CPMG trains from fully hydrated SPEEK/SiO$_2$ membranes were recorded at room temperature on a DMX-300 spectrometer under MAS with a rotor frequency of $\nu_R = 5$ kHz. Two distinct transverse relaxation processes are evidenced. The one with short relaxation time T_{2s} corresponds to the water bound to the acidic sites, and other with a longer relaxation time T_{2l} relates to the free water. The proton exchange is *slow* on the time scale of transverse relaxation time, i.e. $T_2 < 1/k$. The dependence of these relaxation times on the PEOS content is shown in Fig. 3.12a. The mobility of the free water has a maximum for 10% wt. PEOS but increases monotonically for bound water. In the complete range of investigated PEOS content, the increased mobility of the free water leads to values of T_{2l} longer than those of the samples without PEOS.
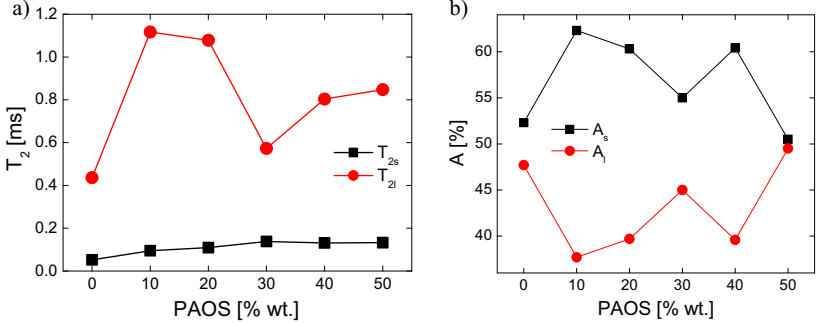
Fig. 3.12 Dependences of T_{2s} and T_{2l} **(a)** and of the relative amounts of bound (A_s) and free water (A_l) **(b)** on the PEOS content in fully hydrated SPEEK. All the measurements were done at room temperature.

In proton exchange membranes the bound water is connected to the sulfonated sites by hydrogen bonds. If we assume bulk mediated surface diffusion in the strong-absorption limit, the diffusion process can be described by Lévy statistics and a Cauchy propagator [Val97, and references therein]. For a planar surface the water displacement r is governed by the propagator of the form

$$P(r,t) = \frac{1}{2\pi} \frac{ct}{\left[(ct)^2 + r^2 \right]^{3/2}} , \qquad (3.10)$$

that is valid for surface displacements short compared to the rms value in the bulk. For the dipolar interaction, which is the main relaxation mechanism, the relevant correlation functions refer to the spherical harmonics of degree two and order m. In this case, the NMR correlation function obtained with the Cauchy propagator Eq. (3.10) for infinite planar surfaces [Val97] becomes

$$G_{\mathrm{m}}(\tau) = 1 - \frac{1}{\sqrt{1 + t_{\mathrm{h}}/|\tau|}} , \qquad (3.11)$$

where the water retention time is $t_{\mathrm{h}} = h^2 / D_0$. The adsoption depth is denoted by h and the bulk diffusion coefficient of water is D_0.

The transverse relaxation rate $1/T_2$ is dominated by the spectral density function $J^{(0)}(0) \approx 2 \int_0^{\tau_c} G_0(\tau) d\tau$, i.e., $1/T_2 \propto J^{(0)}(0)$. Therefore, from Eq. (3.11) we can write

$$\frac{1}{T_{2s}} \propto 2\tau_c - \sqrt{\tau_c(\tau_c + t_{\mathrm{h}})} + t_{\mathrm{h}} \ln\left\{ \sqrt{\frac{\tau_c}{t_{\mathrm{h}}} + 1} + \sqrt{\frac{\tau_c}{t_{\mathrm{h}}}} \right\} . \qquad (3.12)$$

Hence, the transverse relaxation rate $1/T_{2s}$ is related to the correlation time τ_c which describes the reorientation of the proton internuclear vector in the "Lévy dust" and the water retention time t_h. From Fig. 3.12a it is evident that both these quantities essentially do not change with the amount of PEOS. Nevertheless, the amount of bound water is changing in the presence of silica particles (*vide infra*). For long transverse relaxation times we have $T_{21} \propto \tau_c^{-1}$, and therefore, the reorientations and translations of the free water molecules become faster in the hybrid SPEEK/SiO$_2$ (Fig. 3.12a) due to faster exchange with bound water (Fig. 3.11b) in the presence of silanol groups.

The relative amounts of bound and free water can be evaluated from the amplitudes A_s and A_l of the two exponential functions used to fit the transverse magnetization decay in CPMG experiments. Their dependence on the PEOS content is shown in Fig. 3.12b. The highest amount of bound water in the fully hydrated SPEEK at room temperature is detected for 10% wt. in PEOS.

3.4 Conclusions

The proton exchange processes are investigated in hydrated SPEEK/SiO$_2$ PEM series. As the molecular actors in these processes are protons as quantum particles the quantum-mechanical approach is needed. Therefore, the Eyring function is used for the evaluation of the enthalpy of activation describing proton exchange between different water pools. The measurements of the isotropic chemical shift of the NMR MAS spectrum as a function of temperature provide information about the normalized enthalpy of activation for exchange processes. These thermodynamic quantities reveal that the water exchange processes in hydrated SPEEK-silica membranes are more efficient when low concentrations of PEOS are used for the sample preparation. This will increase the probability of hydrogen bond breaking and *inter alia* will lead to better performances of PEMs.

The state of water was investigated in series of fully hydrated SPEEK/SiO$_2$ PEM samples by ^{1}H ODESSA and transverse relaxation NMR. The ODESSA method allows us to quantify the bound/free water exchange rate. It shows a maximum near 10% wt. PEOS. The dynamics of bound water were analyzed by ^{1}H transverse relaxation NMR in terms of Lévy statistics. In contrast to the free water it was shown that the reorientation correlation time and retention time of bound water at room temperature is not very sensitive to the silica particle content. These results reveal that the exchange rate between bound and free water as well as the amount of bound water in hydrated SPEEK/SiO$_2$ PEM increase when

low concentrations of PEOS are used for sample preparation. Therefore, the presence of silica particles with concentration of 5%-10% wt. is expected to enhance the electrical conductivity of PEM.

4 On-line Monitoring of Free Radical Polymerizations by Hyperpolarized ^{129}Xe NMR

4.1 Introduction

In the past two decades ^{129}Xe NMR has developed into a widely used tool for material investigations due to its good spatial and temporal resolution and to the sensitivity of Xe to its chemical environment resulting from its highly polarizable electron cloud, leading thus to a wide range of chemical shifts, and the possibility of hyperpolarization by spin-exchange optical pumping (section 4.2.1) [Hap72, Kni88, Wal97, App98].

Hyperpolarized Xe is met in worldwide applications ranging from fundamental science research to material science and medical applications. Thus, hyperpolarized ^{129}Xe was applied in the field of fundamental physics, where ^{129}Xe/^{3}He spin exchange pumped masers [Sto96, Bea98] were used for the investigation of charge-parity violation [Bea00] and for atomic electric dipole moment measurements [Ros01]. Hyperpolarized ^{129}Xe is a useful tool in surface physics for probing small surfaces [Raf91, But94, Bru98] and single crystals [Jän97, Jän98, Sta02]. In material science, hyperpolarized Xe was successfully applied for the investigation of microporous materials [Ito82, Chm91, Raf91, Raf94, Rat98, Jam02, Ter02, Nos03, Sea03, Mou04, Stu04]. In biological sciences, hyperpolarized Xe NMR is used as a biosensor in protein studies [Til82, Alb95, Rub00a, Rub00b, Loc01], having a more a specific application in studying the red blood cells and the degree of oxygenation of human blood [Bif96, Wol00a, Wol00b]. Hyperpolarized ^{129}Xe is also used in NMR and MRI studies in medical sciences, where ^{129}Xe can be applied as an imaging agent [Alb94, Tse99, Mou00, Mai03, Han04, Wan04].

Understanding how polymerization reactions work is very important in polymer engineering because it can provide information related to the physical and chemical changes of the polymer during the polymerization process. Therefore, a real-time monitoring of the of the reaction could be a useful tool in understanding the properties of the polymer as its molecular weight starts increasing during the polymerization. The aim of

this work is to exploit the capability of Xe NMR for performing time-resolved measurements combined with the good sensitivity of Xe to its chemical environment for the monitoring of free radical polymerizations in real-time. The measurements were done under continuous hyperpolarized Xe flow [App01]. The hyperpolarized gas dissolves in the reaction bulk and makes time resolved Xe NMR spectroscopy viable.

The polymerizations of methyl methacrylate (MMA), methyl acrylate (MA), and the copolymerization of methyl methacrylate and methyl acrylate were performed as free radical polymerizations in the presence of an initiator – azobisisobutylonitrile (AIBN) and a solvent – butyl acetate. The changing in chemical shift and linewidth of xenon inside the polymers was analyzed as a function of the reaction time, showing the effect of increasing the molecular weight of a polymer on the xenon signal.

4.2 Theory

4.2.1 Hyperpolarization by spin-exchange optical pumping

Spin-exchange optical pumping (SEOP) refers to the mechanism of transferring the angular momentum from circular polarized light to the nuclear spins in several steps [Hap72, Wal97, App98] (Fig. 4.1). The first step refers to the transfer of spin order from photons from circular polarized light to the electron spins of Rb atoms. This procedure is called optical pumping, and it was discovered by Kastler in 1950 [Kas50], for which he was awarded the Nobel Prize in Physics in 1966. The second step in SEOP was discovered by Bouchiat et al. in 1961 [Bou60, Her65, Bou69, Bou72, Gro78, Vol80, Bha83, Hap84] and it consists in transferring the polarization from the electron spins of an alkali-metal atoms to the nuclear spins of a noble gas, in our case ^{129}Xe, by Rb-Xe binary collisions. The combination of the first two steps defines the spin-exchange optical pumping. Further on it has been discovered that by dipole-dipole interactions, the nuclear polarization can be transferred from the Xe atoms to the protons of liquid toluene via Spin Polarization Induced Nuclear Overhauser Effect (SPINOE) [Nav96, Cav96, Son97, Son00, App01]. This results in a high proton polarization which can later be transferred to other nuclei via cross-polarization (CP) [Lon93, Gae95, Pie98].
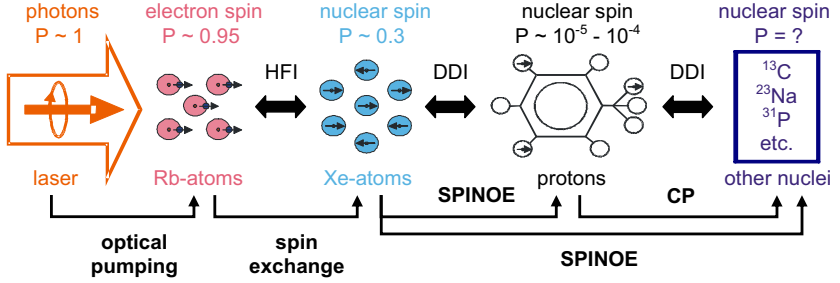
Fig. 4.1 Principle of polarization transfer via SEOP: polarization is transferred from photons to the electron spins of Rb atoms, from the electron spins to the nuclear spins of Xe atoms by hyperfine interactions and further on to protons and other nuclei by dipole-dipole interactions via SPINOE and CP. The magnitudes of spin polarization P for each step are indicated at the top of the figure [App04].

4.2.2 Chemical shift of ^{129}Xe

When a molecule is placed in an external magnetic field B_0 its atoms experience a variation in the local magnetic field compared to the applied external magnetic field. As a result, the precession frequency of a given atomic nucleus is proportional to the local value of the magnetic field. Therefore, the Larmor frequency depends on the location of the nucleus in the molecule and on the details of the electronic structure [Lev01]. This effect is called chemical shift (δ) and it is described by the following equation:

$$\delta = \frac{B_{\text{loc}} - B_{\text{loc}}^{\text{ref}}}{B_0} = \sigma^{\text{ref}} - \sigma, \tag{4.1}$$

where B_{loc} is the local field of the molecule or atom of interest and $B_{\text{loc}}^{\text{ref}}$ is the local field of a reference molecule or atom, and σ, σ_{ref} is the magnetic shielding of the observed and the reference nucleus [Blü00, App04].

Following Buckingham, Streever, and Jameson [Buc56, Str61, Jam70, Jam73, Jam92] the nuclear shielding of Xe gas $\sigma(T,[Xe_{\text{gas}}])$ can be described by a virial expansion

$$\sigma\left(T,\left[Xe_{\text{gas}}\right]\right) = \sigma_0\left(T\right) + \sigma_1\left(T\right)\left[Xe_{\text{gas}}\right] + \sigma_2\left(T\right)\left[Xe_{\text{gas}}\right]^2 + \ldots, \tag{4.2}$$

where $\sigma_1(T)$ and $\sigma_2(T)$ are called the second and third virial coefficients of shielding, respectively, which depend on the temperature T and the Xe gas density $[Xe_{\text{gas}}]$. For Xe gas the first virial coefficient $\sigma_0(T)$ is constant and is set by definition to zero [App04]. Thus, Eq. (4.2) is reduced to $\sigma\left(T,\left[Xe_{\text{gas}}\right]\right) = \sigma_1\left(T\right)\left[Xe_{\text{gas}}\right]$. Buckingham showed that the second virial coefficient can be expressed as

$$\sigma_1(T) = \int_0^\infty 4\pi r_a^2 \cdot \left[\sigma(r_a) - \sigma(\infty)\right] \cdot \exp\left(-\frac{V_{\text{pot}}(r_a)}{kT}\right) dr_a, \tag{4.3}$$

where $\sigma(r_a)$ is the intermolecular shielding function, which depends on the intermolecular separation r_a, and $\sigma(\infty)$ is the shielding of the free Xe atom for $r_a=\infty$. $V_{\text{pot}}(r_a)$ is defined as the intermolecular potential function with a minimum at $r_a=r_0$.

According to Jameson *et al.* the shielding function $\sigma(r_a)$-$\sigma(\infty)$ consists of a paramagnetic contribution $\sigma^{\text{par}} \sim -\sigma_0^{\text{par}} / r_a^6$ and a diamagnetic contribution $\sigma^{\text{dia}} \sim \sigma_0^{\text{dia}} / r_a$ [Jam92] resulting in a positive chemical shift due to the fact that for a noble gas the negative paramagnetic contribution to the total shielding is larger than the positive diamagnetic contribution.

Eq. (4.3) can be well approximated by an analytical model where the potential $V_{\text{pot}}(r_a)$ at $r_0<r_a<r_0+d_a$ is replaced by a potential well of width d_a, and has an average activation energy E_A per atomic pair. Thus, Eq. (4.3) is replaced by $\exp\left(-V_{\text{pot}}(r_a)/kT\right) \approx 1-V_{\text{pot}}(r_a)/kT$ under the condition that $\left|V_{\text{pot}}(r_a)\right| \ll kT$, leading to a new expression for the second virial coefficient [App04]:

$$\sigma_1(T) = \alpha_1 + \alpha_2 \cdot \exp\left(-E_A/kT\right) + O\left(1/kT\right), \tag{4.4}$$

where the coefficients α_1 and α_2 are given by

$$\begin{aligned}
\alpha_1 &= -(4/3)\pi\sigma_0^{\text{par}}\left(r_0+d_a\right)^{-3}, \\
\alpha_2 &= -(4/3)\pi\sigma_0^{\text{par}}\left[r_0^{-3}-\left(r_0+d_a\right)^{-3}\right] + 2\pi\sigma_0^{\text{dia}}\left[\left(r_0+d_a\right)^2 - r_0^2\right].
\end{aligned} \tag{4.5}$$

The function $O(1/kT)$ is linear in $V_{\text{pot}}(r_a)/kT$ and is much smaller than α_1 and α_2. Therefore it will be neglected in the following. The coefficient α_1 in (4.4) can be interpreted as the temperature independent chemical shift contribution which originates from long range Xe-Xe or Xe-solvent interactions. The term $\alpha_2 \cdot \exp\left(-E_A/kT\right)$ represents the temperature dependent chemical shift contribution due to short range contact Xe-Xe or Xe-solvent interactions [App04].

4.3 Experimental

4.3.1 Samples

The reactions investigated are the free radical polymerizations of methyl methacrylate (MMA), methyl acrylate (MA), and copolymerization of methyl methacrylate nad methyl

acrylate The polymerizations were initiated by azobisisobutylonitrile (AIBN) and the solvent used for all cases was butyl acetate. For the polymerization of methyl methacrylate, the reaction took place by mixing 1 mL of methyl methacrylate with 1 mL of butyl acetate and the reaction was initiated by 0.016 g AIBN. For polymethyl acrylate, 0.9 mL of methyl acrylate were mixed with 1 mL of butyl acetate and 0.016 g AIBN. The copolymerization of methyl methacrylate and methyl acrylate was initiated by 0.033 g AIBN after mixing 1.06 mL of methyl methacrylate with 0.9 mL of methyl acrylate and 2 mL of butyl acetate. For each experiment approximately 1.5 mL of solution was used to study the polymerizations under continuous hyperpolarized Xe flow in a 20 mm sample tube (Fig. 4.2) constructed at the research center Jülich. All reactions were monitored at a constant temperature of 350 K.

Fig. 4.2 Probe for the hyperpolarized ^{129}Xe NMR measurements. The Xe flow is achieved with the help of an inflow gas tube and an outflow gas tube.

4.3.2 ^{129}Xe NMR measurements and set up

The entire setup for the measurements can be seen in Figure 4.3. It consists of a home-built Rb-Xe hyperpolarizer [App04] which provides the continuous hyperpolarized ^{129}Xe flow, two 30 W lasers which produce the circular polarized light with a wavelength of 795 nm, a high vacuum pump, and a temperature controller for the optical pumping cell. The temperature of the pumping cell was maintained constant at 180° C during the measurements.

For the hyperpolarization, a gas mixture of 98% Helium, 1% Nitrogen, and 1% Xenon was used at a pressure of 5 bar. The flow rate for all measurements was 300 cm^3/min. The hyperpolarized Xe is transported to the sample tube (Fig. 4.2) through a 7 m long perfluoroalcoxy (PFA) pipe. The sample tube is placed inside a 4.7 T magnet operated by a Bruker DSX-200 spectrometer working at a ^{129}Xe resonance frequency of 55.3 MHz. The spectrometer is equipped with a standard Bruker temperature unit which allows

measurements to be done in the temperature range of 150 K to 360 K. The high nuclear spin polarization achieved leads to a good S/N ratio offering the possibility to acquire each spectrum in single shot.
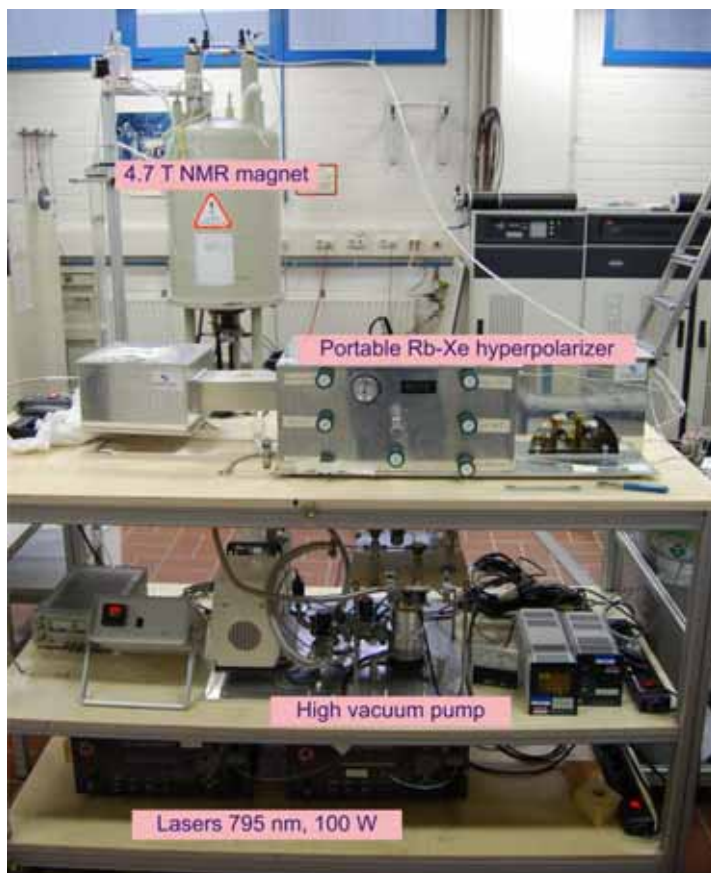
Fig. 4.3 Experimental setup for the [129]Xe measurements: portable Rb-Xe polarizer built at the research center Jülich and located in the Magnetic Research Center RWTH-Aachen University, and the connection to the 4.7 T magnet where the [129]Xe NMR measurements are performed.

A detailed description of the experimental setup can be seen in Figure 4.4. The sample tube containing ca. 0.5 cm^3 of solution is connected to the Xe flow and placed inside liquid N_2 in order to freeze the solution while creating the vacuum in the sample tube. Afterwards the sample tube is removed from the liquid N_2 and inserted into the 4.7 T vertical bore Bruker magnet, and the spectra are acquired while polarized Xe gas is flown with a pressure of 0.05 bar on top of the solution.
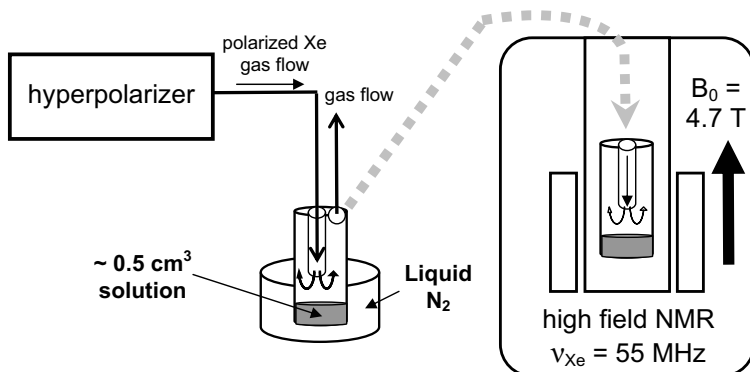
Fig. 4.4 Experimental setup and procedure for the measurement of time-resolved Xe NMR of polymerization reactions under continuous hyperpolarized Xe flow.

4.4 Results and discussion

4.4.1 Polymerization of methyl methacrylate

The free radical polymerization of methyl methacrylate is a chain-growth polymerization initiated by AIBN ($C_8H_{12}N_4$, 2,2'-azobisisobutyronitrile), which upon increasing the temperature above 40° C will split in two radicals with the liberation of a very stable N_2 molecule, as indicated in Fig. 4.5. These radicals will start reacting with the monomers and then the monomers will keep reacting with the active species leading to the formation of polymer chains until the termination of the polymerization occurs. There are two processes that could cause the termination of the free radical polymerization. The first one is termination by combination and results in the simultaneous destruction of two radicals producing a molecule with two initiator fragments. The second termination process is by disproportionation and it occurs when an atom is transferred from one polymer radical to another, and in the end each polymer molecule contains one initiator fragment [Hie84].
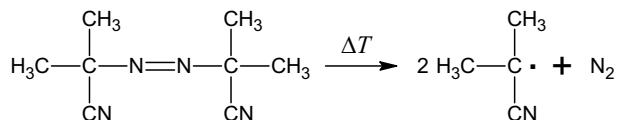
Fig. 4.5 Formation of the free radicals from AIBN (2,2'-Azobisisobutyronitrile) which will lead to the initiation of the polymerization reaction.

The polymerization reaction of MMA was monitored at 350 K in the presence of hyperpolarized [129]Xe, recording [129]Xe NMR spectra at different time intervals during the reaction. In order to study the growth of the PMMA (Fig. 4.6) chains during the polymerization process the evolution of the chemical shift and linewidth of the peak corresponding to the Xe dissolved in the reaction bulk function of the reaction time was recorded.

Fig. 4.6 Repeating unit of a PMMA chain.

Figure 4.7 shows a series of [129]Xe NMR spectra recorded at constant intervals of 30 minutes during the polymerization of MMA using butyl acetate as solvent for the reaction. Considering that the spectra were always referenced to the Xe gas line which was set at 0 ppm, the plots only depict the spectral region corresponding to the Xe dissolved in the reaction bulk.
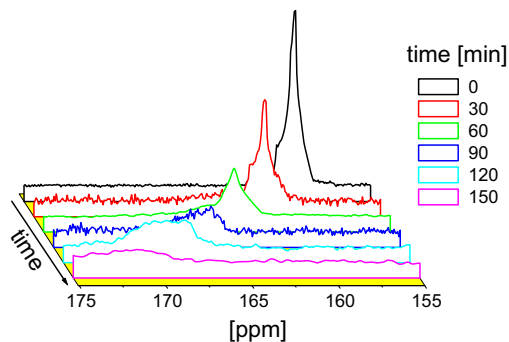
Fig. 4.7 [129]Xe NMR spectra acquired during the polymerization of MMA as function of time. The plot shows the peak corresponding to the Xe dissolved in the reaction bulk which is referenced to the Xe gas line set at 0 ppm.

Taking a closer look at the [129]Xe spectra at different times during the polymerization a clear increase in the chemical shift (Fig. 4.8a) and a broadening of the line corresponding to the hyperpolarized Xe dissolved in the reaction bulk (Fig. 4.8b) with increasing reaction time can be seen. In the beginning of the reaction, the solution is a

liquid with a linewidth of 30 Hz, which after 150 minutes gradually turns into a viscous solution, the final product having a linewidth of 340 Hz. There are a few possible explanations for the line broadening as well as the asymmetric character of the line. One possible explanation is the Xe-H dipole-dipole interaction which becomes stronger as the liquid solution turns into a viscous solution and leads to an increase in linewidth with increasing polymer chains. The inhomogeneous line broadening could be the result of the interaction of the Xe atoms with polymer chains of different size leading to a chemical shift anisotropy. It could also be influenced by an intermediate chemical exchange where the exchange rate is of the order of the difference in chemical shifts of the two sites which leads to an overlapping of the lines resulting in an inhomogeneous line broadening.
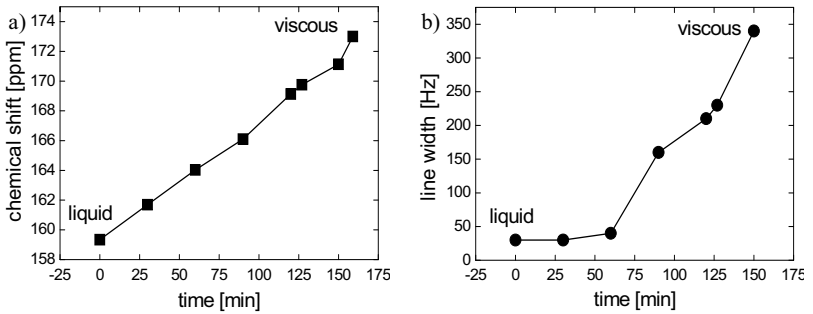
Fig. 4.8 Dependence of the chemical shift **(a)** and linewidth **(b)** on time for the polymerization of methyl methacrylate.

We assume that the measured chemical shift of the Xe dissolved in the polymeric solution δ_{Xe}^{pol} in Figure 4.8a can be described by the sum of four contributions [App04]

$$
\begin{aligned}
\delta_{Xe}^{pol}(T) = &-\sigma_0^{Xe-pol}(T) \cdot [pol](T) - \sigma_0^{Xe-mon}(T) \cdot [mon](T) - \\
&-\sigma_0^{Xe-solv}(T) \cdot [solv](T) - \sigma_1^{Xe-Xe}(T) \cdot [Xe_{sol}](T)
\end{aligned}
\tag{4.6}
$$

where the first term, proportional to the polymer density [pol], on the right side of Eq. (4.6) is the chemical shift contribution due to the Xe-polymer interaction and is equivalent to the first virial expansion coefficient $\sigma_0(T)$ in Eq. (4.2). The second term is the chemical shift contribution due to the Xe-monomer interaction, and the third term is the contribution due to the interaction between the Xe atoms with the solvent molecules. The last term on the right side of Eq. (4.6), which is proportional to the Xe density [Xe_{sol}] in solution, is the chemical shift contribution due to Xe-Xe interaction [App04].

According to Eq. (4.6) the chemical shift of Xe in the polymer solution depends strongly on the local temperature and on the local polymer [pol] and Xe density [Xe_{sol}] in

the Xe-polymer mixture. A very inhomogeneous distribution of the Xe and polymer density in the solution would result in a broad NMR line because the NMR spectrum results as the integral over all spectra of each voxel in the sample volume. This is in agreement with the observations made by Kentgens [Ken91] who upon measuring the linewidth as function of magnetic field strength, suggested that the line broadening of Xe absorbed in polymer samples is due to a distribution of chemical shifts or a small residual shielding anisotropy.

In order to prove that the increase of chemical shift with time (Fig. 4.8a) is indeed due to the polymerization reaction, and is not only the effect of density changes caused by the increasing temperature, the following measurements were done. A new solution of MMA, AIBN, and butyl acetate was prepared and ^{129}Xe NMR spectra were recorded while increasing the temperature to 350 K, then at the constant temperature of 350 K. Afterwards ^{129}Xe spectra were recorded while decreasing the temperature to room temperature and then while increasing it back to 350 K (Fig. 4.9).
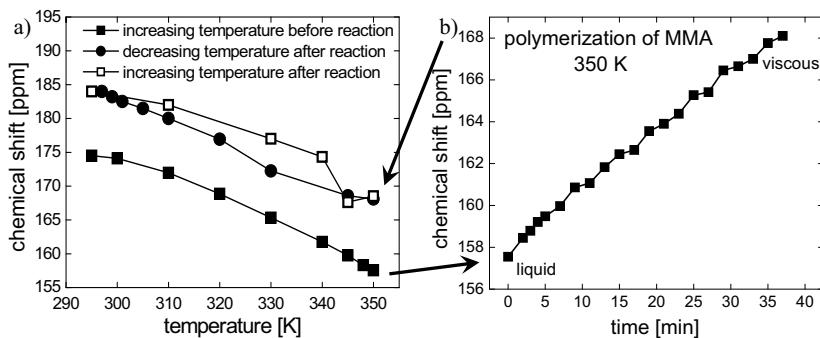
Fig. 4.9 Dependence of the chemical shift on the increasing and decreasing temperature **(a)** and of the reaction time at a constant temperature of 350 K **(b)**.

When increasing the temperature to 350 K, a decrease in the chemical shift with increasing temperature can be seen (Fig. 4.9a) , which is in agreement with the results of Stengle [Ste87] who probed the amorphous state of solid polymers with xenon NMR. Considering the fact that the reaction only starts after AIBN starts generating free radicals, that is after reaching higher temperatures, the decrease in chemical shift is entirely attributed to a decrease in density with increasing temperature, an effect previously noticed also when analyzing the Xe chemical shift in ethanol [Küh04] and more recently obtained from molecular dynamic simulations of Xe chemical shifts in *n*-alkanes [Yua07].

After the stable temperature of 350 K has been reached and the polymerization starts, the chemical shift of Xe dissolved in the reaction bulk increases continuously during the time the reaction is monitored (Fig. 4.9b). This changing in chemical shift can be explained by the changes that occur in the reaction bulk during the polymerization process. Thus, in the beginning, the solution is dominated by the MMA monomers, and in the end it is dominated by the polymer, as the amount of monomer decreases during the polymerization while the polymer chains start to grow. Therefore, the chemical shift observed in the beginning of the polymerization process is assigned to the monomers in the reaction bulk, while the increased values of Xe chemical shift observed in the end of the reaction is assigned to Xe dissolved in the polymer chains. During the reaction, the Xe chemical shift in the reaction bulk is composed of two components, one corresponding to the monomer, and the second one corresponding to the polymer, and the changes in the chemical shift of Xe are assigned to the changing in the monomer-polymer proportion during the reaction. This could also be another explanation for the asymmetric character of the broad line and to the increased linewidth of Xe dissolved in the reaction bulk as a bigger distribution of chemical shifts corresponding to different lengths of the polymer chains is present with increasing reaction time.

After 37 minutes of monitoring the reaction, the temperature is decreased back to room temperature and the reverse effect of increasing of the Xe chemical shift with decreasing temperature can be seen (Fig. 4.9a). Once the room temperature was reached, the temperature was raised back to 350 K and the value of the Xe chemical shift coincides with the value obtained when the reaction was stopped by decreasing the temperature. This proves once again that the changes in Xe chemical shift that occur when increasing and decreasing temperature are due only to temperature changes and not to the polymerization reaction. The small hysteresis observed between decreasing and increasing temperature is due to the small differences between the temperature observed and the actual temperature of the sample given by the fact that it is needed a certain time to reach a stable temperature.

The next step in analyzing the polymerization of MMA with hyperpolarized [129]Xe NMR was to follow the reaction in the absence of the solvent. Therefore, a new solution composed only of MMA and AIBN was prepared and introduced in the sample tube. The reaction was monitored under continuous hyperpolarized [129]Xe flow for 21 minutes (Fig. 4.10a) until the reaction product turned into a solid polymer and the signal from Xe inside the polymer could no longer be seen. The reaction was again monitored at 350 K, and the change in chemical shift with reaction time is presented in Fig. 4.10b.
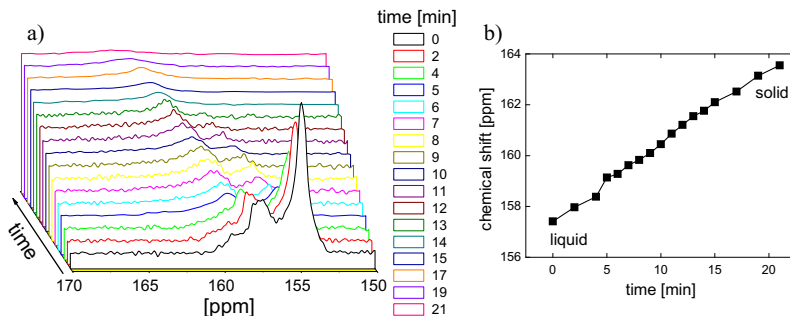
Fig. 4.10 (a) ^{129}Xe NMR spectra acquired during the polymerization of MMA as function of time in the absence of the solvent. **(b)** Chemical shift of Xe dissolved in the polymer versus time for the polymerization of MMA in the absence of butyl acetate.

.   In this case, the separation between the signal from the monomer and form the growing chains of the polymer becomes more clear, as two peaks appear in the spectrum, one at a smaller value of chemical shift, corresponding to the Xe interacting with the monomer, and the second peak with a larger chemical shift corresponding to the Xe interacting with the polymer. Due to the absence of the solvent, the reaction is much faster and it could only be followed for 21 minutes when the reaction product was already a solid and the signal from the Xe penetrating the polymer or on the polymer surface could no longer be monitored. The peak corresponding to the Xe-monomer interaction decreases in intensity with time as Xe interacts less and less with the monomer while the polymer chains start to grow. An increase in the chemical shift with the reaction time is again observed (Fig. 4.10b) as the reaction bulk undergoes a transformation from the liquid state mainly dominated by the monomeric solution to solid state composed mainly of the polymer.

4.4.2 Polymerization of methyl acrylate

The second free radical polymerization investigated using hyperpolarized ^{129}Xe NMR spectroscopy was the polymerization of methyl acrylate (MA) (Fig. 4.11). It is based on the same mechanism described in section 4.4.1 for the polymerization of methyl methacrylate. It is initiated by the free radicals formed by AIBN upon increasing the temperature (Fig. 4.5) and it was investigated in the presence of butyl acetate as solvent for the reaction.
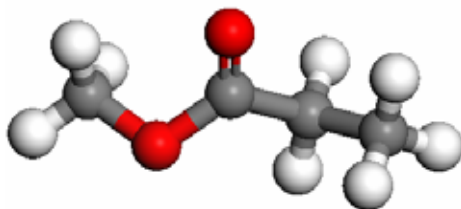
Fig. 4.11 Repeating unit of a PMA chain.

The polymerization reaction of MA was monitored at 350 K in the presence of hyperpolarized [129]Xe, recording [129]Xe NMR spectra at different time intervals during the reaction (Fig. 4.12a). In order to study the growth of the PMA chains during the polymerization process the evolution of the chemical shift of the peak corresponding to the Xe dissolved in the reaction bulk was recorded as a function of the reaction time (Fig. 4.12b). Figure 4.12a shows a series of [129]Xe NMR spectra recorded for approximately two hours during the polymerization of MA. All spectra were referenced to the Xe gas line which was set at 0 ppm, therefore the plots only depict the spectral region corresponding to the Xe dissolved in the reaction bulk.

Fig. 4.12 (a) [129]Xe NMR spectra acquired during the polymerization of MA as function of time. **(b)** Chemical shift of Xe dissolved in the polymer versus time for the polymerization of MA.

The polymerization of methyl acrylate starts after the stable temperature of 350 K has been reached and AIBN starts to decompose and produce free radicals to initiate the reaction. Similar to the polymerization reaction of MMA, a continuous increase of the chemical shift of Xe dissolved in the reaction bulk during the polymerization is observed (Fig. 4.12b). As the reaction bulk starts to be dominated by the polymer with increasing

reaction time, the interaction of the Xe atoms with the polymer starts having a bigger contribution to the chemical shift than the interaction with the monomer, leading thus to an increase in the chemical shift with the growth of the PMA chains.

4.4.3 Copolymerization of methyl methacrylate and methyl acrylate

The copolymerization of methyl methacrylate and methyl acrylate was studied under hyperpolarized [129]Xe flow in order to test how the chemical shift of the Xe dissolved in the reaction bulk changes during the polymerization when two different polymers are present in the reaction. The purpose of monitoring this reaction was to see which one of the two polymers has a greater contribution to the changing of the chemical shift of Xe dissolved in the reaction bulk. For this purpose [129]Xe NMR spectra were recorded during the copolymerization by turning on the hyperpolarized [129]Xe flow only 20 seconds before the measurement in order to insure a longer monitoring time with no sample loss due to a continuous Xe flow. At the temperature of 350 K, the free radical polymerization starts, and the reaction was monitored for 7 hours (Fig. 4.13), until the peak corresponding to Xe inside the polymer was no longer visible due to the fact that after 7 hours the polymer was already solid, and the Xe signal from the surface was too low to be detected.

The [129]Xe NMR spectra recorded at different moments during the polymerization are given in Fig. 4.13a, showing the decrease in signal amplitude during the polymerization as the reaction bulk transforms from a liquid solution to a solid and less Xe atoms can penetrate the reaction bulk. During the reaction a continuous increase of the chemical shift with increasing reaction time is observed (Fig. 4.13b).
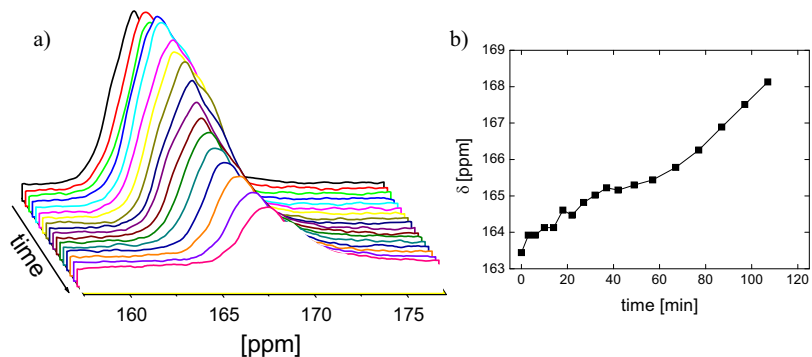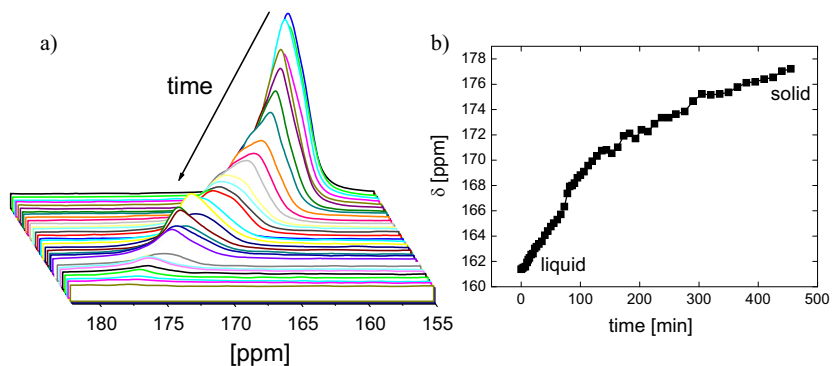

Fig. 4.13 (a) [129]Xe NMR spectra acquired during the copolymerization of MA and MMA as function of time. **(b)** Chemical shift of Xe dissolved in the reaction bulk versus time for the copolymerization of MA and MMA.

Two different slopes are observed for the increase of the chemical shift with reaction time for the copolymerization of MA and MMA. In order to understand this process, two new solutions were prepared and the polymerizations of MA and MMA were monitored again under exactly the same conditions as the copolymerization of MMA and MA stopping the Xe flow between measurements in order to preserve the sample to have a longer reaction time. Thus, the chemical shifts of PMMA and MMA obtained from these measurements could be accurately compared to the chemical shifts during the copolymerization or MA and MMA (Fig. 4.14).
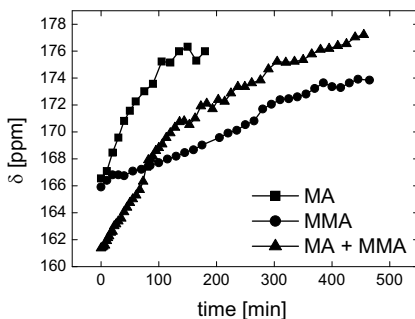
Fig. 4.14 Comparison between the chemical shifts during the polymerization of MA, MMA, and the copolymerization of MMA and MA.

Figure 4.14 shows that the polymerization reaction of methyl acrylate is much faster than the other two reactions, while the slowest reaction is the polymerization of methyl methacrylate. Thus it can be concluded that in the curve corresponding to the copolymerization of MA and MMA, the first 3 hours with a bigger slope are influenced by the fast polymerization of MA, while the last 4 hours with the smaller slope are influenced by the slow polymerization of MMA.

4.5 Conclusions

This study reports the successful application of hyperpolarized [129]Xe NMR spectroscopy into investigating free radical polymerizations which are of high technological interest due to a large variety of industrial applications. The polymerization reactions of methyl methacrylate and methyl acrylate, as well as the copolymerization of methyl acrylate and methyl methacrylate were monitored in real-time under hyperpolarized [129]Xe flow. In all cases an increase in the chemical shift of the Xe atoms in the reaction bulk with increasing

reaction time at a constant temperature of 350 K was recorded. This is explained by the changing in the composition of the reaction bulk as the quantity of monomers starts to decrease and the polymeric chains grow larger during the polymerization. Thus the Xe-monomer interaction is gradually replaced by the Xe-polymer interaction leading to the increase of the chemical shift with the increase of the polymer chains during the reaction.

Comparing all three free radical polymerizations presented here, the characterization of the copolymerization of MA and MMA was possible, thus concluding that in the beginning it is dominated by methyl acrylate and in the end by methyl methacrylate.

5 Pieces of History Revealed by the NMR-MOUSE

5.1 Introduction

What is death? What happens to a person when he dies? Is everything over or does the soul continue his journey in another world? These are some of the questions that we all ask ourselves sooner or later, trying to give a meaning to life and death, hoping that we have not lived in vain, hoping that in the moment we die there is something else awaiting, that we will continue on existing one way or another… Throughout history people had different beliefs about death, they found different explanations for it, and manifested different attitudes towards death.

Since ancient times death was not considered the end, but simply the passage to the afterlife. The ancient Egyptians considered that the preservation of the body after death was very important for the passage in the afterlife. Therefore, they were trying to keep the body intact after death, by mummification, so that the *ka* and the *ba*, the essence or the life force and the manifestation of the soul of a person would reunite in the afterlife, and by unification they would form the *akh* which is the form under which the deceased lived in the afterlife. If the mummy was not well prepared and the body not well preserved, the *ka* and the *ba* would forever wonder in the underworld trying to find each other so they would reunite into the *akh* [Tay01]. In order to help the *akh* in his journey in the underworld, papyrus scrolls containing chapters from the Book of the Dead [Fau72, Fau94, Ash00] were placed in the deceased's tomb. These texts would help the *akh* find its way in the underworld and overcome any obstacles that he may encounter in his journey. Together with the scrolls, magic amulets were placed in the tomb in order to protect the spirit in the afterlife. These are the basic funerary rites that the ancient Egyptians used to practice in order to insure that a person would keep on existing in the afterlife.

The Egyptians are not the only ancient people who would mummify the deceased to prepare him for the afterlife. The first recollection of mummification is form the years 5000 B.C attributed to the Chincorro culture that was dated as far as 7000 B.C. on the Atacama Desert coast, the region which is now the northern Chile and the southern Peru

[Arr08]. The mummies found in Peru dating from the Inca period around 500 years ago are both artificial mummies of the dead kings and natural mummies of children sacrificed for the Inca religious beliefs. These were mummified by the extreme coldness and dry mountain air where they were taken for the sacrifice. Another natural mummy preserved due to low temperatures is Ötzi the Iceman, a 5300 year old glacier mummy found in the Alps on the border between Austria and Italy.

Since the discovery of the first mummy, the scientific world was fascinated by the subject, and since then mummies have been subjected to various kinds of scientific investigations. One of the most famous mummies is the mummy of Tutankhamun, an Egyptian Pharaoh from the 18th dynasty whose tomb was discovered in 1925. Using computer tomography to scan the mummy of King Tut, Dr. Zahi Hawaas and his team determined Tutankhamun's age of death at around 19 years old, and they were able to rule out murder as the cause of death, as previously thought because of the missing skull pieces, and associated them to the embalming process [Haw05]. Another mummy whose 3D reconstruction was made using X-ray computer tomography is the mummy of Tjentmutengebtiu, a priestess from the 22nd dynasty revealing new information related to the mummification process [Bal94]. CT was successfully applied for 3D reconstruction of mummies [Jan02, Mar88, Mag89, Ces03], to identify internal anatomy [Hof02a], or for pathological investigations [Hof02b, Rüh04]. The natural glacier mummy Ötzi, is another mummy that received a great attention from the scientific world. Thus, investigations on Ötzi have been done in order to determine the cause of death, the age of the mummy and the way he became a mummy [May97, Rol97, Gos02, Mur03, Rüh06].

After learning what death meant to the ancient people and how they were preparing for the afterlife it's time to take a look at the modern person and his view of death and afterlife. The views of contemporary people on death are very vast and contradictory. Some say the person's soul continues to exist in another world, others say it all ends the moment the body dies, some think after death we are reunited with our loved ones who are waiting for us on the other side, and there are those who live forever though the legacy they leave behind. This is the case of great men in history, science and art who will always be remembered for the great things they achieved during their lives and their memory will never fade away. Among these great personalities, with relevance for this chapter is Charlemgane, a man who played an important role in history, and the violin makers who left behind memorable pieces of art.

Charlemagne, also known as Karl der Grosse for the Germans, or Charles the great for the English, was the king of Franks and Emperor of the Holy Roman Empire between 742 and 814. He was the ruler of a kingdom which was formed by today's Germany, France, The Nederlands, Belgium, Switzerland, and parts of Italy, Spain and Austria, and today the resting place for his remains is Aachen, Germany. His life and his political and religious views were the inspiration for the work of many historians and novelists [Rus30, Eas61, Ein69, Wil06], but no scientific investigations have been done on the remains of Charlemagne until now. This is the first scientific study of the bones of Charlemagne together with other ancient bones.

Building a violin is an art which began with the Amati family in Italy around the year 1555 and since then very few people could master this technique to create a truly memorable piece of art. Among them history of art mentions the names of the Amaty family, the Guarnery family, and the Stradivari family. Among the famous violinists who gave life to these instruments that captivated the human ear one might recall the names of Johann Sebastian Bach, Antonio Vivladi, Joseph Haydn, Wolfgang Amadeus Mozart, George Enescu, and many others.

Precious objects such as the violins are being scientifically investigated for three main reasons: for a better understanding of the physical mechanism on which they are based, to try to differentiate an authentic violin from a fake, and to find a way to preserve such an art work. For this purpose, methods such as mass spectrometry, and x-ray fluorescence were applied to analyze the varnish for the violins and establish its chemical composition [Chi08, Ech08a, Ech08b]. For the understanding of physical processes that lead to the use of a violin for different kinds of music from solo to orchestra, the mechanical system of a violin was analyzed [Hut98]. The mechanical behavior was tested when studying the upper and lower bow-force limits for violins [Sch08], and the acoustical properties of violins were tested function of the physical changes in a violin [Fri07]. CT was proved to be a reliable tool for the characterization of violins; it is able to detect defects in violins, to detect changes of the wood thickness or density [Sir97].

The aim of this study is to apply the NMR-MOUSE for the investigation of ancient mummies and bones, as well as for the analysis of old masterpieces. The advantage of the NMR-MOUSE is the fact that it is a non-invasive tool which can be applied for both studies, first for the analysis of mummies without disturbing the akh in the afterlife by damaging the body he left behind, and second for the investigations of violins and bows, at the same time being able to maintain the masterpieces of great artists intact. Not only is it a

non-invasive method for the characterization of materials, but it is also a portable device, meaning that the samples can be measured in the museums or any other environment that hosts them without having to move the samples out of their medium which is important for their preservation.

5.2 The NMR-MOUSE

The NMR-MOUSE is an open and portable sensor that can detect NMR signals from large samples external to the magnet, giving access to a variety of applications which cannot be tackled in closed magnet geometries. The profile NMR-MOUSE (Fig. 5.1) consists of four permanent magnet blocks positioned on an iron yoke. Two magnets are polarized along y, and two along $-y$, producing a magnetic field B_0 above the magnet parallel to the surface of the sensor. For analysis, a radio-frequency (rf) magnetic field B_1 is applied by means of a rectangular rf coil mounted in between the magnet blocks, which is perpendicular to B_0. With this arrangement, an NMR signal can be collected from a thin and flat slice located at a fixed distance of 3 to 10 mm from the magnet surface [Per05]. The advantage of measuring NMR signals in the stray field of a magnet is that there are no restrictions to the sample size as for conventional NMR, where the sample has to fit inside a magnet. However, the sensitive volume is restricted to regions near to the surface of the object under examination [Edi96].
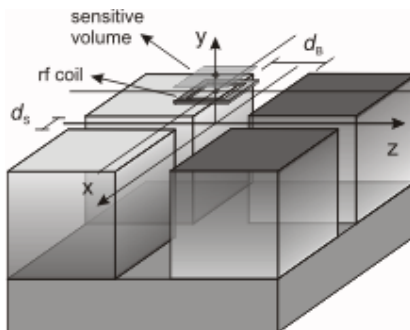

Fig. 5.1 The magnet geometry used to generate a highly flat sensitive volume in the stray field [Per05].

With this profile NMR-MOUSE [Per05], high resolution profiles can be recorded by placing the sensor on a stepper-motor driven, high-precision automatic lift which changes the distance between the sensor and the sample (Fig. 5.2). By varying this distance,

the sensitive slice is shifted through the object, and depth profiles can be measured with a resolution better than 10 μm. The lateral dimensions of the sensitive slice are 20 mm by 20 mm.
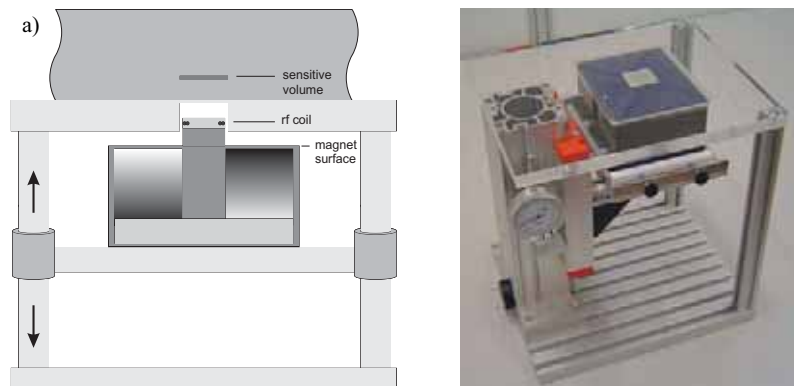

Fig. 5.2 Schematic representation of the lift used to reposition the sensitive slice across the sample [Per05]. The sample is placed on the top plate, which is parallel to the mobile plate on which the sensor is mounted. The magnet surface, the rf coil that defines the sensor surface, as well as the relative position of the sensitive slice are identified. b) Set-up consisting of the NMR-MOUSE and the lift used for NMR measurements.

Non-invasive measurements with single-sided NMR have been explored during the last 10 years in a large number of applications [Blü08, Per05] such as well-logging [Kle96], moisture detection in composites [Pra01], medical diagnostics [Hak00, Blü00], food science [Ped03], conservation of cultural heritage [Blü03a, Rüh07], and quality control [Mat98, Blü03b].

The most important contrast parameters employed by the NMR-MOUSE are the signal amplitude corresponding to the proton density, and the transverse relaxation times T_2 which relates to the molecular mobility and the effective self-diffusion coefficients of liquids within the sensitive volume. This information is obtained using the Carr-Purcell-Meiboom-Gill (CPMG) pulse sequence (Fig. 5.3a). For the determination of the transverse relaxation times, the decay curve measured with the CPMG sequence is fitted with a biexponential function to determine the short and the long T_2 relaxation times which are ascribed to the rigid and mobile phases of the investigated polymer. The proton density is estimated from the integration of the signal corresponding to the first part of the CPMG decay (Fig. 5.3b).
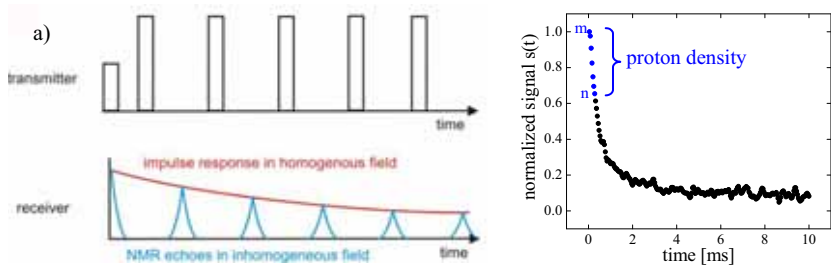
Fig. 5.3 (a) CPMG pulse sequence and the NMR response in inhomogeneous fields [Blü05] and **(b)** Estimation of the proton density from the T_2 decay by integration of the first echoes.

5.3 Samples

5.3.1 Mummies and bones

Both ancient and more recent mummies and bones were investigated using the NMR-MOUSE. One of the ancient mummies that participated in this study is Ötzi, the Iceman (Fig. 5.4a), a 5300 year old glacier mummy which was found in the Alps, and is now hosted by the South Tyrol Museum of Archaeology in Bozen, Italy. Ötzi's measurements were done *in situ* in the cold storage room of the museum, where Ötzi's body is preserved at the constant temperature of -6.12° C and constant humidity of 99.42%. Before being able to measure Ötzi, test measurements with the NMR-MOUSE were done on a modern mummy, Ötzi3 (Fig. 5.4b), prepared by the Institute of Anatomy, Innsbruck. The measurements were done at the morgue of the General Hospital Bozen in order to find the right parameters for the measurement of Ötzi.
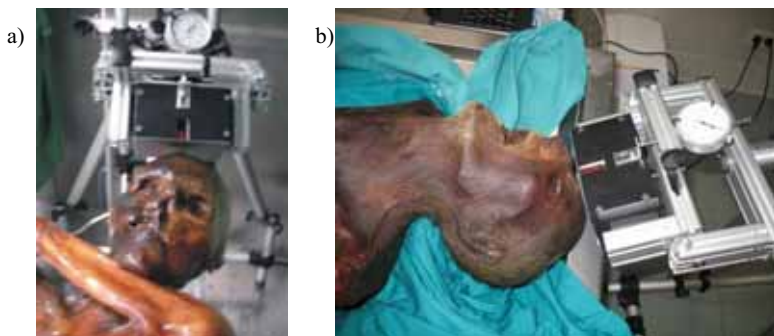
Fig. 5.4 (a) Ötzi, the Iceman, a 5300 year old natural mummy and **(b)** Ötzi3, a modern mummy.

The NMR-MOUSE was successfully applied on another natural mummy – a Peruvian mummy (Fig. 5.5a), and Egyptian mummy head (Fig. 5.5b), a 100 years old modern skull (Fig. 5.5c), and a 1000 years old skull (Fig. 5.6d).
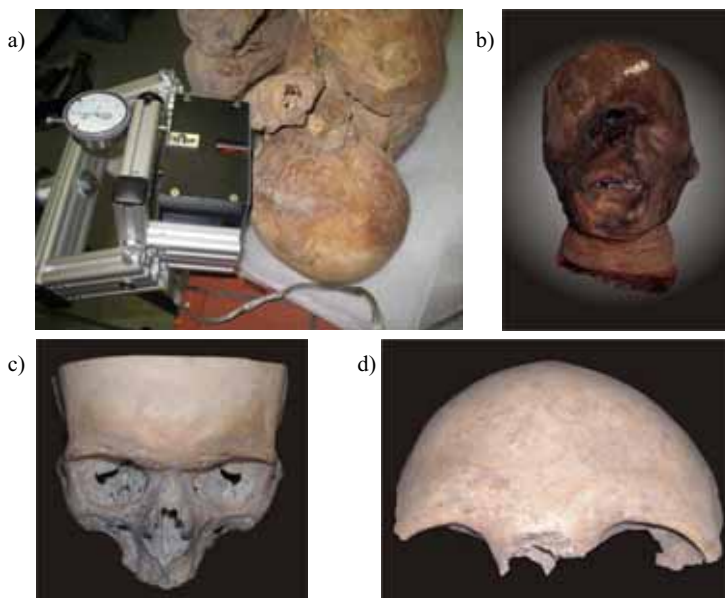
Fig. 5.5 (a) Peruvian mummy, **(b)** Egyptian mummy head, **(c)** recent skull, and **(d)** old skull.

Besides skulls, other bones investigated with the NMR-MOUSE are several tibiae, and among them an important one is the one belonging to Charlemagne (Fig. 5.6), whose remains are currently kept in the treasury of the Aachen Dom.

Fig. 5.6 The tibia of Charlemagne.

5.3.2 Violins and bows

From the pieces of art left by the great masters, several violins and bows, both old and new were analyzed with the NMR-MOUSE (Fig. 5.7). Among the investigated violins are numbered a Paulus violin from 1890, a Homolka violin from 1823, and other several

violins fabricated in the period 1700 untill 1900. The bows investigated were fabricated between 1800 and 2000.

Fig. 5.7 The NMR-MOUSE setup to measure the depth profiles for the violins and bows. It consists of the NMR-MOUSE which is placed on top of a movable plate, which, controlled by a step motor, can automatically move the sensor with respect to the sample so that depth profiles can be acquired.

5.4 Results and discussion

5.4.1 Mummies and skulls

It has been shown before that the NMR-MOUSE is capable of differentiating different layers in paintings [Blü08], which was possible due to the differences in the T_2 values of different paints. Considering that different anatomical layers experience different proton densities and mobilities, the first aim of this study was to apply the NMR-MOUSE for the investigations of mummies to distinguish the different anatomical structures and for the study of bones to detect the changes in bone density that could eventually lead to clearing bone density issues for clinical applications, such as detecting and preventing osteoporosis.

The test measurements with the NMR-MOUSE to verify whether it can be applied for investigations of mummies were done on an Egyptian mummy hand (Fig. 5.8a) and an Egyptian mummy finger (Fig. 5.8b) by measuring depth profiles through the samples. Thus, in the case of the mummy hand, a clear delineation between the textile wrapping and the mummified soft tissue is seen (Fig. 5.8c), while for the mummy finger the depth profiles show a varying proton density from the nail to the finger pad (Fig. 5.8d). This first attempt

was successful and proved the ability of the NMR-MOUSE to detect different anatomical layers due to the change of proton densities from one anatomical structure to another.
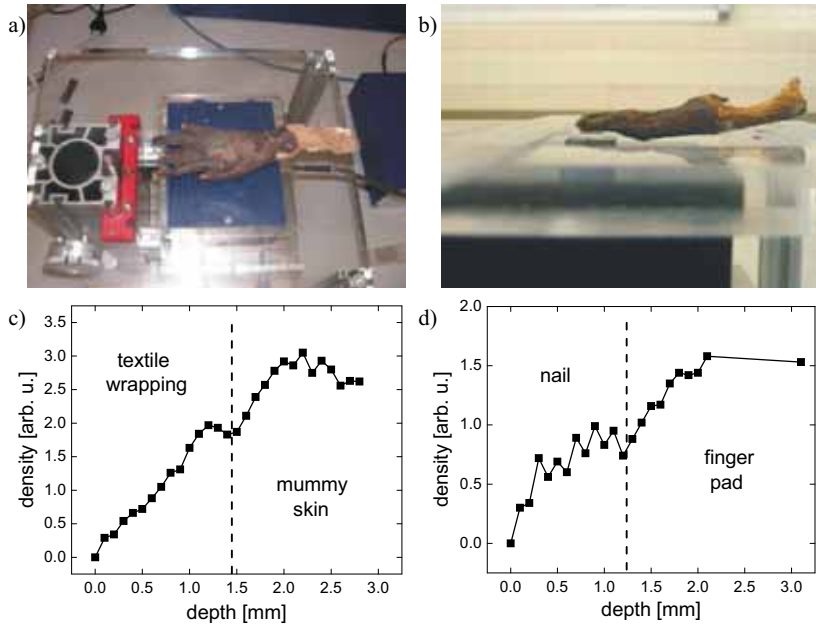
Fig. 5.8 Photos: Test samples **(a)** Egyptian mummy hand, and **(b)** Egyptian mummy finger. **(c)** Depth profile for the Egyptian mummy hand. **(d)** Depth profile for the Egyptian mummy finger.

With this proof that the NMR-MOUSE is capable to distinguish different anatomical layers, the next step was to apply the NMR-MOUSE for the investigation of the frontal region of a variety of different skulls, varying from ancient mummies to modern human skulls. Thus, the first measurements were done on the modern model cadaver of an 80 year old man – Ötzi3 (Fig. 5.4b) – a modern mummy prepared by the Institute of Anatomy in Innsbruck by air drying to reduce his body weight to the weight of Ötzi. Using Ötzi3 as a reference sample, depth profiles were acquired in the frontal region of his head (Fig. 5.9a). Here, one can differentiate the different anatomical layers due to the T_2 contrast introduced in the density profiles by extending the integration limit of the CPMG echo train. The CPMG decays for different layers in the profile are shown in Fig. 5.9b. The assignment of these anatomical layers was done according to Fig. 5.10, where one can see the different layers of soft tissue and the bone structure of the forehead region.

Fig. 5.9 (a) High resolution depth profiles through Ötzi3's forehead, and **(b)** the T_2 relaxation curves at the positions indicated in the depth profile.
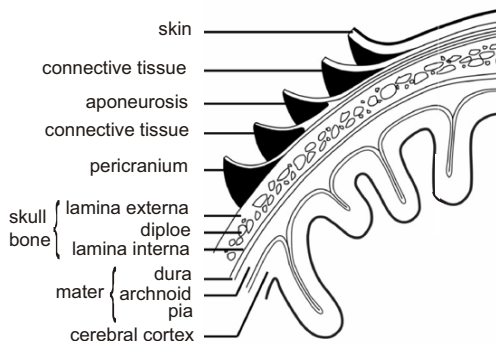
Fig. 5.10 Schematic drawing of the anatomy of the forehead region (adapted from [Agu91]).

The measurements performed on Ötzi3's forehead lead to a clear delimitation of the different soft tissue and bone layers due to the differences in the transverse relaxation times of each anatomical structure. Thus, due to the T_2 contrast imposed in the density profiles by integrating increasing numbers of echoes in the CPMG decay, one can distinguish the signal coming from the skin, the tendon and the bone.

Using the same method, the forehead of Ötzi was measured with the NMR-MOUSE *in situ* in the cold storage room of the Museum of Archaeology in Bozen, Italy. For comparison, the depth profiles were acquired through the forehead of Ötzi (Fig. 5.11a) in the same region of the forehead where the depth profiles were acquired for Ötzi3. The density profiles reveal the clear separation between three different layers. The exterior layer, which presents the longest CPMG decay (Fig. 5.11b), was assigned to the ice covering Ötzi's body, as he is kept at a constant temperature of -6° C for conservation. The second and third layers in the depth profile were assigned to the soft tissue and the bone, respectively, by means of T_2 contrast imposed in the density profile measurements.
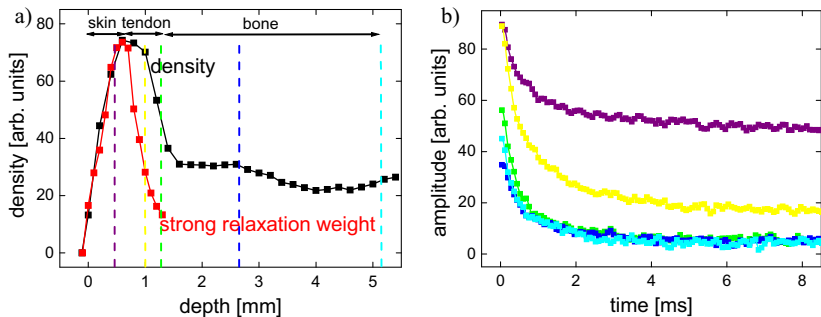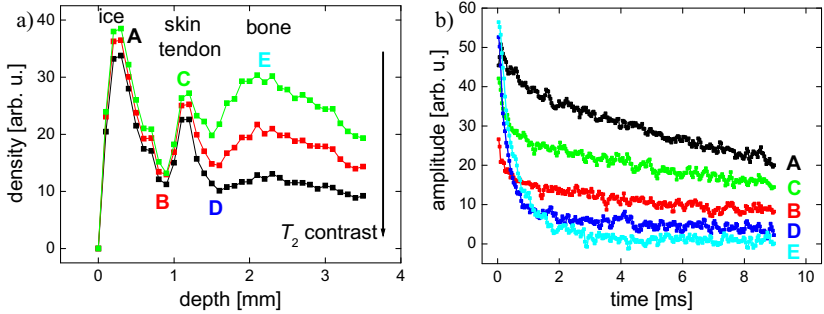
Fig. 5.11 (a) High resolution depth profiles through Ötzi's forehead, and **(b)** the T_2 relaxation curves at the positions indicated in the depth profile.

By integrating more echoes in the profile, the T_2 contrast is increased, and the short T_2 of the bone can be seen in comparison with the longer T_2 of the soft tissue. Taking advantage of the fact that the NMR-MOUSE is capable of revealing information about rigid samples with short T_2 such as the bone layer of the two mummies, in the following depth profiles through different skulls were acquired. Thus, the frontal region of an old skull, a modern skull, as well as the skull of a Peruvian mummy were analyzed with the NMR-MOUSE, recording depth profiles (Fig. 5.12) with the integration of the very first echoes of the CPMG decay to reveal information about the proton density with no influence of the T_2.
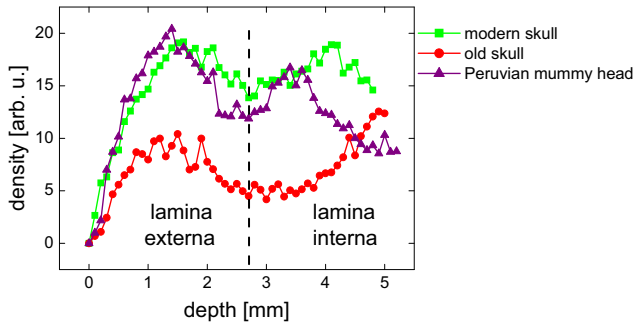
Fig. 5.12 Depth profiles through the frontal region of three human skulls, a modern skull, an old skull, and the skull of a natural preserved Peruvian mummy.

The depth profiles for all skulls show a density distribution with a minimum in the center. This is in agreement with the dense bone structure for the inner and outer surfaces of the skull and a spongeous inner part as pictured in Fig. 5.10. However, the thickness of the skull bone varies randomly and may exhibit different thicknesses of the dense or the

spongeous regions. Thus, Fig. 5.12 reveals a spongeous zone of the old skull double than it can be seen in the case of the Peruvian mummy head.

To understand the signal amplitude variation in the bone region, the depth profiles acquired through skulls of different ages were analyzed and compared (Fig. 5.13). Thus it can be seen that the bone profiles of the modern skull and the Peruvian mummy head overlap perfectly, while the density profiles of the Egyptian mummy head and the historic skull are lower, and the bone region of the frozen Iceman has the highest proton density of all the measured bones. The lower amplitudes of the Egyptian mummy heads and the historic skull can be explained by a lower bone density due to partial decay of the bone structure over several centuries.
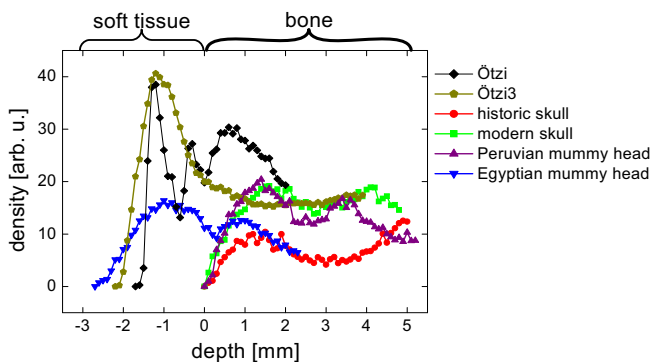
Fig. 5.13 Depth profiles of different skulls. The difference in bone density signals can be judged from the differences in amplitude of the depth profiles of the dry bones. By super-imposing the various depth profiles, one can distinguish different anatomical layers between soft-tissue and bone and even within the bone.

For a better understanding of the high proton density in the bone region of Ötzi, a new set of depth profiles was acquired on two small pieces of bone, one from the historic skull and the other from the modern skull. On each piece of bone three depth profiles were recorded: one on the dry samples, one after keeping the sample in water for 24 hours, and one after freezing the sample by keeping the wet bone in the freezer for 48 hours at -18° C. The depth profiles for the wet and frozen modern skull (Fig. 5.14a) show identical proton densities for the wet and frozen bone, indicating the non-freezable character of the water trapped in the pores of the modern skull. The profiles recorded for the historic skull (Fig. 5.14b) show a much higher intensity of the signal coming from the wet bone than the dry one compared to the amplitudes recorded for the modern skull, indicating higher water uptake of the old skull pores, which leads to the conclusion that the pores of the historic skull are larger than the pores of the modern skull.
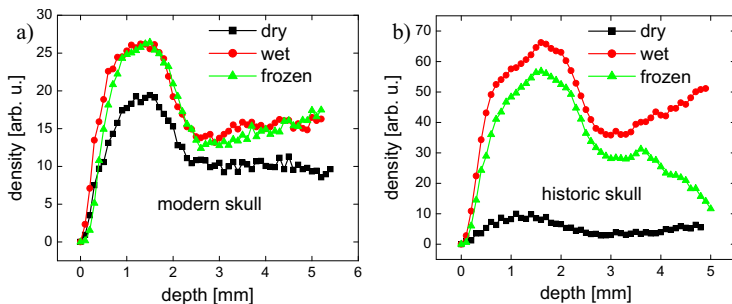
Fig. 5.14 Depth profiles recorded for **(a)** the modern skull and **(b)** the historic skull under different physical conditions of the bone: dry, wet, and frozen.

These last measurements recorded on the two skulls under different physical conditions lead to a possible explanation of the high signal amplitude for the bone region of the Iceman compared to the other skulls. Thus, the high proton density of Ötzi's skull could be explained by the fact that his skull bone is filled with water and even though the body is kept at -6° C, the water is in his skull pores is not frozen as concluded from the analysis of the depth profiles in Fig. 5.14.

5.4.2 Tibiae

The studies performed on mummies and skulls proved that the NMR-MOUSE is able to detect changes in bone density from one specimen to another. The next step in the investigation of bones was to use the NMR-MOUSE for studying long human bones such as tibiae with the aim of gathering information about bone density which could be used for clinical applications such as osteoporosis. For this purpose several tibia have been analyzed, including the tibia of Charlemagne. Before using the NMR-MOUSE for bone density measurements for clinical purposes it is important to understand the anatomy of the tibia (Fig. 5.15), to understand how the proton density can be correlated to the bone structure. The tibia is one of the long bones of the body, and it can be divided into three regions, namely the epiphysis, the metaphysic, and the diaphysis. The epiphysis is the rounded end of the bone, it consists mainly of cancellous (spongy or trabecular) bone, with lower bone density. The metaphysic is the part adjacent to the epiphysis in the adult. The diaphysis is the cylindrical shaft of the bone made up of cortical (compact) bone, with higher bone density, surrounding a central cavity containing cancellous bone. The cortical bone is thickest in the mid-portion of the shaft, the cancellous bone being relatively diminished in this portion of the bone [Nat05].
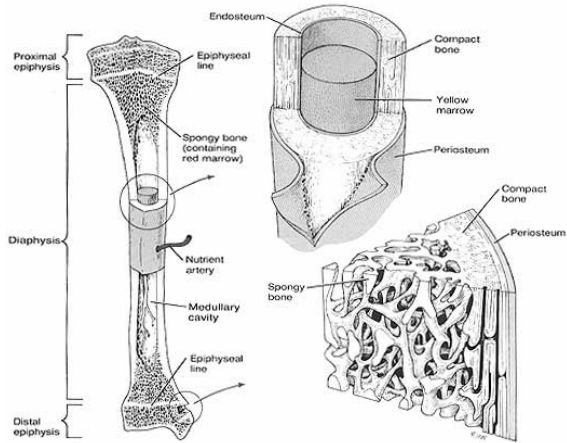
Fig. 5.15 The structure of human tibia. One can distinguish the cortical bone of the epiphysis from the compact bone of the diaphysis.

With a better understanding of the tibia anatomy, several tibiae have been analyzed both in the diaphysis region and in the epiphysis region with the aim of using the NMR-MOUSE for detecting the changes in bone density, to try to distinguish the cortical bone from the spongy bone. In the following the example of an old, fragmented tibia (Fig. 5.16a) referenced as B95 (private collection of F. Rühli) is shown, where the depth profiles (Fig. 5.16b) acquired with the NMR-MOUSE are compared with the CT images for a better assignment of the profiles.
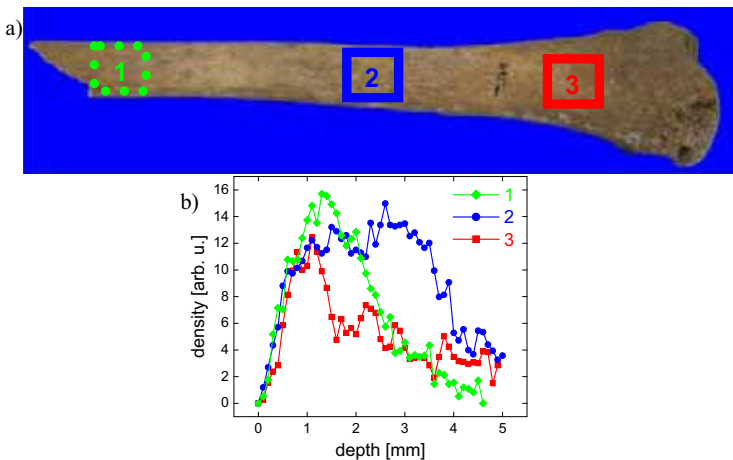
Fig. 5.16 (a) Photo of the B95 fragmented tibia and **(b)** depth profiles recorded in the spots marked on the tibia.

Depth profiles were recorded in the diaphysis region, both in the region where it was broken and deteriorated (Fig. 5.17a), and in the region where the tibia is intact (Fig. 5.17b), and also in the epiphysis region (Fig. 5.17c).

Fig. 5.17 Comparison of depth profiles recorded with the NMR-MOUSE for a fragmented tibia and the information revealed by the CT images. Three spots of the tibia were studied closely: **(a)** the region of the diaphysis was broken, **(b)** the region where the diaphysis is intact, and **(c)** the epiphysis region.

For the point where the tibia was broken (Fig. 5.17a), both the depth profile recorded with the NMR-MOUSE, and the corresponding CT image show a short region of high intensity, corresponding to the compact bone, and a region of lower intensity corresponding to the spongy bone. The same observation was made for the other region of

the diaphysis which was analyzed (Fig. 5.17b), except for this point a much larger distribution of high intensities can be seen. With the help of the CT image, this was assigned to the compact bone which has a bigger thickness in the diaphysis region where the bone is intact. In the case of the epiphysis (Fig. 5.17c), the bone is less dense, resulting in a lower signal amplitude of the depth profile. Two different thin layers of cortical bone separated by cancellous bone are observed in the CT image. These two layers are also observed in the depth profile, and as the signal decreases only the spongy bone of the epiphysis is detected.

After having the proof that the NMR-MOUSE complemented by computer tomography can provide relevant information related to the bone density, the tibia of Charlemagne (Fig. 5.18a) was analyzed using the same methods, recording depth profiles in different regions of the tibia and comparing them with the CT images (Fig. 5.18b).
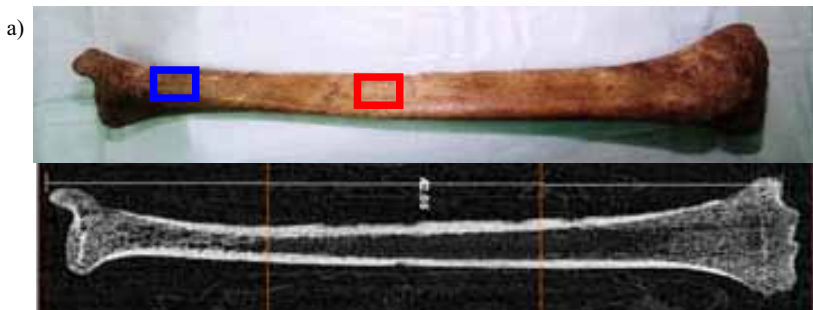
Fig. 5.18 (a) The tibia of Charlemagne. The regions where depth profiles were acquired are marked on the tibia. **(b)** CT image of the complete tibia.

Depth profiles were acquired both in the epiphysis region (Fig. 5.19a) and in the diaphysis region (Fig. 5.19b) and compared to the corresponding CT images. Thus, the depth profile recorded in the epiphysis region (Fig. 5.19a) shows a density distribution, varying from high proton density corresponding to the cortical bone with higher bone density and gradually decreasing in intensity as the spongy bone takes the place of the cortical bone at a depth of 2-2.5 mm. The high amplitude of the profile recorded in the diaphysis region (Fig. 5.19b) corresponds to the high proton density of the cortical bone present in the diaphysis and seen also in the CT image. Here only the cortical bone is seen, which has a thickness of about 5 mm resulting both from the depth profile and from the CT image.
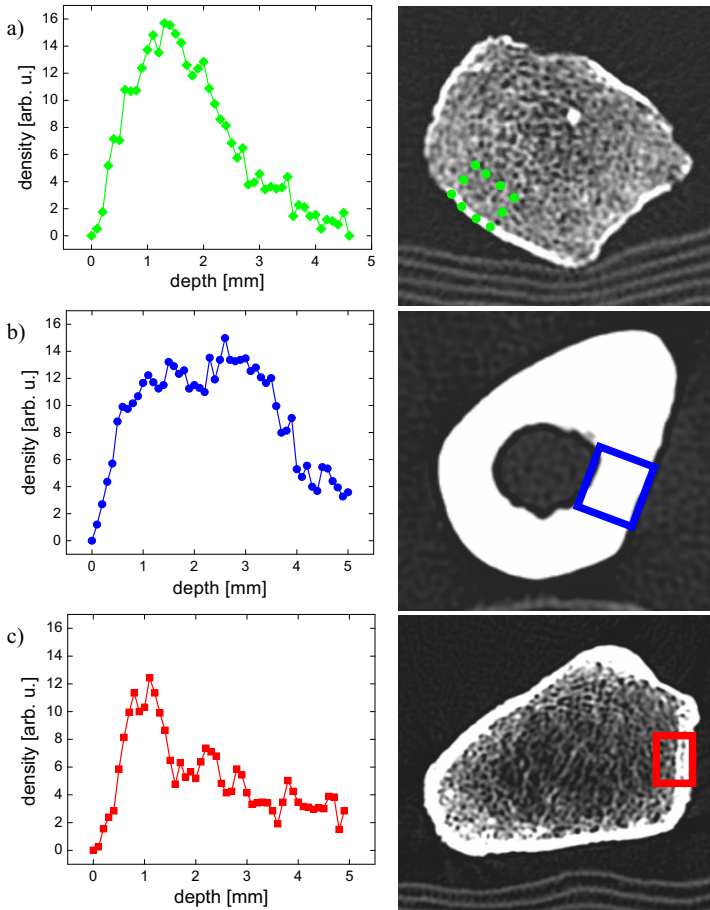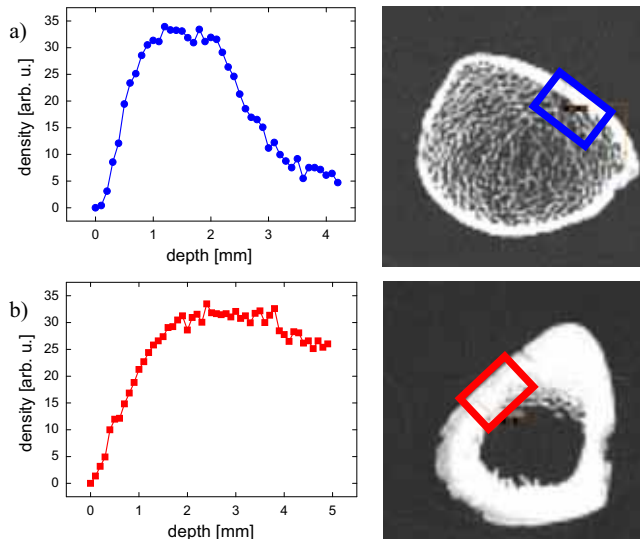
Fig. 5.19 Comparison of depth profiles recorded with the NMR-MOUSE for the tibia of Charlemagne and the information revealed by the CT images. Two regions of the tibia were studied closely: **(a)** the epiphysis region, and **(b)** the diaphysis region.

By comparing the amplitudes of the profiles recorded for the B95 tibia and the ones of the tibia of Charlemagne, a much higher signal intensity is seen for the tibia of Charlemagne, both for the epiphysis (Fig. 5.20a) and for the diaphysis (Fig. 5.20b). The explanation for the high signal amplitude of the tibia of Charlemagne could be related to the organic substances which were used for the treatment of the bones in order to insure a good preservation of the remains of Charlemagne.
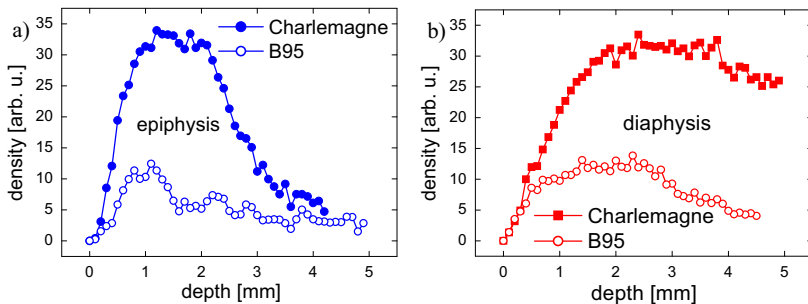
Fig. 5.20 Comparison of the depth profiles of the B95 tibia and the tibia of Charlemagne. Both the profile recorded for the epiphysis and for the diaphysis of Charlemagne show a proton density three times higher than the density of the B95 tibia.

5.4.3 Violins and bows

Another area of cultural heritage where an understanding of materials is important is the construction and preservation of a violin. For this purpose several violins and bows of different ages and woods were studied using the NMR-MOUSE. Therefore, depth profiles were recorded both for the violins (Fig. 5.21a) and for the bows (Fig. 5.21b) with the aim of detecting changes in the materials for the purpose of differentiating a genuine violin from a fake one.
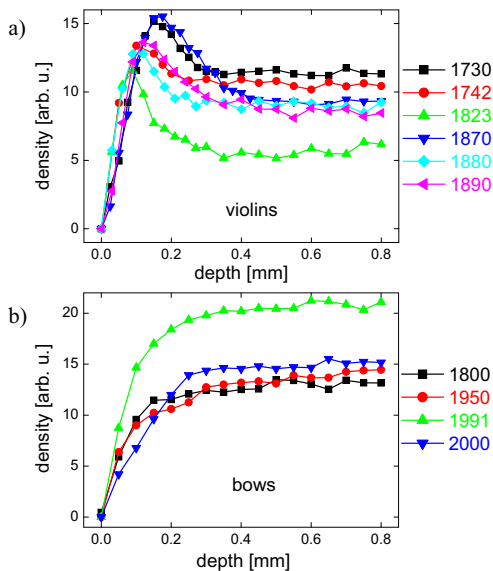
Fig. 5.21 Depth profiles recorded for **(a)** violins and **(b)** bows of different ages. The integration of the first two echoes was used for the density profiles to eliminate the T_2 contribution.

In the case of the violins, a clear differentiation between the wood and the varnish layer on the wood surface can be seen (Fig. 5.21a). According to the depth profiles, the varnish layer varies from one violin to another ranging from 100 μm to 300 μm. Taking a closer look at the depth profiles of the bows (Fig. 5.21b), no clear differentiation between wood and the varnish layer can be seen. This could be explained by similar T_2 values for the varnish and wood given by the fact that the wood used for the building the bows is different than the one used for building the violins. This can be clearly seen in Fig. 5.22, where T_1 (Fig. 5.22a) and T_2 (Fig. 5.22b) at different depths are shown for two examples: the 1742 violin and the 2000 bow. Thus, in the case of the violin, both T_1 and T_2 values in the wood region are approximately twice as high as for the varnish layer, while in the case

of the bow, a much smaller difference between the T_1 and T_2 values for wood and paint is observed.
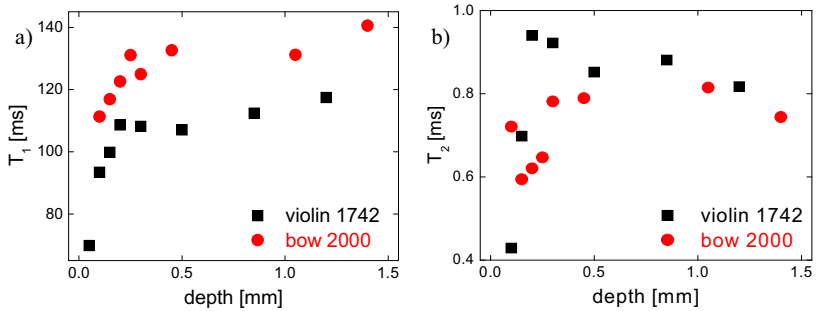
Fig. 5.22 (a) T_1 and **(b)** T_2 at different depths inside the violins and bows. The varnish layer can be differentiated from wood by the smaller values of T_1 and T_2 in the varnished area.

Since the wood quality and wood density plays a very important role in the quality of the instrument and the sounds it is able to reproduce, we will next focus only on the results obtained for the wood region of the instruments. Thus, by plotting the T_1 (Fig. 5.23a) and T_2 (Fig. 5.23b) function of the average proton density obtained from the depth profiles for the wood region, a clear separation between the wood used for building violins and the one used for the bows is obtained.
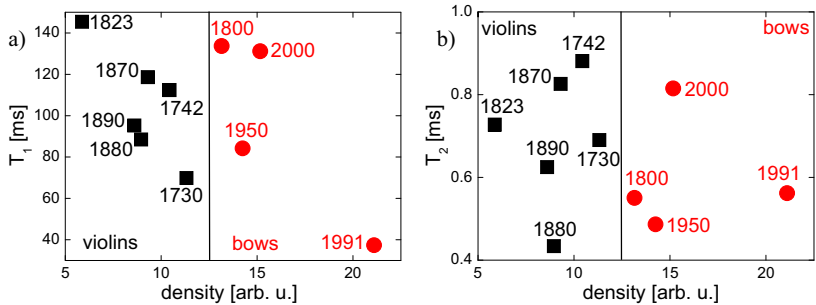
Fig. 5.23 (a) T_1 and **(b)** T_2 plotted against the average proton density of the wood can provide a good differentiation between the violins and the bows given by the different types of wood used for their construction.

By further analyzing the proton density of the wood function of the fabrication year, two different patterns are encountered, one associated with the violins and the other with the bows. Thus, a decreasing proton density with the fabrication year is observed, while the proton density of the bows increases with the fabrication year (Fig. 5.24). This could lead a

method of detecting of the fabrication year of a violin or bow by analyzing the proton density of wood with the NMR-MOUSE.
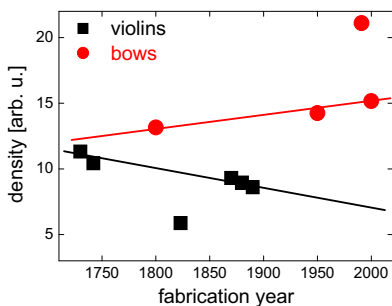
Fig. 5.24 Changes that occur in the proton density of the wood of violins and bows with increasing fabrication year.

Both for the violins and for the bows, one of the samples doesn't fit in the observed trend of decreasing or increasing density with the fabrication year. There are two possible explanations for these exceptions. The first cause could be the different type of wood used for that particular violin or bow, and as seen before, the density changes with the type of wood. A second explanation could be related to the authenticity of the violin or bow, whether or not the sample was fabricated in the indicated year. To clarify this problem, more samples have to be analyzed with the NMR-MOUSE in order to understand whether it's the type of wood or it's age cause the change in proton density.

5.5 Conclusions

The NMR-MOUSE has been successfully applied to visualize spatial depth profiles in historic natural and artificial mummies, a recent model mummy, as well as late medieval bones. In particular, the NMR-MOUSE was able to differentiate single layers of bandages versus underlying tissue on an isolated mummy hand, to measure across the fingernail into the tissue of an ancient mummified finger, and to discriminate different soft and hard tissue layers, both in dry and frozen mummified tissue and bone. It was found that the amplitude of the depth profiles varies across the skull in concordance with the bone density. Furthermore, deteriorated bone material from an ancient mummy and historic skeletons show lower bone density. These data give evidence that the density of dry bone can be assessed non-invasively with the NMR-MOUSE and such measurements have the potential to replace destructive measurements such as mercury intrusion porosimetry. However,

water containing frozen bone leads to higher signal amplitudes as observed in the laboratory and the historic Iceman mummy. Continuous monitoring of this signal in the Iceman may be another way of assessing its conservation state over time, as it is still debated whether or not Iceman is still decomposing [Mur03].

The NMR-MOUSE was successfully applied for the analysis of violins and bows to detect different types of wood used for the construction of violins and bows. The good spatial resolution provided by the NMR-MOUSE allows the detection of a thin varnish layer on top of the violin wood. The proton density obtained from the depth profiles allows a classification of the violins and bows as a function of the fabrication year, leading to a possible determination of a certain type of wood or of a fabrication year of a violin or bow just by detecting the proton densities with the NMR-MOUSE.

6 General Conclusions

Nuclear Magnetic Resonance was chosen as the main tool for investigating the different systems described, as it is unique in providing the information details about the morphology and molecular structures and conformations by which the fundamental properties of these biological and chemical systems can be understood. The main conclusions of this work summarize the results obtained as follows:

- Proton spin-diffusion experiments combined with ^{13}C CPMAS spectroscopy were successfully applied to characterize the changes that occur during the thermal denaturation of keratin fibers from wool and hair. A model describing both the effect of thermal denaturation and the effect of different chemical treatments on keratin fibers is presented.

- Proton NMR spectroscopy was used for studying the proton exchange in Sulfonated Polyether Ether Ketone proton exchange membranes revealing that the water exchange processes in hydrated SPEEK-silica membranes are more efficient when low concentrations of polyethoxysiloxane (PEOS) are used for the membrane preparation. Proton 1D exchange spectroscopy combined with transverse relaxation measurements offered good insight in the state of water in hydrated SPEEK/SiO$_2$ membranes revealing that concentrations of 5%-10% wt. PEOS could enhance the electrical conductivity of PEM.

- Hyperpolarized ^{129}Xe NMR spectroscopy was successfully applied for monitoring the free radical polymerization reactions of methyl methacrylate, methyl acrylate and the copolymerization of methyl methacrylate and methyl acrylate. The observation of Xe chemical shift and linewidths during the reactions reveal information about the polymer chain growths during the polymerizations.

- The successful application of the NMR-MOUSE to visualise the different anatomical layers with varying proton densities opens the possibility of its use in clinical studies such as osteoporosis for bone density measurements. The NMR-MOUSE was also successfully applied for the analysis of violins and bows and a classification of the violins and bows as a function of the fabrication year was achieved.

References

[Agu91]   A. Agur, *Grant's Atlas of Anatomy*, Williams and Wilkins, Baltimore, 1991.

[Alb94]   M. S. Albert, G. D. Cates, B. Driehuys, W. Happer, B. Saam, C. S. Springer, A. Wishnia, *Nature*, **370** (1994) 199-201.

[Alb95]   M. S. Albert, V. D. Schepkin, T. F. Budinger, *J. Comput. Assisted Tomogr.*, **19** (1995) 975.

[App98]   S. Appelt, A. Ben-Amar Baranga, C. J. Erickson, M. A. Romalis, A. R. Young, W. Happer, *Phys. Rev. A*, **58** (1998) 1412.

[App01]   S. Appelt, F. W. Häsing, S. Baer-Lang, N. J. Shah, B. Blümich, *Chem. Phys. Lett.*, **348** (2001) 263-269.

[App04]   S. Appelt, *From Photon Spin to Magnetic Resonance Imaging*, Habilitation, RWTH Aachen, 2004.

[Arr08]   B. T. Arriaza, V. G. Standen, V. Cassman, C. M. Santoro, Chinchorro Culture: Pioneers of the Coast of the Atacama Desert, in: H. Silverman, W. H. Isbell (eds), *Handbook of South American Archaeology*, Springer, New York, 2008, pp. 45-58.

[Ash00]   M. A. Ashby, *The Egyptian Book of the Dead*, Cruzian Mystic Books, 2000.

[Bai03]   A. D. Bain, *Prog. Nucl. Magn. Reson. Spec.*, **43** (2003) 103.

[Bai08]   M. Baias, D. E. Demco, I. Colicchio, B. Blümich, M. Möller, *Chem. Phys. Lett.*, **456** (2008) 227.

[Bai09]   M. Baias, D. E. Demco, C. Popescu, R. Fechete, C. Melian, B. Blümich, M. Möller, Thermal Denaturation of Hydrated Wool Keratin by ^{1}H Solid-State NMR, *J. Phys. Chem. B*, **113** (2009) 2184-2192.

[Bal94]   C. Baldock, S. W. Hughes, D. K. Whittaker, J. Taylor, R. Davis, A.J. Spencer, K. Tonge, A. Sofat, *J. Royal Soc. Med.*, **87** (1994) 806.

[Bea98]   D. Bear, T. E. Chupp, K. Cooper, S. DeDeo, M. Rosenberry, R. E. Stoner, R. L. Walsworth, *Phys. Rev. A*, **57** (1998) 5006.

[Bea00]   D. Bear, R. E. Stoner, R. L. Walsworth, V. A. Kostelecky, C. D. Lane, *Phys. Rev. Lett.*, **85** (2000) 5038.

[Bha83]   N. D. Bhaskar, W. Happer, M. Larsson, X. Zeng, *Phys. Rev. Lett.*, **50** (1983) 105.

[Bif96]   A. Bifone, Y. Q. Song, R. Seydoux, R. E. Taylor, B. M. Goodson, T. Pietrass, T. F. Budinger, G. Navon, A. Pines, *Proc. Nat. Acad. Sci. USA*, **93** (1996), 12932-6.

[Bir57]   M. S. C. Birbeck, E. H. Mercer, *J. Biophys. Biochem. Cytol.*, **3** (1957) 203.

[Blü00]   B. Blümich, *NMR Imaging of Materials*, Clarendon Press, Oxford, 2000.

[Blü03a]   B. Bümich, S. Anferova, S. Sharma, A.L. Segre, C. Federici, Degradation of historical paper: nondestructive analysis by the NMR-MOUSE, *J. Magn. Reson.*, **161** (2003) 204-209.

[Blü03b]   B. Blümich, S. Anferova, K. Kremer, S. Sharma, V. Herrmann, A. Segre, Unilateral NMR for quality control: the NMR-MOUSE, *Spectroscopy*, **18** (2003) 18–32.

[Blü05]   B. Blümich, *Essential NMR*, Springer, Berlin, 2005.

[Blü08]   B. Blümich, J. Perlo, F. Casanova, Mobile single-sided NMR, *Prog. Nucl. Magn. Res. Spect.*, **52** (2008) 197-269.

[Bou60]   M. A. Bouchiat, R. R. Carver, C. M. Varnum, *Phys. Rev. Lett.*, **5** (1960) 373.

[Bou69]   C. C. Bouchiat, M. A. Bouchiat, L. C. L. Pottier, *Phys. Rev.*, **181** (1969) 144.

[Bou72]   M. A. Bouchiat, J. Brossel, J. Pottier, *J. Chem. Phys.*, **56** (1972) 3703.

[Bre62]   R. G. Brewer, *J. Chem. Phys.*, **37** (1962) 2504.

[Bru98]   E. Brunner, R. Seydoux, M. Haake, A. Pines, J. A. Reimer, *J. Magn. Res.*, **130** (1998) 145.

[Buc56]   A. D. Buckingham, J. A. Pople, *Discuss. Faraday Soc.*, **22** (1956) 17.

[Bud03]   P. Budrugeac, L. Miu, V. Bocu, F.-J. Wortmann, C. Popescu, *J. Thermal Anal. Cal.*, **72** (2003) 1057.

[Bud04]   P. Budrugeac, L. Miu, V. Bocu, F.-J. Wortmann, C. Popescu, *J. Thermal Anal. Cal.*, **77** (2004) 975.

[Buda03a]   A. Buda, D. E. Demco, M. Bertmer, B. Blümich, V. M. Litvinov, J.-P. Penning, *J. Phys. Chem.* B, **107** (2003) 5357.

[Buda03b]   A. Buda, D. E. Demco, M. Bertmer, B. Blümich, B. Reining, H. Keul, H. Höcker, *Solid State Nucl. Magn. Reson.,* **24** (2003) 39.

[Buda04]   A. Buda, D. E. Demco, M. Bertmer, B. Blümich, V. M. Litvinov, J.-P. Penning, *Chem. Phys. Chem.*, **5** (2004) 876.

[But94]   R. Butscher, G. Wäckerle, M. Mehring, *J. Chem. Phys.*, **100** (1994) 6923.

[Cal91]   P. T. Callaghan, *Principles of Nuclear Magnetic Resonance Microscopy*, Calderon Press, Oxford, 1991.

[Car01]   L. Carrette, K. A. Friedrich, U. Stimming, *Fuel Cells*, **1** (2001) 5-39.

[Cav96]   J. Cavanagh, W. J. Fairbrother, A. G. Palmer, N. J. Skelton, *Protein NMR spectroscopy: Principles and Practice*, Academic Press, San Diego, 1996.

[Ces03]   F. Cesarani, M. C. Martina, A. Ferraris, R. Grilletto, R. Boano, E. F. Marochetti, A. M. Donadoni, G. Gandini, *Am. J. Roentgenol.*, **180** (2003) 597-606.

[Chi08]   G. Chiavari, S. Montalbani, V. Otero, *Rapid Communic. Mass. Spec.*, **22** (2008) 3711.

[Chm91]   B. F. Chmelka, D. Raftery, A. V. McCormick, L. C. de Menorval, R. D. Levine, A. Pines, *Phys. Rev. Lett.*, **66** (1991) 580-583.

[Cin68]   R. Cini, M. Torrini, *J. Chem. Phys.*, **49** (1968) 2826.

[Col06]   I. Colicchio, H. Keul, D. Sanders, U. Simon, T. E. Weirich, M. Möller, *Fuel Cells*, **6** (2006) 225.

[Col09]   I. Colicchio, D. E. Demco, M. Baias, H. Keul, M. Moeller, Influence of the silica content in SPEEK-silica membranes prepared from sol-gel process of polyethoxysiloxane: morphology and proton mobility, *J. Membrane Sci.*, (accepted).

[Cra75]   J. Crank, *The Mathematics of Diffusion*, Clarendon Press: Oxford, 1975.

[Dem95]   D. E. Demco, A. Johansson, J. Tegenfeldt, *Solid State Nucl. Magn. Reson.*, **4** (1995) 13.

[Deu98]   H. Deutz, F.-J. Wortmann, *J. Appl. Polym. Sci.*, **68** (1998) 1991.

[Due01]   M. J. Duer, *Solid-State NMR: Theory and Applications*, Blackwell Science Ltd.: Oxford, 2001.

[Due03]   M. J. Duer, N. McDougal, R. C. Murray, *Phys. Chem. Chem. Phys.*, **5** (2003) 2894.

[Eas61]   S. C. Easton, H. Wieruszowski, *The Era of Charlemagne: Frankish State and Society*, Robert E. Krieger Publishing, Huntington, New York, 1961.

[Ech08a]   J. P. Echard, B. Lavedrine, *J. Cult. Herit.*, **9** (2008) 420-429.

[Ech08b]   J. P. Echard, M. Cotte, E. Dooryhee, L. Bertrand, *Appl. Phys. A*, **9**2 (2008) 77-81.

[Edi96]   G. Eidmann, R. Savelsberg, P. Blümler, B. Blümich, The NMR MOUSE, a mobile universal surface explorer, *J. Magn. Reson.*, **A122** (1996) 104–109.

[Ein69]   Einhart, , Notker the Stammerer, *Two Lives of Charlemagne*, Penguin Books, London, 1969.

[Ern90]   R. R. Ernst, G. Bodenhausen, A. Wokaun, *Principles of Nuclear Magnetic Resonance in One and Two Dimensions*, Oxford Univ. Press: Oxford, 1990.

[Fau72]   R. O. Faulkner, *The Ancient Egyptian Book of the Dead*, University of Texas Press, Austin, 1972.

[Fau94] R. O. Faulkner, *The Egyptian Book of the Dead. The Book of Going Forth By Day*, Chronicle Books, 1994.

[Fer01] J. Ferguson, *The promise of portable MRI*, Eng. Sci., **2** (2001) 29-33.

[Feu02] M. Feughelman, *J. Appl. Polym. Sci.*, **83** (2002) 489.

[Fri07] C. Fritz, I. Cross, B. C. J. Moore, J. Woodhouse, *J. Acoustical Soc. Am.*, **122** (2007) 3640.

[Gae95] H. C. Gaede, Y.-Q. Song, R. E. Taylor, E. J. Munson, J. A. Reimer, A. Pines, *Appl. Magn. Res.*, **8** (1995) 373.

[Gla03] L. F. Gladden, *Magnetic resonance: ongoing and future role in chemical engineering research*, AIChE J., **49** (2003) 2-9.

[Gol66] M. Goldman, L. Shen, *Phys. Rev.*, **144** (1966) 321.

[Gos02] P. Gostner, E. E. Vigl, *J. Archaeol. Science*, **29** (2002) 323.

[Gow02] G. R. Goward, M. F. H. Schuster, D. Sebastiani, I. Schnell, H. W. Spiess, *J. Phys. Chem. B*, **106** (2002) 9322.

[Gro78] B. C. Grover, *Phys. Rev. Lett.*, **40** (1978) 391.

[Gut56] H. S. Gutowsky, C. H. Holm, *J. Chem. Phys.*, **25** (1956) 1228.

[Hak00] R. Haken, B. Blümich, Anisotropy in tendon investigated in vivo by a portable NMR scanner, the NMR-MOUSE, *J. Magn. Reson.*, **144** (2000) 195-199.

[Hal67] A. R. Haly, J. W. Snaith, *Text. Res. J.*, **37** (1967) 898.

[Han04] S. Han, H. Kühn, F. W. Häsing, K. Münnemann, B. Blümich, S. Appelt, *J. Magn. Reson.*, **167** (2004) 298-305.

[Hap72] W. Happer, *Rev. Mod. Phys.*, **44** (1972) 169.

[Hap84] W. Happer, E. Miron, S. Schaefer, D. Schreiber, W. A. Wijngaarden, X. Zeng, *Phys. Rev. A*, **29** (1984) 3092.

[Haw05] Z. Hawaas, Tutankhamun and thegolden age of the Pharaoahs, *National Geographic*, (2005) 263.

[Her65] R. Herman, *Phys. Rev.*, **137** (1965) 1062A.

[Hic04] M. A. Hickner, H. Ghassemi, Y. S. Kim, B. Einsla, J. E. McGrath, *Chem. Rev.*, **104** (2004) 4587.

[Hic05] M. A. Hickner, B. S. Pivovar, *Fuel Cells*, **5** (2005) 213.

[Hie84] P. C. Hiemenz, *Polymer Chemistry - The Basic Concepts*, Marcel Dekker, New York, 1984.

[Hof02a] H. Hoffman, W. E. Torres, R. D. Ernst, *Radiographics*, **22** (2002) 377-385.

[Hof02b]   H. Hoffman, P. A. Hudgins, *Am. J. Roentgenol.*, **178** (2002) 1367-1376.

[Hof03]   R. E. Hoffman, *J. Magn. Reson.*, **163** (2003) 325.

[Hut98]   C. M. Hutchins, *J. Audio Eng. Soc.*, **46** (1998) 751.

[Ist08]   D. Istrate, C. Popescu, M. Er Rafik, M. Möller, *Biopolymer*, 2008, submitted

[Ito82]   T. Ito, J. Frassaird, *J. Chem. Phys.*, **76** (1982) 5225.

[Jam70]   A. K. Jameson, C. J. Jameson, H. S. Gutowsky, *J. Chem. Phys.*, **53** (1970) 2310.

[Jam73]   C. J. Jameson, A. K. Jameson, S. M. Cohen, *J. Chem. Phys.*, **59** (1973) 4540.

[Jam92]   C. J. Jameson, A. C. de Dios, *J. Chem. Phys.*, **97** (1992) 417.

[Jam02]   C. J. Jameson, A. C. De Dios, *J. Chem. Phys.*, **116** (2002) 3805.

[Jan02]   R. J. Jansen, M. Poulus, W. Taconis, J. Stoker, *Comput. Med. Imag. Graph.*, **26** (2002) 211-216.

[Jän97]   H.-J. Jänsch, *Appl. Phys. A*, **65** (1997) 567.

[Jän98]   H.-J. Jänsch, T. Hof, U. Ruth, J. Schmidt, D. Stahl, D. Fick, *Chem. Phys. Lett.*, **296** (1998) 146.

[Jon85]   D. P. Jones, D. C. Leach, D. R. Moore, Mechanical properties of poly(ether-ether-ketone) for engineering applications, *Polymer*, **26** (1985) 1385.

[Kap80]   J. I. Kaplan, G. Fraenkel, *NMR of Chemically Exchanging Systems*, Academic Press, NewYork, 1980.

[Kas50]   A. Kastler, *J. Phys. Radium*, **11** (1950) 255.

[Ken91]   A. P. M. Kentgens, H. A. Van Boxtel, R.-J. Verweel, W. S. Veeman, *Macromolecules*, **24** (1991) 3712-3714.

[Kim03]   Y. S. Kim, L. Dong, M. A. Hickner, T. E. Glass, V. Webb, J. E. McGrath, *Macromolecules*, **36** (2003) 6281.

[Kle96]   R.L. Kleinberg, *Well logging*, D.M. Grant, R.K. Harris Eds., Encyclopedia of NMR, Wiley, New York, 1996.

[Kni88]   R. J. Knize, Z. Wu, W. Happer, *Advances in Atomic and Molecular Physics*, **24** (1988) 223.

[Kob98]   T. Kobayashi, M. Rikukawa, K. Sanui, N. Ogata, *Solid State Ionics*, **106** (1998)219-225.

[Kre01]   K. D. J. Kreuer, *Membr. Sci.*, **185** (2001) 29.

[Küh04]   H. Kühn, *NMR mit thermisch polarisiertem un hyperpolarisiertem Xe*, Dissertation ITMC, RWTH-Aachen (2004).

[Lap99]   M. Laporta, M. Pegoraro, L. Zanderighi, *Phys. Chem. Chem. Phys.*, **1** (1999) 4619.

[Ler05]   M. Leroy, J. Cao, *Biopolymer*, **77** (2005) 38.

[Lev01]   M. H. Levitt, *Spin Dynamics – Basics of Nuclear Magnetic Resonance*, John Wiley and Sons, Chichester, 2001.

[Li08]   J. Li, K. G. Wilmsmeyer, L. A. Madsen, *Macromolecules*, **41** (2008) 4555.

[Loc01]   E. Locci, Y. Dehouck, M. Casu, G. Saba, A. Lai, M. Luhmer, J. Reisse, K. Bertik, *J. Magn. Reson.*, **150** (2001) 167-4.

[Lon93]   H. W. Long, H. C. Gaede, J. Shore, L. Reven, C. R. Bowers, J. Kritzenberger, T. Pietrass, A. Pines, *J. Am. Chem. Soc.*, **115** (1993) 8491.

[Mac88]   J. W. Mack, D. A. Torchia, P. M. Steinert, *Biochemistry*, **27** (1988) 5418.

[Mag89]   D. Magid, B. M. Bryan, R. A. Drebin, D. Ney, E. K. Fishman, *Clin. Imag.*, **13** (1989) 239-240.

[Mai03]   R. W. Mair, R. Wang, M. S. Rosen, D. Candela, D. G. Cory, R. L. Walsworth, *Magn. Reson. Imag.*, **21** (2003) 287.

[Mar80]   M. L. Martin, G. L. Martin, J.-J. Delpuech, *Practical NMR spectroscopy*, Heyden, London, 1980.

[Mar88]   M. Marx, D. H. D'Auria, *Am. J. Roentgenol.*, **150** (1988) 147-149.

[Mat98]   G. A. Matzkanin, *A review of non-destructive characterization of composites using NMR*, P. Höller, V. Hauck, C. O. Ruud, R. E. Green Eds., Nondestructive Characterization of Materials, Springer, Berlin, 1998.

[May97]   B. X. Mayer, C. Reiter, T. L. Bereuter, *J. Chromatogr. B*, **692** (1997) 1-6.

[McC58]   H. M. McConnell, *J. Chem. Phys.*, **28** (1958) 430.

[Mil99]   C. Miles, M. Ghelashvili, *Biophysical Journal*, **76** (1999) 3243.

[Mou00]   I. L. Moudrakovski, S. Lang, C. I. Ratcliffe, S. Benoit, G. Santyr, J. A. Ripmeester, *J. Magn. Reson.*, **144** (2000) 372.

[Mou04]   I. L. Moudrakovski, L. Q. Wang, T. Baumann, J. H. Satcher, G. H. Exarhos, C. I. Ratcliffe, J. A. Ripmeester, *J. Am. Chem. Soc.*, **126** (2004) 5052.

[Mur03]   W. A. Murphy, D. zur Nedden, P. Gostner, R. Knapp, W. Recheis, H. Seidler, *Radiology*, **226** (2003) 614-629.

[Nat05]   A. Nather, *Bone Grafts and Bone Substitutes*, World Scientific Publishing Co Pte Ltd, 2005.

[Nav96]   G. Navon, Y.-Q. Song, T. Rõõm, S. Appelt, R. E. Taylor, A. Pines, *Science*, **271** (1996) 1848.

[Nis98]   N. Nishikawa, Y. Tanizawa, S. Tanaka, Y. Horiguchi, T. Asakura, *Polymer,* **39** (1998) 3835.

[Nis99]   N. Nishikawa, Y. Horiguchi, T. Asakura, I. Ando, *Polymer,* **40** (1999) 2139.

[Nos03]   A. Nossov, E. Haddad, F. Guenneau, A. Gedeon, *Phys. Chem. Chem. Phys.*, **5** (2003) 4473.

[Pad03]   S. J. Paddison, *Annu. Rev. Mater. Res.*, **33** (2003) 289.

[Par85]   D. A. P. Parry, R. D. B. Fraser, *Int. J. Biol. Macromol.,* **7** (1985) 203.

[Par05]   D. A. Parry, *Adv. Protein Chem.,* **70** (2005) 113.

[Ped03]   H.T. Pedersen, S. Ablett, D.R. Martin, M.J.D. Mallett, S.B. Engelsen, Application of the NMR-MOUSE to food emulsions, *J. Magn. Reson.*, **165** (2003) 49-58.

[Per95]   J. W. Perich, R. B. Johns, A. R. Thompson, *Aust. J. Chem.,* **48** (1995) 1925.

[Per05]   J. Perlo, F. Casanova, B. Blümich, Profiles with microscopic resolution by single-sided NMR, *J. Magn. Reson.*, **176** (2005) 64-70.

[Per06]   J.-C. Perrin, S. Lyonnard, A. Guillermo, P. Levitz, *J. Phys. Chem.*, **110** (2006) 5439.

[Pie98]   T. Pietrass, R. Seydoux, A. Pines, *J. Magn. Res.*, **133** (1998) 299.

[Pop07]   C. Popescu, H. Hoecker, *Chem. Soc. Rev.*, **36** (2007) 1282.

[Pop08]   C. Popescu, P. Budrugeac, F.-J. Wortmann, L. Miu, D. E. Demco, M. Baias, *Polym. Degrad. Stab*., **93** (2008) 976.

[Pow59]   J. G. Powles, *The atomic nucleus as a magnetic top*, New Sci., **5** (1959) 26.

[Pow97]   B. C. Powles, G. E. Rogers, *In Formation and Structure of Human Hair*, P. Jolles, H. Zahn, H. Höcker, Eds., Birkhäuser Verlag: Basel, Switzerland, 1997, pp 59-167.

[Pra01]   P.J. Prado, NMR hand-held moisture sensor, *Magn. Reson. Imag.*, **19** (2001) 505-508.

[Raf91]   D. Raftery, H. Long, T. Meersmann, P. J. Grandinetti, L. Reven, A. Pines, *Phys. Rev. Lett.*, **66** (1991) 584.

[Raf94]   D. Raftery, B. F. Chmalka, Xe NMR spectroscopy, *NMR – Basic Principles and Progress*, **30** (1994) 111.

[Raf04]   M. Er Rafic, J. Doucet, F. Briki, *Biophys. J.,* **86** (2004) 3893.

[Rat98]   C. I. Ratcliffe, Xenon NMR, *Ann. Rep. NMR. Spec.*, **36** (1998) 123.

[Rei00]   D. Reichert, G. Hempel, Z. Luz, P. Tekely, H. Schneider, *J. Magn. Reson.*, **146** (2000) 311.

[Rol97]   F. Rollo, S. Luciani, M. Ubaldi, *Human Evolution*, **12** (1997) 197.

[Ros01]   M. A. Rosenberry, T. E. Chupp, *Phys. Rev. Lett.*, **86** (2001) 22.

[Rub00a]   S. M. Rubin, M. M. Spence, B. M. Goodson, D. E. Wemmer, A. Pines, *Proc. Nat. Acad. Sci. USA*, **97** (2000) 9472-5.

[Rub00b]   S. M. Rubin, M. M. Spence, I. E. Dimitrov, E. J. Ruiz, A. Pines, D. E. Wemmer, *J. Am. Chem. Soc.*, **123** (2000) 8616-7.

[Rus30]   C. E. Russell, *Charlemagne: First of the Moderns*, The Riverside Press, Boston, 1930.

[Rüh04]   F. J. Rühli, R. K. Chhem, T. Böni, *Can. Assoc. Radiol. J.*, **55** (2004) 218.

[Rüh06]   F. J. Rühli, E. Egarter-Vigl, P. Gostner, *Am. J. Phys. Anthropol.*, **42** (2006) 156.

[Rüh07]   F. Rühli, T. Böni, J. Perlo, F. Casanova, M. Baias, E. Egarter, B. Blümich, Non-invasive spatial tissue discrimination in ancient mummies and bones in situ by portable nuclear magnetic resonance, *J. Cult. Herit.*, **8** (2007) 257.

[San82]   J. Sandstrom, *Dynamic NMR Spectroscopy*, Academic Press, London, 1982

[Sea03]   D. N. Sears, C. J. Jameson, *J. Chem. Phys.*, **119** (2003) 12231.

[Sch93]   K. Schmidt-Rohr, H. W. Spiess, *Acta Polymer,* **44** (1993) 1.

[Sch94]   K. Schmidt-Rohr, H. W. Spiess, *Multidimensional Solid-State NMR and Polymers*, Academic Press: London, 1994.

[Sch08]   E. Schoonderwaldt, K. Guettler, A. Askenfelt, *Acta Acustica united with Acustica*, **94** (2008) 604.

[Sha70]   H. Shanan-Atidi, K. H. Bar-Eli, *J. Phys. Chem.*, **74** (1970) 961.

[Sir97]   S. A. Sirr, J. R. Waddle, *Radiology*, **203** (1997) 801.

[Son97]   Y. Q. Song, B. M. Goodson, R. E. Taylor, D. D. Laws, G. Navon, A. Pines, *Angew. Chem.*, Intl. ed. Engl., **36** (1997) 2368.

[Son00]   Y. Q. Song, *Concepts Magn. Reson.*, **12** (2000) 6-20.

[Sta02]   D. Stahl, W. Mannstadt, P. Gerhard, M. Koch, H. Jänsch, *J. Magn. Reson.*, **159** (2002) 1.

[Ste87]   T. R. Stengle, K. L. Williamson, *Macromolecules*, **20** (1987) 1428-1430.

[Ste89]   P. M. Steinert, D. R. Torkia, J. W. Mack, *In Formation and Structure of Human Hair*, G. E. Roger, P. J. Reis, K. A. Ward, Eds., Chapman & Hall: London, 1989, pp 157-167.

[Sto96]   R. E. Stoner, M. A. Rosenberry, J. T. Wright, T. E. Chupp, E. R. Oteiza, R. L. Walsworth, *Phys. Rev. Lett.*, **77** (1996) 3971.

[Str61]   R. L. Streever, H. Y. Carr, *Phys. Rev.*, **121** (1961) 20.

[Stu04]   D. Stueber, C. J. Jameson, The chemical shifts of Xe in the cages of clathrate hydrate structures I and II, *J. Chem. Phys.*, **120** (2004) 1560.

[Tay01]   J. H. Taylor, *Death and the Afterlife in Ancient Egypt*, University of Chicago Press, 2001.

[Tek00]   P. Tekely, D. Reichert, H. Zimmermann, Z. Luz, *J. Magn. Reson.*, **145** (2000) 173.

[Ter02]   V. V. Terskikh, I. L. Moudrakovski, S. R. Breeze, S. Lang, C. I. Ratcliffe, J. A. Ripmeester, A. Sayari, *Langmuir*, **18** (2002) 5653.

[Til82]   R. F. Tilton, I. D. Kuntz, *Biochemistry*, **21** (1982) 6850-7.

[Tse99]   C. H. Tseng, R. W. Mair, G. P. Wong, D. Williamson, D. G. Cory, R. L. Walsworth, *Phys. Rev. E*, **59** (1999) 1785.

[Tyc94]   R. Tycko (Ed.), *Nuclear Magnetic Resonance Probes of Molecular Dynamics*, Kluwer Academic Publishers, Boston, 1994.

[Val97]   R. Valiullin, R. Kimmich, N. Fatkulin, *Phys. Rev. E*, **56** (1997) 4371.

[Van96]   D. L. VanderHart, G. B. McFadden, *Solid State Nucl. Magn. Reson.*, **7** (1996) 45.

[Vol80]   C. H. Volk, T. M. Kwon, J. G. Mark, *Phys. Rev. A*, **21** (1980) 1549.

[Wal97]   T. G. Walker, W. Happer, *Rev. Mod. Phys.*, **69** (1997) 629.

[Wan04]   R. Wang, R. W. Mair, M. S. Rosen, D. G. Cory, R. L. Walsworth, *Phys. Rev. E*, **70** (2004) 026312.

[Wan96]   J. Wang, *J. Chem. Phys.,* **104** (1996) 4850.

[Wil06]   D. A. Wilson, *Charlemagne: the great adventure*, Doubleday, New York, 2006.

[Wol00a]   J. Wolber, A. Cherubini, M. O. Leach, A. Bifone, *Magn. Res. Med.*, **43** (2000) 491.

[Wol00b]   J. Wolber, A. Cherubini, M. O. Leach, A. Bifone, *NMR Biomed.*, **13** (2000) 234

[Wor07]   F.-J. Wortmann, C. Popescu, G. Sendelbach, *Biopolymers*, **83** (2007) 630.

[Wor08]   F.-J. Wortmann, C. Popescu, G. Sendelbach, *Biopolymers*, **89** (2008) 600.

[Wüt86]   K. Wüthrich, *NMR of Proteins and Nucleic Acids*, John Wiley & Sons, Inc., 1986.

[Ye06]   G. Ye, N. Janzen, G. R. Goward, *Macromolecules*, **39** (2006) 3283.

[Ye07]   G. Ye, C. A. Hayden, G. R. Goward, *Macromolecules*, **40** (2007) 1529.

[Yos90]   H. Yoshimizu, I. Ando, *Macromolecules*, **23** (1990) 2908.

[Yua07]   H. Yuan, S. Murad, C. J. Jameson, J. D. Olson, *J. Phys. Chem. C*, **111** (2007) 15771-15783.

[Yue07]   X. Yue, H. Zhang, W. Chen, Y. Wang, S. Zhang, G. Wang, Z. Jiang, Crosslinkable fully aromatic poly(aryl ether ketone)s bearing macrocycle of aryl ether ketone, *Polymer*, **48** (2007) 4715.

[Zai00]   S. M. J. Zaidi, S. D. Mikhailenko, G. P. Robertson, M. D. Guiver, S. Kaliaguine, *J. Membr. Sci.*, **173** (2000) 17-34.

[Zaw91]   T. A. Zawodzinski Jr, M. Neeman, L. O. Sillerud, S. Gottesfeld, *J. Phys. Chem.*, **95** (1991) 6040.

[Zhu06]   X. Zhu, M. Jaumann, K. Peter, M. Möller, C. Melian, A. Adams-Buda, D. E. Demco, B. Blümich, *Macromolecules*, **39** (2006) 1701.

Acknowledgments

- First of all I'd like to thank Professor Blümich for accepting me in his group, for his guidance and advices, and especially for giving me the freedom on working on many interesting projects.

- My deepest gratitude goes to Professor Dan Demco, for the many useful discussions, for helping me understand the basic physics of the NMR, and mostly for working with someone as stubborn as me.

- Many thanks to Professor Stephan Appelt for all his help with the Xe experiments, and especially for the many long discussions that provided me a deeper understanding not only of NMR but all the other physical phenomena that helps us better understand the Universe.

- I would also like to acknowledge Prof. Siegfried Stapf, Prof. Jeff Reimer, Prof. Crisan Popescu, and Federico Casanova for their nice and interesting lectures.

- Special thanks go to my best friend Isa, who always supported and encouraged me, every time I had a presentation or a talk, always finding the right words to say, and always listening whenever I needed to complain about something. Gs (&lQ)...

- Many thanks go to my other best friends Adi, Cristi, and Elena for all their support and for showing me that sometimes life is not all about sitting in a lab, and thank you very much for all your encouragements from the night before my PhD exam.

- I would also like to thank all my other friends and colleagues, Alexandra, Andrea, Lichi, Juan, Ernesto, Qingxia, João, Jörg, Jürgen, Nadia, Eva, Santosh, Rudra, Gabi, Dragos, Gighi, Irene, Dan, Agi, Lavinia, Eva, both for our work collaborations and for all the great time we had together in Aachen and all the other places where we were together in conferences.

- By far the greatest acknowledgments go to my family, my parents, and my grandma, who were always there for me no matter what, for their unlimited faith in me, for all their advice, for believing in me at all times, for trusting me to make the right decisions in life and supporting them. I could write a whole book just thanking them, and it will still not be enough to express my deepest gratitude and love for them. Va multumesc din tot sufletul pentru tot ce ati facut pentru mine, pentru ca ati crezut in mine, ca ati crezut ca voi reusi chiar si cand eu eram convinsa ca nu va fi asa.

- I'm sure I left out some people (accidentally, of course), so whoever you are, I'm sorry, and... thank you, too.

Curriculum Vitae

Maria Antoaneta Baias

Birth date and place: 3rd of July 1982, Dej, Romania

Education:

April 2009:	Defence for the Doctoral Degree in Natural Science
2006-2009:	Ph.D. student, RWTH Aachen, Germany.
	Dissertation: Science and history explored by nuclear magnetic resonance.
2005-2007:	Master degree in Biophysics and Medical Physics, Faculty of Physics, "Babes-Bolyai" University, Cluj-Napoca, Romania.
2001-2005:	University degree in Medical Physics, Faculty of Physics, "Babes-Bolyai" University, Cluj-Napoca, Romania.
1993-2001:	Secondary School, Dej, Romania
1989-1993:	Primary School, Dej, Romania.

Publications:

- M. Baias, D. E. Demco, D. Istrate, C. Popescu, B. Blümich, M. Möller, *Morphology and molecular mobility of fibrous hard α-keratins by ^{1}H, ^{13}C, and ^{129}Xe NMR*, J. Phys. Chem. B 113 (2009) 12136-12147.

- M. Baias, D. E. Demco, B. Blümich, M. Möller, *State of water in hybrid sulfonated poly(ether ether ketone) – silica membranes by ^{1}H solid-state NMR*, Chem. Phys. Lett. 473 (2009) 142-145.

- I. Colicchio, D. E. Demco, M. Baias, H. Keul, M. Möller, *Influence of the silica content in SPEEK-silica membranes prepared from the sol-gel process of polyethoxysiloxane: morphology and proton mobility*, J. Membr. Science 337 (2009) 125-135.

- M. Baias, D. E. Demco, I. Colicchio, B. Blümich, M. Möller, *Proton exchange in hybrid sulfonated poly(ether ether ketone)-silica membranes by ^{1}H solid-state NMR*, Chem. Phys. Lett. 456 (2008) 227-230.

- M. Baias, D. E. Demco, C. Popescu, Radu Fechete, Claudiu Melian, Bernhard Blümich, Martin Möller, *Thermal denaturation of hydrated wool keratin by ^1H solid-state NMR*, J. Phys. Chem. B 113 (2008) 2184-2192.

- Adrian Pirnau, Vasile Chis, Ovidiu Oniga, Nicolae Leopold, Laszlo Szabo, Maria Baias, Onuc Cozar, *Vibrational and DFT study of 5-3-pyridyl-methylidene-thiazolidine-2-thione-4-one*, Vibrational Spectroscopy 48 (2008) 289-296.

- Crisan Popescu, Petre Budrugeac, Franz-Josef Wortmann, Lucretia Miu, Dan E. Demco, Maria Baias, *Assessment of collagen-based materials that are supports of cultural and historical objects*, Polymer Degradation and Stability 93 (2008) 976-982.

- F. Rühli, T. Böni, J. Perlo, F. Casanova, M. Baias, E. Egarter, B. Blümich, *Noninvasive spatial tissue discrimination in ancient mummies and bones by in situ portable nuclear magnetic resonance*, Journal of Cultural Heritage 8 (2007) 257-263.

- Pirnau, V. Chis, M. Baias, O. Cozar, M. Vasilescu, O. Oniga, S. Simon, *Experimental and DFT Investigation Of 5-Para-Nitro-Benziliden-Tiazolidin-2-Tion-4-ona*, J. Optoelectron. Adv. M. 9 (2007) 547-550.

- M. Baias, A. Pirnau, V. Chis, O. Cozar, M. Vasilescu, *Experimental and Theoretical Investigation of 5-Para-Fluoro-Benziliden-Tiazolidin-2Tion-4-Ona*, J. Optoelectron. Adv. M. 8 (2006) 205-207.

- Mihai A. Voda, Dan E. Demco, Alexandra Voda, Thomas Schauber, Matthias Adler, Thomas Dabisch, Alina Adams, Maria Baias, Bernhard Blümich, *Morphology of thermoplastic polyurethanes by ^1H spin-diffusion NMR. Correlation with thermodynamic and mechanical properties,* Macromolecules 39 (2006) 4802-4810.

- Marko Bertmer, Dan E. Demco, Mingfei Wang, Claudiu Melian, Ramona I. Marcean-Chelcea, Radu Fechete, Maria Baias, Bernhard Blümich, *Segmental dynamic heterogeneity of short-chain grafted-poly(dimethylsiloxane) by ^1H spin-diffusion NMR*, Chem. Phys. Lett 431 (2006) 404-409.

- O. Cozar, V. Chis, L. David, M. Baias, *Experimental and density functional theory investigation on some biomedical compounds*, J. Optoelectron. Adv. M. 8 (2006) 164-171.